Water Transport in Fuel Cell Membranes Measured by Laser Interferometry

by

Jungik Kim

M.S. Mechanical Engineering
Seoul National University, Seoul, Korea, 2001

Submitted to the Department of Mechanical Engineering
in partial fulfillment of the requirements for the degree of

Doctor of Philosophy in Mechanical Engineering

at the

MASSACHUSETTS INSTITUTE OF TECHNOLOGY

June 2009

Author _____

Department of Mechanical Engineering
February 25, 2009

Certified by _____

Yang Shao-Horn
Associate Professor of Mechanical Engineering
Thesis Supervisor

Accepted by _____

David E. Hardt
Chairman, Committee on Graduate Students

Water Transport in Fuel Cell Membranes Measured by Laser Interferometry

by

Jungik Kim

Submitted to the Department of Mechanical Engineering on February 25, 2009
in partial fulfillment of the requirements for the degree of
Doctor of Philosophy in Mechanical Engineering

ABSTRACT

Proton exchange membrane (PEM) fuel cells are considered as one of the most promising clean energy conversion devices. The strong dependency of the proton conductivity of Nafion® membranes, which are the most widely used PEM, on the water content and the large amount of swelling due to water uptake makes the understanding of the water transport mechanism in these membranes crucial for estimating the performance and the durability of the fuel cells and developing a better system. In this regard, a laser interferometry technique to visualize the water content of Nafion® membranes with temporal and spatial resolutions has been developed on the basis of the linear relationship between the optical path length and the water content. The technique was applied 1) to evaluate the fundamental properties of the water transport, the coefficients of diffusion and electro-osmotic drag, and 2) to monitor a Nafion® membrane assembled in a fuel cell. The procedures for evaluating the transport properties rely on the temporal and spatial derivatives of the water content obtained from the laser interferometry and the use of the governing equations for the transport phenomena, which allow the calculation of the coefficients of diffusion or electro-osmotic drag as a function of the water content from a single experiment. The measured chemical diffusion coefficients showed a strong dependency on the compressive stress applied on the membrane, suggesting that a spatially non-uniform distribution of the diffusion process or the water content can develop during the fuel cell operation. The coefficients of electro-osmotic drag were found to increase with the increasing water content, which indicates that the Grotthuss mechanism of proton transfer is not active in the membranes with low water content. The successful evaluation of these coefficients has not only showed the validity of this new technique, which is confirmed by the agreement between the measured coefficients and the models proposed to explain the transport of water within Nafion® membranes, but also provided useful information to describe and understand the water transport mechanism in Nafion® membranes. Finally, the application of the laser interferometry to the membranes within a fuel cell has demonstrated the feasibility of the technique as an in-situ tool for monitoring the water content, which can be used for optimizing the designs of fuel cell components.

Thesis Supervisor: Yang Shao-Horn
Title: Associate Professor of Mechanical Engineering

ACKNOWLEDGEMENTS

First of all, I would like to thank Professor Yang Shao-Horn for her endless and patient supports for the past five years. Without her continuous guidance and trust in me, it would not have been possible for me to have what I am and what I have achieved today. She has been a mentor to me not only for the research, but also for my life at MIT.

Professor George Barbastathis, Professor Paula Hammond, and Professor Mary Boyce kept me on the right track with valuable discussions and suggestions. Their insightful questions and constructive advices from their expertise have been very helpful for me to strengthen my research where optics, polymer, and mechanics converge together.

I am grateful to Laura Waller who shared her experience on optical measurements. Also, Nathan Ashcraft, Seung Woo Lee, and Dr. Avni Argun helped me a lot with the sample preparations and the measurements on thin films of polymer.

Much of my thanks must go to the members of EEL who helped me in many ways as collaborators and friends, and made my life at MIT much more enjoyable than without them. Ethan Crumlin kindly made me the experimental devices without which many parts of my experiments would not have been possible. Dr. Shuo Chen introduced SEM to me. Dr. Gerardo Jose Lao never hesitated to give his hands whenever I needed. It would be impossible to enumerate the invaluable moments of discussions and conversations I had with the people of EEL.

Also, many thanks to my friends who shared bad times and good times with me, especially Yeunwoo Cho, Hohyun Lee, Minseung Ahn, Heejin Lee, Sunho Park, Yongtae Kim, Kihyoung Cho, and many others.

I would like to thank my family who supported me with their unconditional love and care: my mother Hyunsook Han, my late father Doyoung Kim, my sister Jiyoung, and my parents-in-law, Sookjong Lee and Yongsoon Shin. Finally, I should share whatever I have achieved at MIT with my wife, Jeungyon Lee who always believes in her humble husband and my daughter, Yejoon Kim who has been a source of my delight since her birth throughout the tough periods.

TABLE OF CONTENTS

LIST OF FIGURES

LIST OF TABLES

Chapter 1. Introduction

1.1 Basics of Proton Exchange Membrane (PEM) Fuel Cells

The problems of global warming and environmental pollution have been urging the development of clean energy conversion systems that emit less CO_2 and particulate matters. Hydrogen is a promising fuel for these systems because its byproduct is only water provided that hydrogen is produced from renewable energy sources. One of the problems of hydrogen as a fuel is its relatively low volumetric energy density as shown in Figure 1.

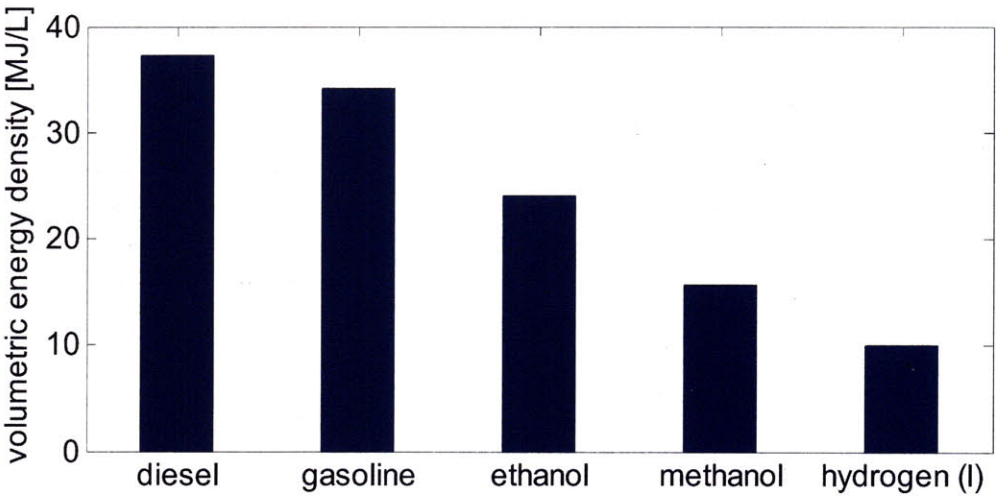

Figure 1. Comparison of the volumetric energy densities of common fuels in liquid form.

To solve the problem of low volumetric energy density requires the efficiency of energy conversion devices using hydrogen fuel to be high enough to have a decent operating duration for stationary applications or a reasonable driving range for automotive applications. High efficiency is important also in terms of the cost as well because hydrogen is not obtained for free and the production of hydrogen generates pollutants.

In this respect, fuel cells are considered as one of the most promising energy conversion devices because they can directly convert the chemical energy of hydrogen to electrical energy. The efficiency of this electrochemical process does not depend on the difference of temperature and is not limited by the Carnot efficiency that defines the

maximum efficiency of conventional heat engines. In addition, since there are no moving parts in fuel cells, the operation does not involve additional efficiency loss due to friction.

There are several types of fuel cells classified by the type of electrolyte used in the cells, as listed in Table 1.

Table 1. Comparison of fuel cell technologies. Adapted from the Reference.[1]

Fuel cell type	Common electrolyte	Operating temperature	System output	Electrical efficiency	Applications	Advantages
Polymer Electrolyte Membrane (PEM)*	solid organic polymer poly-perfluorosulfonic acid	50~ 100 °C	<1kW~ 250kW	53~ 58 %	-backup power -portable power -small distributed generation -transportation -specialty vehicles	-solid electrolyte reduces corrosion & electrolyte management problems -low temperature -quick start-up
Alkaline (AFC)	aqueous solution of potassium hydroxide soaked in a matrix	90~ 100 °C	10 kW~ 100 kW	60 %	-military -space	-cathode reaction faster in alkaline electrolyte, leads to higher performance -can use a variety of catalysts
Phosphoric Acid (PAFC)	liquid phosphoric acid soaked in a matrix	150~ 200 °C	50 kW~ 1 MW	> 40 %	-distributed generation	-higher overall efficiency with CHP** -increased tolerance to impurities in hydrogen
Molten Carbonate (MCFC)	liquid solution of lithium, sodium, and/or potassium carbonates, soaked in a matrix	600~ 700 °C	<1kW~ 1MW	45~47 %	-electric utility -large distributed generation	-high efficiency -fuel flexibility -can use a variety of catalysts -suitable for CHP
Solid Oxide (SOFC)	yttria stabilized zirconia	600~ 1000 °C	<1kW~ 3MW	35~43 %	-auxiliary power -electric utility -large distributed generation	-high efficiency -fuel flexibility -can use a variety of catalysts -solid electrolyte reduces electrolyte management problem -suitable for CHP -hybrid/GT cycle

*Direct Methanol Fuel Cell (DMFC) are a subset of PEM typically used for small portable power applications with a size range of about a sub-watt to 100 W and operating temperature at 60 ~ 90 °C

** Combined Heat and Power

Although each type of fuel cell has its own advantages, PEM (Polymer Electrolyte Membrane or Proton Exchange Membrane) fuel cells are considered to be a suitable alternative to the conventional gasoline engines for automotive applications because of the relatively higher efficiency than those of other types of fuel cells and the capability of

low temperature operation allowing quick start-up.[2,3]

A PEM fuel cell typically has three key components for the desired electrochemical reaction, which are current collector, gas diffusion electrode, and proton exchange membrane, as illustrated in Figure 2

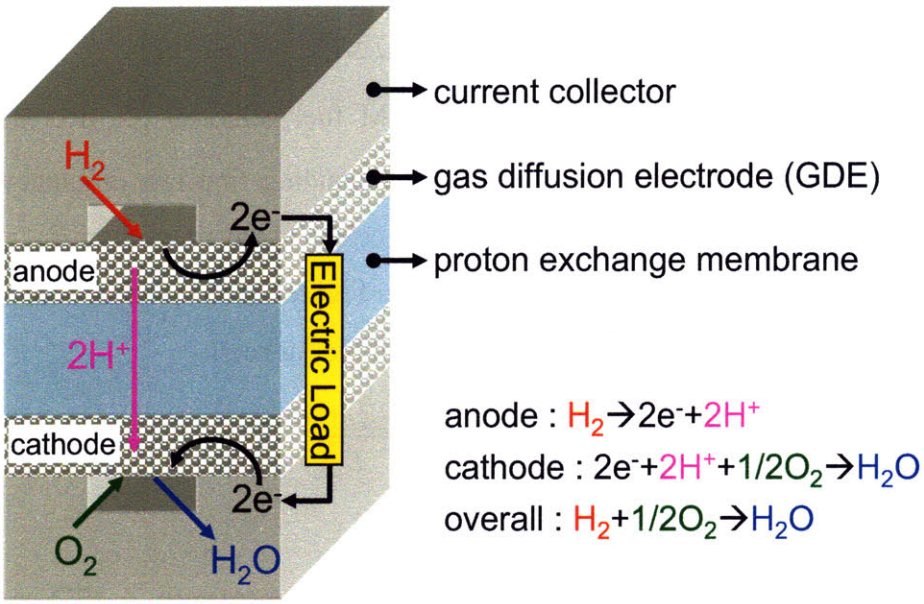

Figure 2. Schematic of a PEM fuel cell composed of current collectors/gas flow channels, gas diffusion electrodes (GDE), and a proton exchange membrane. Hydrogen is oxidized at the anode (top GDE) and oxygen is reduced at the cathode (bottom GDE) to get electricity.

The ideal output voltage of this system without any current (Open Circuit Voltage, OCV) can be estimated by the Nernst equation:

$$E_{ideal} = \frac{-\Delta G_r^0}{2F} + \frac{RT}{2F} \ln\left(\frac{P_{H_2} P_{O_2}^{1/2}}{P_{H_2O}}\right), \qquad \text{Eq. 1}$$

where F, R, and T are Faraday's constant (96485 C/mol), the universal gas constant (8.31 J/mol·K) and the operating temperature in Kelvin, respectively. P_i's are the partial pressure of the reactants and the products. ΔG_r^0, the difference in the Gibbs free energy between the products and the reactants at standard pressure (1 atm), is known to be -237 kJ/mol at 298K. Therefore, if a PEM fuel is operated at 25°C with pure reactants of H_2 and O_2 at 1atm being converted to liquid water, then the ideal OCV of 1.23 V can be

obtained. The comparison of this voltage to 1.48 V calculated based on the enthalpy change, ΔH_r^0, gives the theoretical maximum efficiency (83 %) of PEM fuel cells in terms of the first law of the thermodynamics. The first law efficiency tends to decrease with increasing temperature due to the increased effect of the entropy change (ΔS_r^0) at elevated temperatures on the Gibbs free energy of the reaction:

$$\Delta G_r^0 = \Delta H_r^0 - T\Delta S_r^0 \qquad \text{Eq. 2}$$

ΔG_r^0 at a typical operating temperature of PEM fuel cells, 80 °C, decreases to 228 kJ/mol resulting in E_{ideal} = 1.18 V and the corresponding first law efficiency of 80 %. However, the measured output voltage of a fuel cell is always less than E_{ideal} especially when current is drawn from the cell as depicted in Figure 3 and the ratio between the two voltages defines the second law efficiency (η_{2nd}) of the fuel cell:

$$\eta_{2nd} = \frac{E_{measured}}{E_{ideal}} = \frac{E_{ideal} - E_{loss}}{E_{ideal}} \qquad \text{Eq. 3}$$

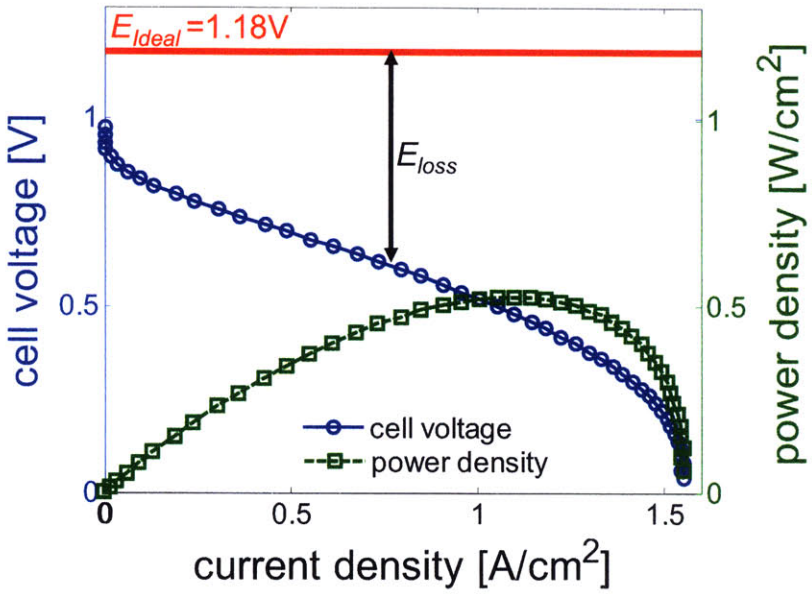

Figure 3. Typical cell voltage and power density as a function of the current density from a PEM fuel cell. The testing conditions are: cell temperature = 70 °C, pressure = 1 atm, no external humidification, H_2 flow rate = 100 cc/min, O_2 flow rate = 150 cc/min, 5 cm^2 active area membrane electrode assembly composed of Nafion® 112 membrane coated with 0.5 mg-Pt/cm^2 catalyst layer and gas diffusion layer (E-tek, LT 1400-W).

There are several factors making the measured voltage deviate from the ideal one, which can be categorized into activation loss (ΔE_{act}), ohmic loss (ΔE_{ohm}), and mass transport loss (ΔE_{mass}). Activation loss is the result of the sluggishness of the electrochemical reactions at the electrodes and can be related to the current density, i, by Butler-Volmer equation:

$$i = i_0 \left\{ \exp\left[\frac{2\alpha F}{RT} \Delta E_{act} \right] - \exp\left[-\frac{2(1-\alpha)F}{RT} \Delta E_{act} \right] \right\}, \qquad \text{Eq. 4}$$

where i_0 is the exchange current density and α is the transfer coefficient. When ΔE_{act} is very small, Eq. 4 can be simplified by using the approximation of $\exp(x) \approx x + 1$:

$$i = i_0 \left\{ \left[\frac{2\alpha F}{RT} \Delta E_{act} \right] + 1 - \left[-\frac{2(1-\alpha)F}{RT} \Delta E_{act} \right] - 1 \right\} = i_0 \frac{2F}{RT} \Delta E_{act} \qquad \text{Eq. 5}$$

From Eq. 5, it is clear that the slope of the voltage loss in the low current density region is inversely proportional to i_0, which represents the catalytic activity of the fuel cell electrodes.

Ohmic loss is associated with the ohmic resistance of the fuel cell components, such as the electrical resistance of the GDE's and current collectors and, more importantly, ionic resistance of the proton exchange membrane. By neglecting the effect of electrical resistance and using Ohm's law, the following relation is obtained:

$$\Delta E_{ohm} = iRA = i \left(\frac{1}{\sigma_{proton}} \right) d, \qquad \text{Eq. 6}$$

where σ_{proton}, A, and d are the proton conductivity, area, and thickness of the proton exchange membrane, respectively.

Mass transport loss is associated with insufficient supply of reactant gases to the reaction sites, which has more impact on the performance of fuel cells operating at high current density. These voltage losses from different sources are added up to get the total loss and Eq. 3 can be rewritten as:

$$\eta_{2nd} = \frac{E_{measured}}{E_{ideal}} = \frac{E_{ideal} - (\Delta E_{act} + \Delta E_{ohm} + \Delta E_{mass})}{E_{ideal}} \qquad \text{Eq. 7}$$

Since ohmic loss is proportional to current density, its effect is minimal at low current density where also the mass transport loss is not yet involved. Therefore, the profile of

the cell voltage in the low current density region is mostly attributed to the activation loss. In the middle range of the current density, the activation loss gets less sensitive to the current density and the slope of the linear portion of the profile represents the ohmic loss. Finally the deviation from the linear slope in the high current density region results from mass transport loss.

Different strategies should be adopted depending on the source of the losses to increase the efficiency of PEM fuel cells. The remedy for the activation loss is to make better catalysts, which is represented by high i_0, while the mass transport loss can be alleviated by improving the design of the gas diffusion layer and the current collector combined with optimized operating conditions. The ohmic loss is closely related to the proton conductivity of the membrane, σ_{proton}, and is believed to be much smaller than other losses.[4]

In order for PEM's to have enough proton conductivity, however, a proper management of water is required because most of available PEM's rely on water to conduct protons.[5] The aim of the water management is to make a fuel cell system operated with just a right amount of water that allows enough proton conductivity of the membrane, but does not cause flooding. When too much water exists in the system, flooding takes place and hinders the reactant gases from accessing the reaction sites, which causes the mass transport loss. Proper water management frequently requires external humidification systems or large blowers to remove excess water which are adverse to efficiency and increase the volume of the fuel cell system. In addition, the operating temperature of the fuel cell is limited below ~80 °C to prevent excessive evaporation of water from the membrane. One solution to this problem is to develop an alternative proton exchange membrane which can be operated at a higher temperature without relying on the environmental humidity for their proton conductivity. In spite of a variety of efforts to develop PEM's for high temperature operation and the existence of promising candidates,[5-7] the conventional perfluorosulfonic acid (PFSA) polymers are still widely used because the gain from the increased proton conductivity of alternative membranes at high temperature has not yet exceeded the performance of the conventional ones operated with a proper water management system at low temperature.

1.2 Nafion® and Water

Nafion®, a trademark of Dupont, is a type of PFSA polymer most widely used for PEM fuel cells and serves as a reference material to which new types of membranes are compared.[8,9] Nafion® provides decent chemical and mechanical stability as well as proton conductivity[8,10,11] owing to the unique structure shown in Figure 4.

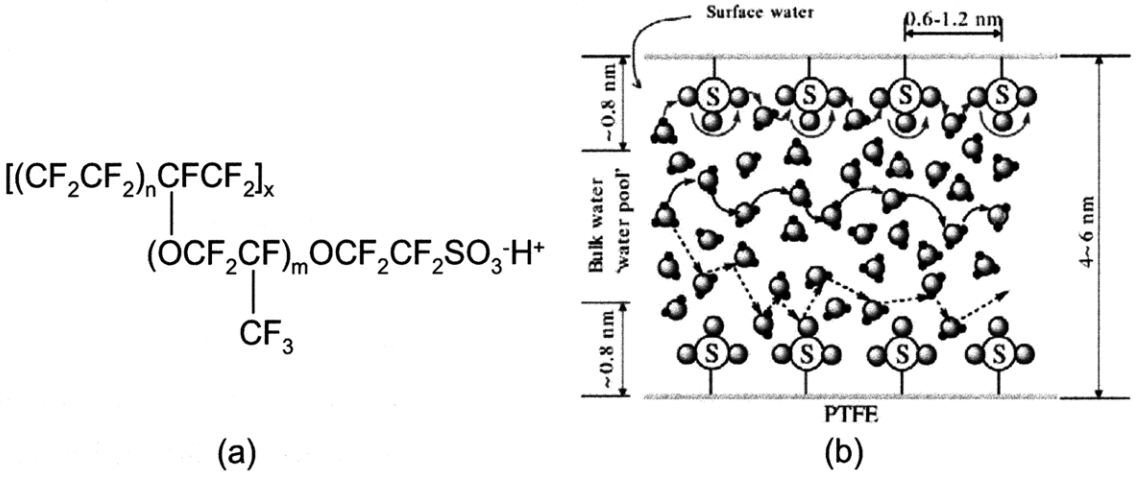

Figure 4. (a) The general structure of a Nafion® membrane, adapted from the Reference.[12] (b) A simplified picture of structure and proton transfer in Nafion® in fully hydrated state, reprinted from the Reference.[13]

Nafion® is composed of hydrophobic backbones, hydrophilic end groups with SO_3^-, and side chains connecting the two. While the backbones which have a similar structure to that of Teflon® (Dupont) contribute to mechanical, thermal, and chemical stability of Nafion®, the hydrophilic end groups act as anchor points for protons and hydroniums and attract water molecules. These water molecules form clusters or channels through which protons can move by vehicular and Grotthuss mechanisms.[13,14] This is the reason why proton conductivity of Nafion® is greatly dependent on its water content,[12,15-17] which is balanced by two mechanisms: diffusion due to concentration gradient and electro-osmotic drag.[16,18] Although the presence of water in Nafion® is indispensable for the proton conductivity, it causes a problem, swelling. It is known that Nafion® membrane can swell up to 15 % due to water uptake compared to its dry state in both length and thickness.[19] The swelling of Nafion® membranes can cause mechanical stresses[20,21] when they are

confined between current collectors and the repeated cycling of hydration and dehydration, which is commonly expected for the case of automotive applications, will eventually result in the failure of membranes. Therefore, the transport of water plays a crucial role in the performance and the durability of Nafion® membranes, and two important parameters for describing Nafion® are the equivalent weight (*EW*) and the water content (λ). *EW* is defined as the weight of dry Nafion® per mole of SO_3^- and is inversely proportional to the density of the fixed charge (SO_3^-). *EW* of Nafion® is determined depending on the manufacturing process and has the typical value of 1100 g/mol-SO_3^-. Nafion® with lower *EW* absorbs more water and shows higher proton conductivity than one with higher *EW*. λ is defined as the number of water molecules per SO_3^- and most properties of Nafion® change as a function of the water content.[8]

1.2.1 Microscopic Model of Nafion®

Microscopic models of Nafion® are necessary to explain how water molecules form clusters or channel in Nafion® at different hydration levels and how water molecules and protons transport in the structure. There have been a lot of microscopic models of Nafion® that were derived from experimental results of both microscopic and macroscopic observations.[22] One of the very common macroscopic observations is the increase of proton conductivity with increasing water content as reported by many researchers.[12,15-17] The dependency of the proton conductivity on the water content clearly suggests that protons move through the clusters or channels of water of which the density will increase with the water content. In other words, initial water molecules taken by Nafion® start to associate with the hydrophilic parts and form small clusters which are not yet connected very well and result in the minimal proton conductivity at low water content. As more water molecules come into the structure, the size of clusters gets bigger and more clusters are connected each other, which increases the proton conductivity significantly. However, there is an upper limit of the water content because the hydrophobic parts of Nafion® are cross-linked and can not expand any more than a certain degree. Also the proton conductivity through only the connected water clusters and channels can not exceed that of pure water, which is 2.38 S/cm.[23] Consequently, the averaged proton conductivity of the polymer and water has a maximum value of ~0.1

S/cm as shown in Figure 5.

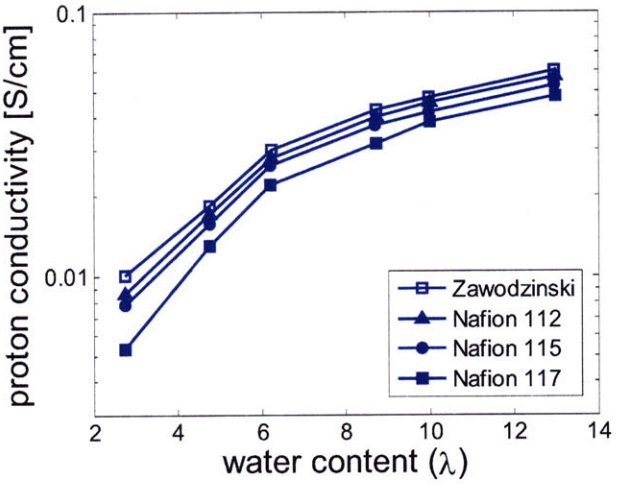

Figure 5. Proton conductivity of Nafion® membranes as a function of water content. Reprinted from the Reference[15] which includes the data from Zawodzinski.[16]

It is noted that the data shown in Figure 5 includes the proton conductivity measured at the water content of up to 13, which is obtained from a Nafion® equilibrated in water vapor with the activity of 1. Nafion® equilibrated in liquid water can reach the water content of ~22 at which the proton conductivity approaches to 0.1 S/cm. The difference in the water content of Nafion® equilibrated in saturated vapor and liquid water is called Schroeder's paradox, because the water activities of both saturated vapor and liquid are 1 but result in quite different water contents (~13 vs. ~22).[24] The evolution of the clusters and the channels of water in Nafion® contacting with vapor or liquid water was well described by Weber,[25] which is summarized in Figure 6. When Nafion® contacts with water vapor, absorbed water molecules solvate the sulfonic acid groups which form inverted micelles and small water clusters. At this stage, the distance among the clusters is too far to form channels ($\lambda < 2$). As Nafion® takes more water molecules, the size of these clusters grows and the distance among them decreases enough to form channels which are less hydrophilic compared to the clusters ($\lambda = 14$). When Nafion® is in contact with liquid water, the surface undergoes structural reorganization so that the hydrophobicity of the surface is reduced and the barrier keeping water from infiltrating is

lowered. Then, the already formed clusters and channels are filled with more water molecules and expand ($\lambda = 22$).

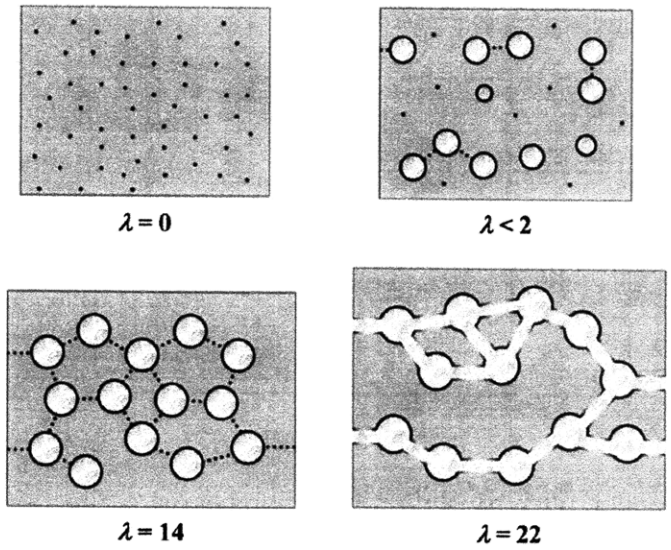

Figure 6. Evolution of the membrane structure as a function of water content, λ. The pictures are cross-sectional representations of the membrane where the gray area is the fluorocarbon matrix, the black is the polymer side-chain, the light gray is the liquid water, and the dotted line is a collapsed channel. Reprinted from the Reference.[25]

Even though the microscopic model by Weber[25] provides the qualitative information on the behavior of Nafion® swelling as a function of the water content, it lacks a detailed and quantitative description of Nafion®, such as the size of the water clusters, the distance among them, and the width of the water channels, which will complete the microscopic model. For this purpose, the microstructure of the water clusters and channels have been studied by atomic force microscopy (AFM)[26-29] and small angle x-ray scattering (SAXS).[26,30-34] James[26] used AFM in tapping mode and SAXS to identify the hydrophilic and hydrophobic regions of Nafion® and found that the spacing between the clusters ranged between 3~5 nm and the cluster size range from 5 nm to 30 nm. McLean[28] also examined Nafion® using AFM and observed that the hydrophilic domain size of 4~10 nm in room humidity increased to 7~15 nm under liquid water. These observations also agree well with the findings of the AFM study done by the author of this thesis as shown in Figure 7.

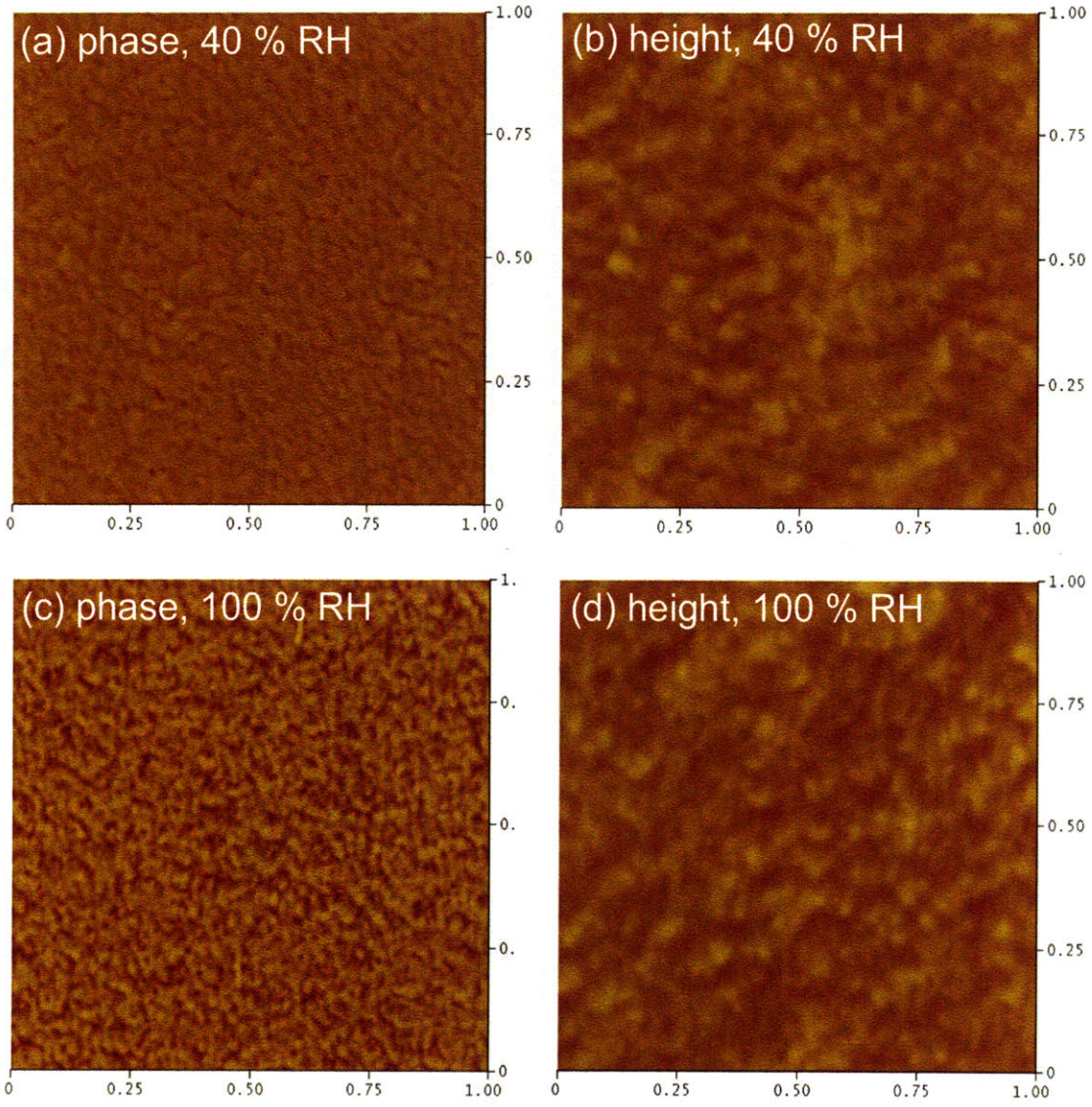

Figure 7. AFM images (tapping mode, setpoint amplitude / RMS amplitude = 1.45 V / 1.80 V, data scale of phase image = 60°, data scale of height image = 50 nm) of the surface of a Nafion® 112 membrane (1 μm × 1 μm). (a) Phase image at 40 % RH. (b) Height image at 40 % RH. (c) Phase image at 100 % RH. (d) Height image at 100 % RH. RH was controlled by flowing argon gas saturated with water vapor at room temperature.

The different interaction of hydrophilic and hydrophobic domains with the AFM tip caused the contrast in the phase images and the darker regions indicated hydrophilic domains. It is clear that more hydrophilic domains were developed and connected with each other in the case of 100 % RH than the case of 40 % RH, while the height images

did not show a noticeable difference, which confirmed that the contrast in the phase images was not affected by the physical roughness of Nafion®. The size of hydrophilic domains increased from 4~8 nm up to 16 nm as RH increased.

The more detailed structure of Nafion® in sub-nanometer scale can be found by analyzing SAXS spectrum. Studies by Diat el al.[30-34] revealed that 1) Nafion® membranes have an intrinsic fibrillar structure with cylindrical aggregates screened by ionic charges, 2) these aggregates have a coherent length on the submicrometer-scale, and 3) water uptake in the Nafion® membranes is not confined in spherical cavities but among fibrillar objects and becomes one continuous medium at high hydration levels. Figure 8 shows a schematic of Nafion® structure proposed by Gebel and Diat[31]

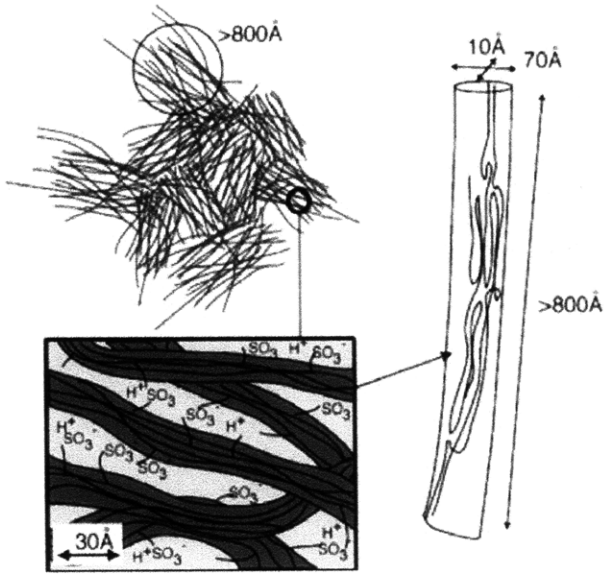

Figure 8. Schematic representation of the Nafion® membrane structure at different scales. Reprinted from the Reference.[31]

The microscopic models proposed by Weber[25] and Gebel[31] look quite different in the sense that the former used a spherical shape for the water clusters and the latter proposed cylindrical aggregates with ionic charges where water molecules agglomerate. Nevertheless, it is still valid that a Nafion® membrane has a fixed number of sulfonic groups bound to the polymer matrix and the phase separation between water clusters and the polymer matrix occurs as the water content increases, even though the shapes of the

water clusters and the connecting channels are debatable.

As mentioned earlier, the transport of protons occurs through the paths formed by water molecules. Protons move through the water channel in the form of hydroniums (H_3O^+) rather than by itself.[35] The pathway of proton transport can be divided into two.[13,36] One is along the interface between the hydrophobic and hydrophilic domains where protons or hydroniums are more strongly bound to the fixed sulfonic ions (SO_3^-) and the proton transport is dominated by surface diffusion. The other pathway is through the center of the water channel where the water molecules are similar to bulk water and protons can move by bulk diffusion or Grotthuss mechanism, which is the hopping of a proton from a hydronium to a neighboring water molecule. It is believed that Grotthuss mechanism is much faster than surface diffusion which should overcome the strong electrostatic attraction from the sulfonic ions and the long distance between them, and bulk diffusion which is retarded by the fluidic friction among hydroniums and water molecules.[37] Because of this, the proton conductivity of Nafion® become high only when it has enough water content which enables proton transport by Grotthuss mechanism. Choi[13] proposed the following equation for the proton conductivity of Nafion®, which incorporate the three mechanisms of the proton transfer based on the Nernst-Einstein relation:

$$\sigma_{H^+} = \frac{\varepsilon}{\tau}\left[\frac{F^2}{RT}\left(D^{\Sigma}_{H^+}c^{\Sigma}_{H^+} + D^{G}_{H^+}c_{H^+} + \frac{D^{W}_{H^+}}{1+\delta_c}c_{H^+}\right)\right] \qquad \text{Eq. 8}$$

ε is the volume fraction of water to the total volume and τ is the tortuosity factor which is related to the microstructure of Nafion®. $D^{\Sigma}_{H^+}$ and $c^{\Sigma}_{H^+}$ are the surface diffusion coefficient and the concentration of proton along the interface between the hydrophilic and hydrophobic domains, respectively. $D^{G}_{H^+}$ and c_{H^+} are the diffusion coefficient for Grotthuss mechanism and the concentration of proton in the middle of the water clusters or channels. $D^{W}_{H^+}$ is the diffusion coefficient of hydronium in bulk water and δ_c is defined as $(D^{W}_{H^+}/D^{M}_{H^+})[(1-x)/x]$, where $D^{M}_{H^+}$ is the diffusion coefficient of proton through the polymer matrix and x is the mole fraction of water. In other words, $D^{W}_{H^+}/(1+\delta_c)$ represents an equivalent diffusion coefficient that is averaged by mole

fractions of water and the polymer. Therefore, the description of the proton transport in Nafion® is very complicated and the fact that all the parameters in Eq. 8 vary as a function of the water content adds more complexity.

On the other hand, the transport of water molecules in Nafion® is governed by two mechanisms: diffusion and electro-osmotic drag.[17,38] Diffusion of water molecules occurs under the presence of the gradient in the chemical potential or the concentration. The diffusion coefficient of water can be determined by considering the self-diffusion coefficient, D_{self}, and the thermodynamic enhancement factor or the Darken factor:

$$D = D_{self} \frac{\partial \ln a_w}{\partial \ln \lambda}, \qquad \text{Eq. 9}$$

where D is chemical diffusion coefficient, which dictates the net flux of water under the concentration gradient. $\partial \ln a_w / \partial \ln \lambda$ is the Darken factor and can be evaluated from the relationship between the activity of water and the water content of Nafion® membranes or the data on the equilibrium sorption of water as a function of the activity. The detailed derivation of Eq. 9 and the discussion on the relationship between D and D_{self} can be found in Appendix B and Chapter 6. D_{self} is associated to the microstructure of Nafion® membranes and also varies as a function of water content like the proton conductivity because the self-diffusion mechanism of water is similar to the diffusion mechanism of protons which move with water molecules in the form of hydroniums. Based on the free volume approach, Yeager proposed the following expression to relate the volume fraction of the polymer, V_p, to D_{self}:

$$D_{self} = D_{self,0} \exp\left[\frac{-bV_p}{(1-V_p)}\right], \qquad \text{Eq. 10}$$

where $D_{self,0}$ is the self-diffusion coefficient of pure water or 2.3×10^{-9} m^2/sec at 25 °C[39] and b is a parameter determined by fitting to experimental data. Even though Eq. 10 well predicted that the log of the experimentally measured D_{self} was proportional to the ratio of volume fractions, $V_p/(1-V_p)$, the estimation of D_{self} was not accurate. This is because not all the water molecules represented as $(1-V_p)$ behave in the same manner regarding the diffusion. When the water content of Nafion® is small, the water molecules in the polymer matrix are strongly bound to the ionic groups and the mobility of these water molecules is considerably smaller than that of free water molecules. As the water content

increases, the polymer matrix expands or swells to incorporate more water molecules which form clusters or channels and have higher mobility than that of strongly bound water molecules. Consequently, Eq. 10 can be modified to consider water molecules which can actively participate in the diffusion as follows:

$$D_{self} = D_0 \exp\left[\frac{-bV_p}{(1-V_p)f_d}\right], \qquad \text{Eq. 11}$$

where f_d is the fraction of water molecules which have the mobility of free water and has the value between 0 and 1 depending on the total water content. f_d is close to 0 when the water content is low, while it approaches to 1 as the water content increases. However, the determination of the accurate f_d as a function of the water content would be possible only after a comprehensive description of the complex microstructure of Nafion® and its interaction with water molecules in the wide range of the water content.

The second mechanism of the water transport in Nafion®, electro-osmotic drag, means the transport of water molecules induced by the transport of protons without the gradient in the chemical potential, but under electrical potential. Proton transport by Grotthuss mechanism does not contribute to electro-osmotic drag, where only protons move between neighboring water molecules which are considered stationary. However, proton transport as a form of hydroniums by diffusion will cause electro-osmotic drag. When water molecules are transported by this physical motion of hydroniums, there are two factors contributing the movement of water molecules.[14] One is simply the transport of hydroniums which include water molecules in them and the other is the transport of water molecules outside of these moving hydroniums dragged by fluidic friction. Again, the water transport by electro-osmotic drag is greatly affected by the water content. When the water content is low, the proton conduction is dominated by the diffusion mechanism, which causes the transport of water molecules, since the Grotthuss mechanism is active only with enough free water molecules. However, in the case of the low water content, there are a relatively small number of available water molecules represented by f_d, which makes both the proton conduction and the electro-osmotic drag difficult. As the water content increases, the Grotthuss mechanism takes over the proton conduction and a large portion of the proton conduction does not involve the transport of water molecules. At the same time, protons can be still transferred by the diffusion mechanism to a certain degree,

which is now much easier to occur due to the abundance of free water molecules compared to the case of the low water content. In addition, it is possible for protons to form not only hydroniums (H_3O^+), but also Zundel ($H_5O_2^+$) or Eigen ($H_9O_4^+$) ions if a large amount of free water molecules are available around protons[38]. Therefore, the high water content is favorable for both the Grotthuss mechanism which does not induce the electro-osmotic drag, and the diffusion of protons hydrated with multiple water molecules which enhances the electro-osmotic drag. The coefficients of the electro-osmotic drag (*EOD*), which is the number of water molecules moved with a proton, are the result of the two competing factors.

$$j_{water} = EOD \cdot j_{proton,total} = \beta \cdot j_{proton,diffusion} \qquad \text{Eq. 12}$$

$$EOD = \beta \frac{j_{proton,diffusion}}{j_{proton,total}} \qquad \text{Eq. 13}$$

where β is a parameter defining the number of water molecules moving with a proton transferred by the diffusion mechanism through the bulk water in clusters or channels. The second term of Eq. 13 is the ratio of the proton flux caused by the diffusion to the total proton flux, which will decrease as the water content increases due to the increased contribution of the Grotthuss mechanism while β will increase with the increased number of water molecules around a moving proton. Eq. 13 can be rewritten by combining Eq. 8:

$$EOD = \beta \frac{\frac{D_{H^+}^W}{1+\delta_c} c_{H^+}}{\left(D_{H^+}^{\Sigma} c_{H^+}^{\Sigma} + D_{H^+}^G c_{H^+} + \frac{D_{H^+}^W}{1+\delta_c} c_{H^+} \right)} \qquad \text{Eq. 14}$$

It is noted that all the parameters of Eq. 14 vary as a function of the water content and the quantitative determination of these parameters and the experimental validation will be very challenging.

In summary, the mechanism of proton and water transport in Nafion® has not been fully understood because of the lack of the comprehensive knowledge on the microstructure of Nafion® and the interaction among the polymer matrix, protons, and water molecules which are highly coupled to each other. The first step to be taken towards the goal of understanding Nafion® would be accurate measurements of the fundamental transport properties, such as the coefficients of diffusion and electro-osmotic

drag, which can provide clues to the goal. Furthermore, the information on these properties will be useful for optimizing the design and the operating conditions of fuel cells to increase the efficiency.

1.2.2 Mechanism of Nafion® Degradation

Besides the fact that the proton conductivity of Nafion® is greatly dependent on the water content, another important issue to consider when Nafion® membranes are used for fuel cells is the durability because the failure of the membranes will result in the low efficiency or sometimes a catastrophic drop in the performance once pinholes and cracks are developed. It is known that Nafion® membranes can degrade from multiple reasons, which can be categorized into mechanical, thermal, and chemical degradation mechanisms.[40-42]

Mechanical degradation is closely related to the swelling of Nafion® membranes due to water uptake. It is well known that Nafion® membranes equilibrated in liquid water can swell up to 15~20 % in both thickness and length. Morris[19] measured the changes in the thickness and the length of a Nafion® 117 membrane as a function of water content and a linear relationship among them was found, as shown in Figure 9.

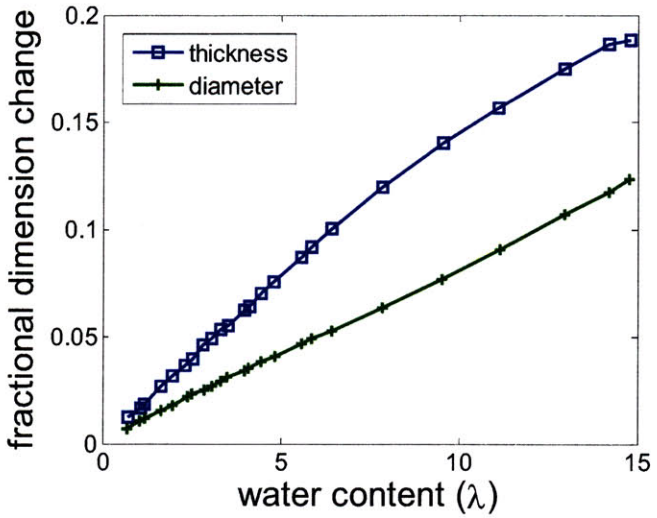

Figure 9. Fractional dimension changes of a Nafion® 117 membrane as a function of water content. Adapted from the Reference.[19]

The problem of mechanical stress arises from the fact that Nafion® membranes are

confined in fuel cells where the membranes can not swell or shrink freely. The spatially non-uniform contact between the membrane electrode assembly and the corrugated current collectors may cause concentrated stresses along the edges between the contacting and non-contacting areas. Operating fuel cells with no or low humidification[43-46] and cycling of relative humidity (RH)[20,47] can accelerate the mechanical degradation. Tang[47] tested the effect of RH cycling and found that the hydrogen crossover current density increased significantly after 3000 times cycling of a Nafion membrane between the water soaked state and 25 % RH as shown in Figure 10, which indicated the mechanical breach and failure of the membrane resulted from the relatively high tensile stress of 2.23 MPa compared to the other cases of less severe hydration cycling.

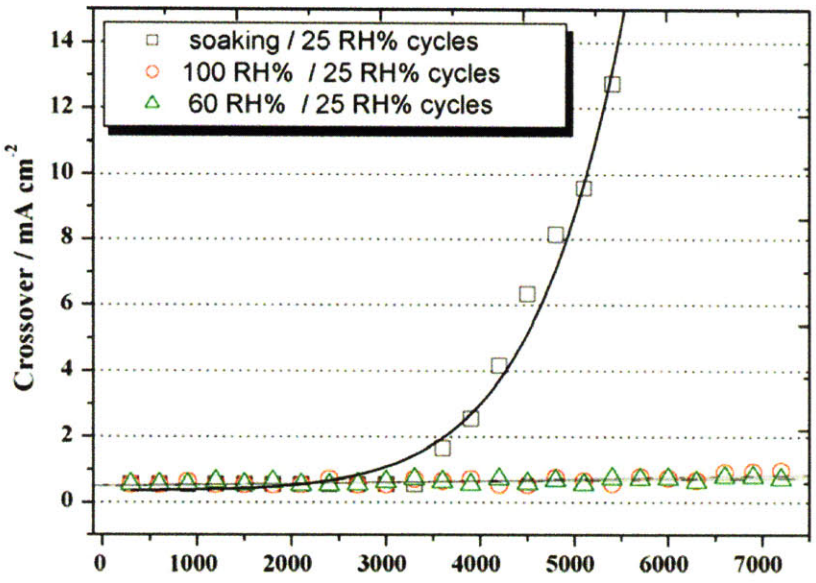

Figure 10. H_2 crossover current density of Nafion® membranes as a function of the hydration cycles. Reprinted from the Reference.[47]

The thermal stability of Nafion® has been examined by thermogravimetric analysis (TGA).[48-51] Wilkie[51] found that Nafion® was quite stable until 380 °C where fluorocarbon radicals, SO_2, and hydroxyl radicals started to be produced. The thermal stability of Nafion® up to 280 °C and then the breach of sulfonic groups and oxidative destruction were observe by Surowiec[50] and Samms.[48] Even though the thermal stability of Nafion® is quite good considering that the typical operating temperature of fuel cells is 80 °C, thermal degradation can result from thermal cycling, which affects Nafion®

membranes in a similar way to that of RH cycling via thermal expansion, and the exposure to high temperature for long time. In addition, operating fuel cells below 0 °C can damage the membrane due to freezing of water remaining in the membranes.[52-55]

It is believed that Nafion® membranes can be chemically degraded by active oxygen species, such as peroxide and hydroperoxide radicals.[56,57] The chemical degradation by these attacking agents can be severe when fuel cells are operated at OCV with low RH.[46,58] However, it is not clearly understood where and how these radicals are generated. They can be formed as the by-products of the oxygen reduction reaction at the cathode or as a result of the cross-over of the reactant gases. Huang[58] showed that the chemical degradation was initiated from the anode side, while Pozio,[59] Stucki,[60] and Yu[61] found that the degradation in the cathode side was more dominant. Mattsson[62] did not observe significant difference between the cathode and anode degradation. Contaminants, such as metal cations, from the reactant gases or other components of the fuel cell also can accelerate the chemical degradation by two mechanisms. First, many metal cations have stronger affinity to the sulfonic groups in Nafion® than protons and can replace them. Consequently, the mobility of protons and water molecules decreases resulting in the performance loss of the fuel cell.[63] The second mechanism is the effect of metal cations catalyzing the formation of radicals, which chemically attack the membrane.[59,64]

It is noted that all the degradation mechanisms of Nafion® membranes can take place simultaneously during the fuel cell operation. Even though it is difficult to determine which degradation mechanism dominantly contributes to the failure of the membranes, the management of water can affect all of them directly or indirectly. RH cycling and the corresponding swelling of the membrane can directly affect the compressive or tensile stresses. The thermal degradation can be accelerated if the membrane is exposed to high temperatures without water in it, which can soften the membrane and absorb heat by evaporation. In addition, freezing of water below 0 °C will directly damage the membrane. As for the chemical degradation, the existence of water can facilitate the chemical reactions of the attacking agents by assisting the transport of them. Therefore, the mechanical, thermal, and chemical degradation can be accelerated and cause earlier failure of Nafion® membranes without a proper water management. For example, Knights[43] reported that a fuel cell operated at well humidified conditions

showed a much longer lifetime than one operated at dry conditions. The opposite result may be expected from the fact that well humidified membrane is under higher compressive stress due to greater swelling and exposed to more of chemically attacking agents, such as active oxygen species,[65,66] that may gain more mobility in humid environment than dry conditions. Based on the contradiction, it can be hypothesized that the temporal and spatial non-uniformity in the water content of membrane, which can develop easily under a dry operating condition due to the localized formation of water in the cathode, is more responsible for the degradation of membrane than other effects, as illustrated in Figure 11.

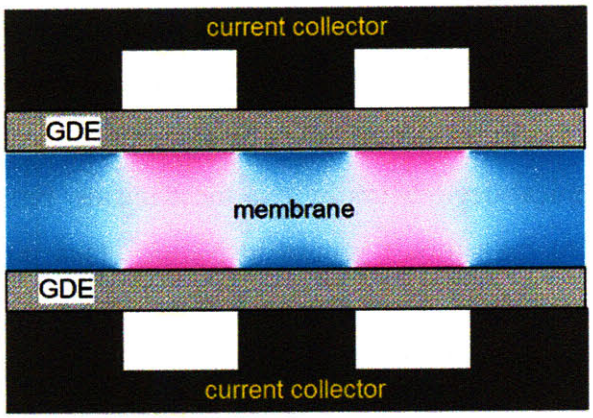

Figure 11. Hypothetical distribution of mechanical stress caused by the non-uniformity in water content of the fuel cell membranes.

Therefore, the verification of this hypothesis and moreover the understanding of the membrane degradation mechanism require the measurement of the water content with temporal and spatial resolutions

1.3 Motivation of the Thesis

From the previous section, it is evident that the proton conductivity of Nafion® membranes is closely related to the water content due to the coupled mechanism of proton and water transport, and the lifetime of the membrane can be shortened by improper water management. Therefore, to understand the mechanism of water transport in Nafion® membranes is crucial to accurately estimate the performance and the

durability of PEM fuel cells and more importantly to develop a new fuel cell system with a better efficiency and a longer lifetime

There have been a great amount of researches to study the relationship between Nafion® and water, including various types of proton conductivity tests as a function of water content,[10,12,15-17,67-70] the measurements of water diffusion coefficients,[16,19,71-76] and measurements of electro-osmotic drag coefficients.[18,77-82] However, the true understanding of the water transport mechanism can not be accomplished without the information on how the water content of Nafion® membranes changes during the operation of the fuel cell temporally and spatially. For this purpose, various types of in-situ monitoring techniques have been developed to measure the water content of fuel cell membranes directly or indirectly. Most of indirect studies relied on the fact that the proton conductivity of Nafion® can be related to its water content and utilized segmented current collectors to measure local current densities.[83-86] Drawbacks of indirect methods are insufficient spatial resolution due to the limited degree of segmentation and the uncertainty resulting from the relationship between water content and local conductivity which may include the effects of contact resistance. The typical spatial resolution of this type of techniques is limited to the width of the flow channels (~1 mm) and it is difficult to capture the spatial variation of the water content near the interface between the land area and the channel area of the current collectors. As for direct measurements, the method of using transparent fuel cells and visible lights has been tried, which has enough spatial and temporal resolutions.[87,88] However, the electrodes of these fuel cells are still opaque and the information obtained is limited to liquid water accumulated in flow channels. Although neutron imaging is a powerful tool to visualize water existing in fuel cells,[89-93] it is not easy to resolve subtle changes in thin membranes, typically thinner than 200 μm, with a sufficient temporal resolution due to the tradeoff between temporal and spatial resolutions of this technique. Because of this, the observations by neutron imaging technique are limited to either steady states with high spatial resolution (16.4 μm, 8.33×10^{-4} Hz)[89] or transient states with poor spatial resolution (250 μm, 1 Hz).[92]

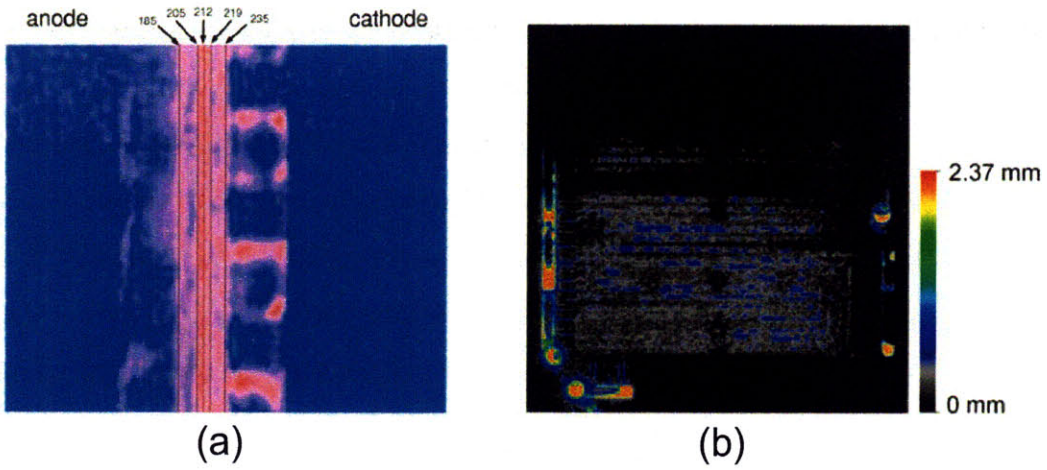

Figure 12. Neutron images with the spatial resolutions (a) 16.4 μm, reprinted from the Reference[89] and (b) 250 μm, reprinted from the Reference.[92]

Magnetic resonance imaging (MRI)[94-96] and small-angle neutron scattering (SANS)[97] have been also used to measure water content in fuel cell membranes, which have similar limitations to those of neutron imaging. Even though Zhang[94,95] recently reported the spatial and temporal resolution of less than 8 μm and 2 min by using the MRI technique, the temporal resolution was not still enough to resolve the transient behavior of water within Nafion® membranes and only qualitative data of water content were provided in arbitrary units. Patil[98] used a Nafion® membrane containing a fluorescence dye and an optical fiber to detect the fluorescence signal sensitive to water content of the membrane. This technique had a high temporal resolution of 1000 Hz, but the spatial information was very limited because only one optical fiber was imbedded in the membrane.

When the variations in the water content are assumed to be governed by the diffusive motion of water molecules, the variations will take place in the time and the length scales related to each other by $\Delta t = (\Delta x)^2 / D$. Since the diffusion coefficient, D, is $\sim 10^{-10}$ m^2/sec,[16] the detection of the transient response of Nafion® membranes during water uptake or loss will typically require the temporal and spatial resolutions of ~1 Hz and ~10 μm, respectively. Alternatively, the combination of ~0.01 Hz and ~100 μm can be used, but this will lead to unreasonably long observation time and also the failure to detect the fine details of the water content variations occurring within ~100 sec or ~100 μm. None of previous techniques, to the knowledge of the author, provided enough

resolutions in both time and space to detect the transient response of Nafion® membranes. This motivated the aim of this thesis, which is the development of a new measurement system to detect the water content of Nafion® membranes with adequate temporal and spatial resolutions for better understanding the mechanism of the water transport.

1.4 Approach and Outline of the Thesis

In order to accomplish the aim, laser interferometry is used to detect the changes in the optical path length of Nafion® membranes as a function of time and position. Since the optical path length, which is the product of the refractive index and the thickness, will change with the water content, the analysis of the corresponding interference pattern will allow the reconstruction of the changes in the water content during the process of water uptake or loss of Nafion® membranes. The developed laser interferometry technique is used for two purposes: 1) the evaluation of the fundamental properties of water transport and 2) in-situ monitoring of the water content of a Nafion® membrane assembled in a fuel cell.

In Chapter 2, the instrumentation of the Mach-Zehnder interferometer is presented with experimental results to show the correlation between the measured interference pattern and the optical path length (*OPL*) of Nafion® membranes. From the correlation, a computational algorithm for the automated retrieval of the *OPL* is made, which enables the visualization of the changes in water content.

In Chapter 3, the relationship between the *OPL* and the water content is determined for the quantitative measurement of water content. For this, ellipsometry as well as interferometry on Nafion® is performed to measure the individual effect of the refractive index and the thickness on the *OPL*. The experimentally determined relationship is also checked by a mathematical model.

In Chapter 4, the effect of the compressive pressure on the *OPL* is considered, which defines the uncertainty of the direct conversion between the *OPL* and the water content. The effect of pressure is experimentally examined by laser interferometry with phase shifting and also confirmed by a model.

In Chapter 5, the mathematical procedures for calculating the coefficients of diffusion and electro-osmotic drag using the data measured by the interferometry are

introduced. The validity of the mathematical schemes is checked by simulational experiments. In addition, the tolerance to the potential noise in the measured data is checked by numerical simulations.

In Chapter 6, the results of diffusion experiments are presented, which allows the evaluation of the effect of compressive stress on the speed of diffusion using the method developed in Chapter 5. In addition to the data of water diffusion, the results of methanol diffusion experiments are given in order to confirm the findings from the water diffusion experiments. The relationship between the chemical and the self diffusion coefficients is considered to have a better idea on the effect of compressive stress.

In Chapter 7, the results of electro-osmotic drag experiments are presented and the coefficients of electro-osmotic drag are evaluated using the method introduced in Chapter 5.

In Chapter 8, the laser interferometry technique is applied to measure the water content of a Nafion® membrane assembled in a fuel cell. For this, the effect of temperature on *OPL* is examined because a fuel cell during the operation may experience temperature changes.

Finally, Chapter 9 summarizes the accomplishments and the findings of this thesis and provides the perspectives of the developed technique.

Chapter 2. Visualization of Water Content with Spatial and Temporal Resolutions

Laser interferometry can detect the changes in the water content of Nafion® membranes with adequate temporal and spatial resolutions to study the transport mechanism of water. As the water content of a Nafion® membrane changes, the refractive index (n) and the thickness (d) of the membrane will change correspondingly. Since an interferometer can measure the variations in optical path length, ($n \times d$) as a function of time and position, it is possible to back-calculate the water content once the relationship between the water content and the optical path length of Nafion® is established. Because this technique relies on the changing rate of interference signal rather than intensity itself, data acquisition is instantaneous and the temporal and spatial resolutions are solely dependent on the refresh rate and the pixel pitch of a camera used for detecting the interference signal. This chapter presents the procedure for converting interference data measured from a Nafion® membrane taking water by diffusion mechanism to the changes in optical path length, including the experimental setup, the acquisition of data, and the method of signal processing.

2.1 Experimental

A Mach-Zehnder interferometer shown in Figure 13 was used to detect changes in the optical path length of Nafion® membrane. A He-Ne laser beam (Thorlabs, HPR170) was expanded to about 1 inch diameter through a spatial filter (Newport, 900) and a plano-convex lens (Newport, KPX201AR.14). The resulting bundle of parallel rays was divided into two identical beams at the first beam splitter (Newport, 20BC17MB.1). One beam penetrated through a Nafion® membrane and picked up phase delay corresponding to the optical path length of the membrane. The other was reflected at a mirror (Newport, 20D10DM.4) and went through the air, which had the constant refractive index of 1 and served as a reference medium. These two beams were recombined at the second beam splitter to interfere with each other and the corresponding intensity was detected by a CMOS sensor (Basler, A504k). The sensor had the area of 15.4 mm * 12.3 mm with 12 μm pixel pitch and the refresh rate of 500 Hz, which was tunable down to 0.1 Hz. The

optical path lengths of the area of interest in Nafion® samples were monitored simultaneous.

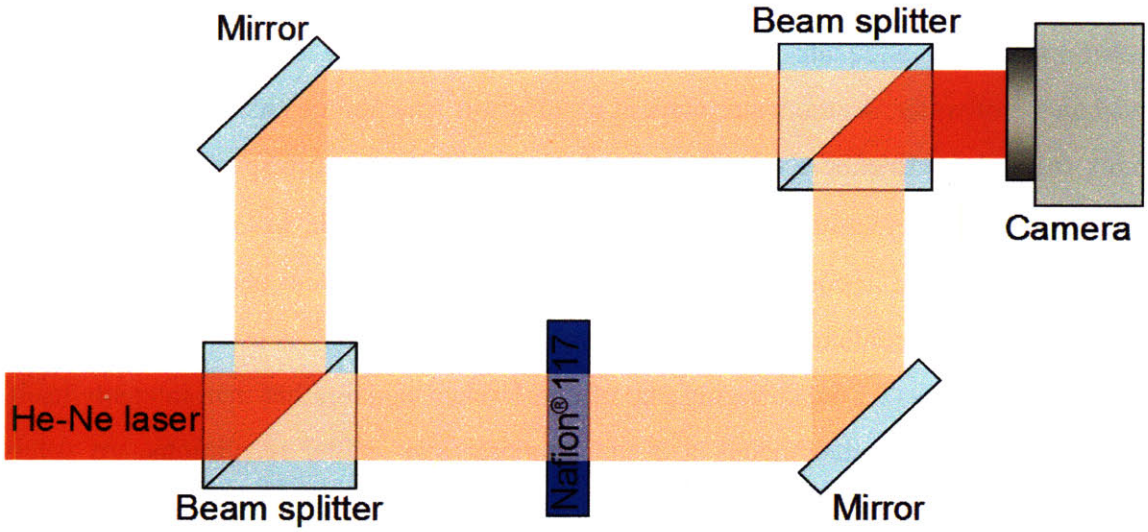

Figure 13. Mach-Zehnder interferometer composed of 2 beam splitters and 2 mirrors. Probing beam passes through Nafion® samples and interferes with reference beam. Resulting interference is recorded by a digital camera.

Nafion® 117 membranes were prepared by boiling sequentially in 3 % H_2O_2, 0.5 M H_2SO_4, and deionized water for 1 hour each, and then stored in deionized water till interferometry experiments. Diffusion of water into Nafion® was introduced by immersing the bottom side of an initially dry membrane into liquid water as shown in Figure 14. A dry Nafion® sample was prepared by storing it in a drying oven at 50 °C for 24 hours. Two glass plates sandwiched the Nafion® sample to keep it flat during the optical measurement and prevent evaporation of water from the surface, which ensured one dimensional diffusion of water. Special attention was paid to prevent water from wicking in-between the glass plates and the sample membrane so that the water uptake of the sample was solely the result of diffusion. The variation in the interference intensity during this diffusion process was monitored by the interferometer as a function of time and position.

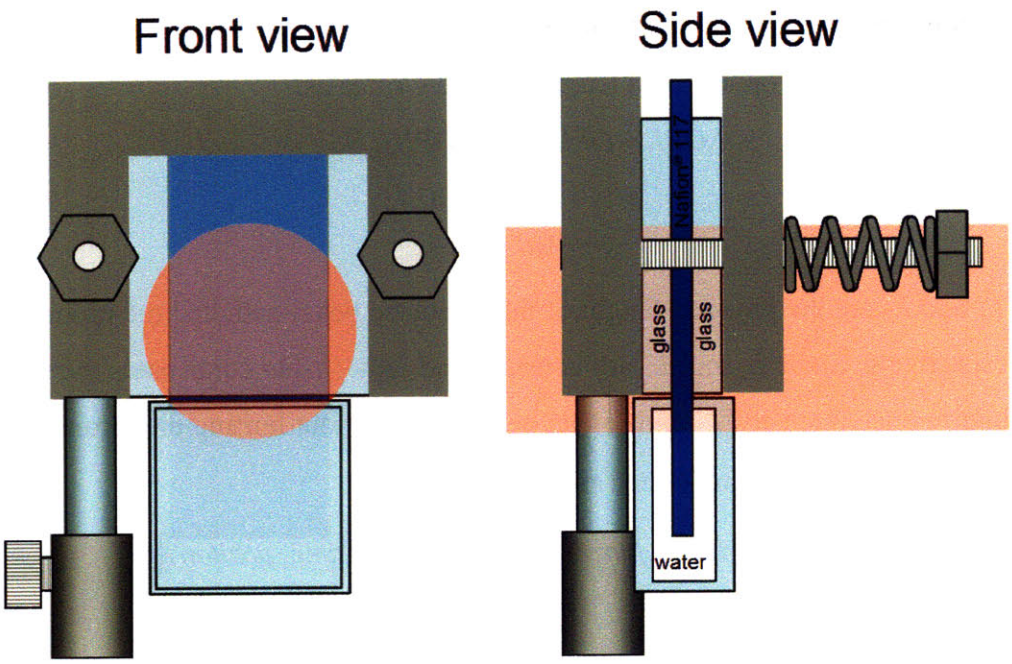

Figure 14. Nafion® sample holder for diffusion experiments. A Nafion® 117 membrane is clamped between two glass plates which keep the membrane flat during water uptake and prevent evaporation of water. Clamping pressure is controlled by two compressive springs. A water chamber is attached to the bottom side of Nafion® sample, which causes gradient in the water content and diffusion. The red shade indicates the location of the probing laser beam.

2.2 Optical Signal Processing

A Nafion® 117 sample was allowed to absorb water from the bottom for 10 hours and the corresponding interference intensities at selected positions as a function of time are shown in Figure 15. It is clear that the frequency of intensity oscillation decreased as the distance from the liquid water increased. These intensity variations are related to the changes in optical path length through the following equation:

$$intensity \Leftrightarrow \cos\left(\frac{\Delta OPL(time, position)}{wavelength} 2\pi\right), \qquad \text{Eq. 15}$$

where ΔOPL is the difference in optical path lengths of the reference beam and the probing beam of the Mach-Zehnder interferometer. While the optical path of the reference beam goes through the air of which the refractive index is constantly 1, the optical path length of the probing beam changes depending on the changes in thickness

and refractive index of the Nafion® membrane as a function of time and position. In other words, the difference in optical path lengths can be written as:

$$\begin{aligned}\Delta OPL &= OPL_{probing} - OPL_{reference} \\ &= [1\cdot(L_2 - d) + n\cdot d] - 1\cdot L_1 \\ &= (n-1)d + L_2 - L_1\end{aligned} \qquad \text{Eq. 16}$$

where L_1 and L_2 are the physical length of the reference beam path and the probing beam path, respectively. Since L_1 and L_2 are constant and only $(n\text{-}1)d$ contributes the variation in the interference intensity, L_1 and L_2 can be omitted without hurting the meaning of Eq. 16. For simplicity, ΔOPL is redefined as:

$$\Delta OPL = (n-1)d = function[water\ content(time, positon)] \qquad \text{Eq. 17}$$

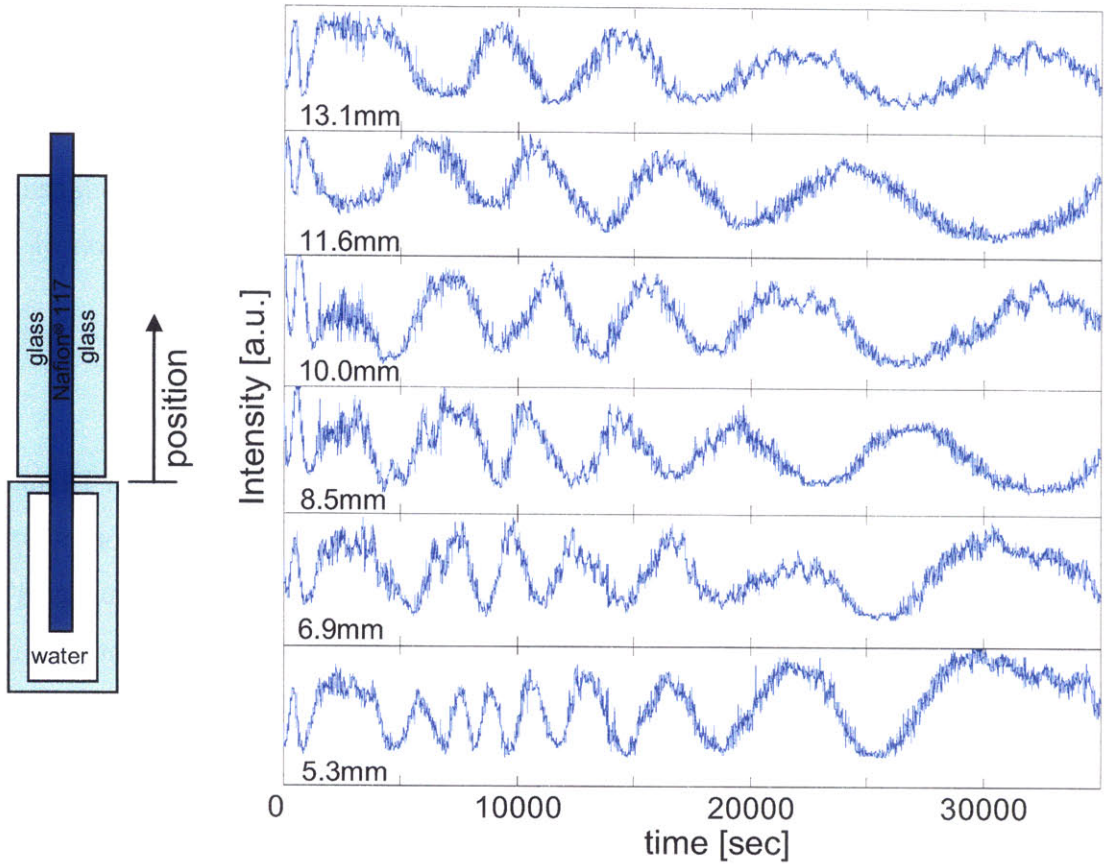

Figure 15. Interference intensity at selected positions during water uptake of Nafion® 117 membrane. As the distance from the water line increases, the frequency of intensity oscillation decreases.

Even though the details of the *function* in Eq. 17 will be discussed in the next chapter, it can be easily guessed that ΔOPL is directly related with the water content of Nafion® membranes and will increase with water uptake which will add more optical length to the probing beam path. Therefore, the first step to measure the water content by laser interferometry is to retrieve ΔOPL from the interference intensity. Subsequently, the *function* defining the relationship between ΔOPL and water content will be used to obtain the distribution of water content in Nafion® membranes as a function of time and position.

The retrieval of ΔOPL requires a series of signal processing, which is summarized in Figure 16. The noise in raw intensity signals is reduced by low-pass filtering. Then the denoised signal is normalized such that it oscillates between -1 and 1. Applying $\cos^{-1}$ function to the normalized signal generates wrapped phase signal. This wrapped phase can be unwrapped by subtracting or adding 2π at each discontinuity. Finally unwrapped phase is converted to ΔOPL by multiplying the wavelength of the He-Ne laser (632.8 nm) and dividing by 2π. One assumption made for the retrieval of optical path length is the direction of the change. Interferometry technique detects only the changes in optical path length without the capability of determining whether the change is negative or positive. In the case of this diffusion experiment where a Nafion® sample absorbed water over time, however, the direction of the change in optical path length can be safely assumed to be positive because water molecules diffusing into the membrane will increase the optical path length.

It is necessary to fully automate the process of ΔOPL retrieval because each experiment requires the repetition of the process more than 1000 times since the CMOS sensor has 1280×1024 pixels. One very challenging step to the automation of the process is the denoising step. The normalizing step detects local maxima and minima and linearly adjusts the values of a portion of data between a local maximum and a minimum so that they can vary exactly between 1 and -1. If the noise in intensity signal is not removed, all the peaks and valleys of the noise are recognized as maxima and minima and result in huge phase changes even when there is no phase change in reality. Therefore, it is indispensible to remove noise by low-pass filtering with a proper cutoff frequency which allows the real variation in intensity signal to survive and removes unwanted noise. The problem comes from the fact that the frequency of the intensity signal varies both

spatially and temporally, which makes it difficult to use a single cutoff frequency.

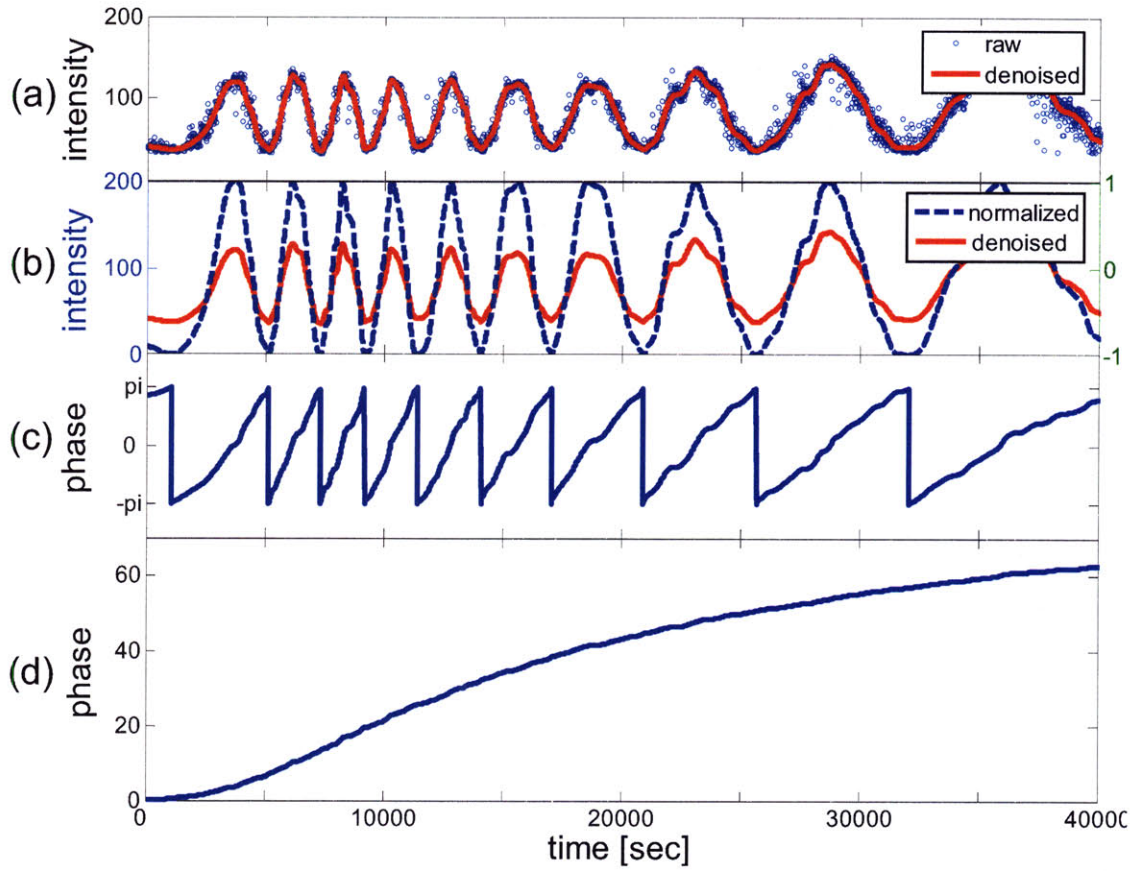

Figure 16. Procedure for retrieving phase information from interference intensity. (a) Noise reduction of raw signal by low-pass filtering. (b) Normalization of denoised signal to make signal oscillate between -1 and 1. (c) Retrieval of phase by applying $\cos^{-1}$ function. (d) Phase unwrapping by adding or subtracting 2π at every discontinuity.

The solution to solve this problem is to vary the cutoff frequency from high to low sequentially and get a denoised signal piece by piece. In other words, a set of data as a function of time is filtered with a starting cutoff frequency high enough to keep all the wanted oscillation. Then, the signal is monitored to find portions of which the difference between the neighboring maximum and minimum exceeds a certain percentage of the difference between the global maximum and minimum. These portions of the signal are stored separately and the rest of the signal is tested with a lower cutoff frequency to find more of surviving portions. This process is repeated until the collection of survived

portions covers the entire time span of the original signal. The Matlab® codes for carrying out this piecewise noise reduction are in Appendix A.

2.3 Results

A distribution of ΔOPL as a function of time and position, which is believed to be directly related to the changes in the water content of Nafion® absorbing water, can be obtained when the procedure for the optical signal processing is applied to the interference intensities recorded by every pixel of the CMOS sensor. Since the experimental setup was designed to have one dimensional diffusion process, it is not necessary to consider the variation of ΔOPL in the horizontal direction. Figure 17 shows a distribution of interference intensity and the corresponding variation of ΔOPL along a vertical line as a function of the distance from the water line and time. Although the features of diffusion is clearly seen in Figure 17 (b), conversion of ΔOPL to water content requires another step, calibration, which is dealt in Chapter 3.

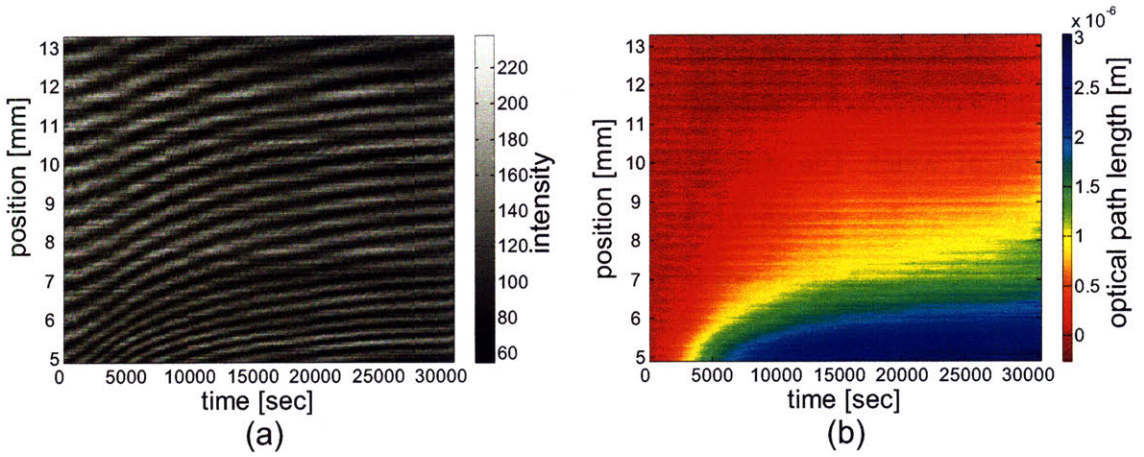

Figure 17. (a) Distribution of optical intensity along a vertical line as a function of the distance from the water line and time. (b) Corresponding distribution of the optical path length converted from (a) using the procedure for optical signal processing explained in Figure 16.

Chapter 3. Relationship between Water Content and Optical Path Length

In the previous chapter, it was shown that the variation in ΔOPL of a Nafion® membrane experiencing changes in the water content can be visualized using laser interferometry assuming that ΔOPL and the water content of Nafion® membranes are directly related. In this chapter, a mathematical model to estimate the relationship between the two quantities is formulated and confirmed by ellipsometry and calibration experiments.

3.1 Experimental

In order to correlate the difference in the optical path length of Nafion® to the changes in the water content, calibration experiments were performed. For this purpose, a wet Nafion® sample was prepared by immersing in DI water and then removing liquid water droplets on the surface of the sample. This sample was quickly assembled in a sample holder shown in Figure 18, which had a tensile spring for maintaining the Nafion® sample flat during interferometry experiments. A micro-balance (Mettler Toledo, AG285) monitored the decrease in the weight of the sample over time, which was the result of the evaporation of water. The weight change was converted to water content change by comparing with the dry weight of the Nafion® sample. At the same time, the same Mach-Zehnder interferometer as shown in Figure 13 recorded the decrease in the optical path length over time.

Nafion® thin films for ellipsometry experiments were made by spin-coating 9 % Nafion® dispersion (1100 g EW, Dupont) on silicon wafers and heat-treating in a vacuum furnace at 165 °C for 2 hours because ellipsometry requires a thin film, typically thinner than 1 μm, for the measurement of refractive index and thickness. It is noted that optical and swelling properties of spin-coated samples may differ from those of commercially available membranes such as Nafion® 117. However, there was no other method to separately measure the changes in the refractive index and the thickness of Nafion® caused by water uptake, which were required to verify the relationship between ΔOPL and the water content. Therefore, the properties of commercially available Nafion®

membranes were assumed to be similar to those measured from thin films. Refractive indexes and thicknesses of these thin films were measured by a spectroscopic ellipsometer (J. A. Woollam, M-2000D) under air and liquid water.

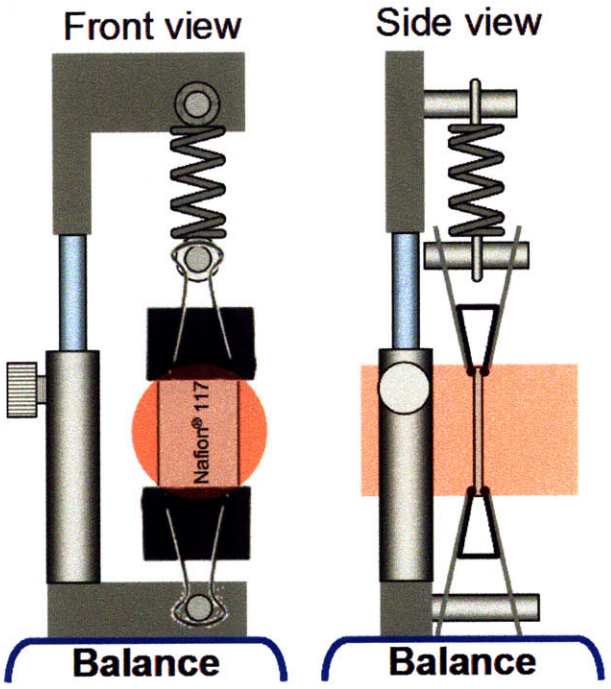

Figure 18. Nafion® sample holder for calibration experiments. A tensile spring stretches Nafion® 117 membrane to keep it flat. During dehydration of the membrane by evaporation, the Mach-Zehnder interferometer monitors the difference in the optical path length and a micro-balance monitors the variation in the weight, which can be converted to the changes in the water content. The red shade indicates the location of the probing laser beam.

3.2 Results of Calibration Experiment

Assuming that the evaporation of water from the surface of the Nafion® sample was spatially uniform, a variation in interference intensity recorded as a function of time from the center of the sample was representative of the whole area of the sample. This intensity signal was analyzed to obtain the phase variation by the same procedure explained in the previous chapter and the result is shown in Figure 19. In this case, the direction of the changes in phase was assumed to be negative because the loss of water

molecules during the dehydration process decreased the optical path length.

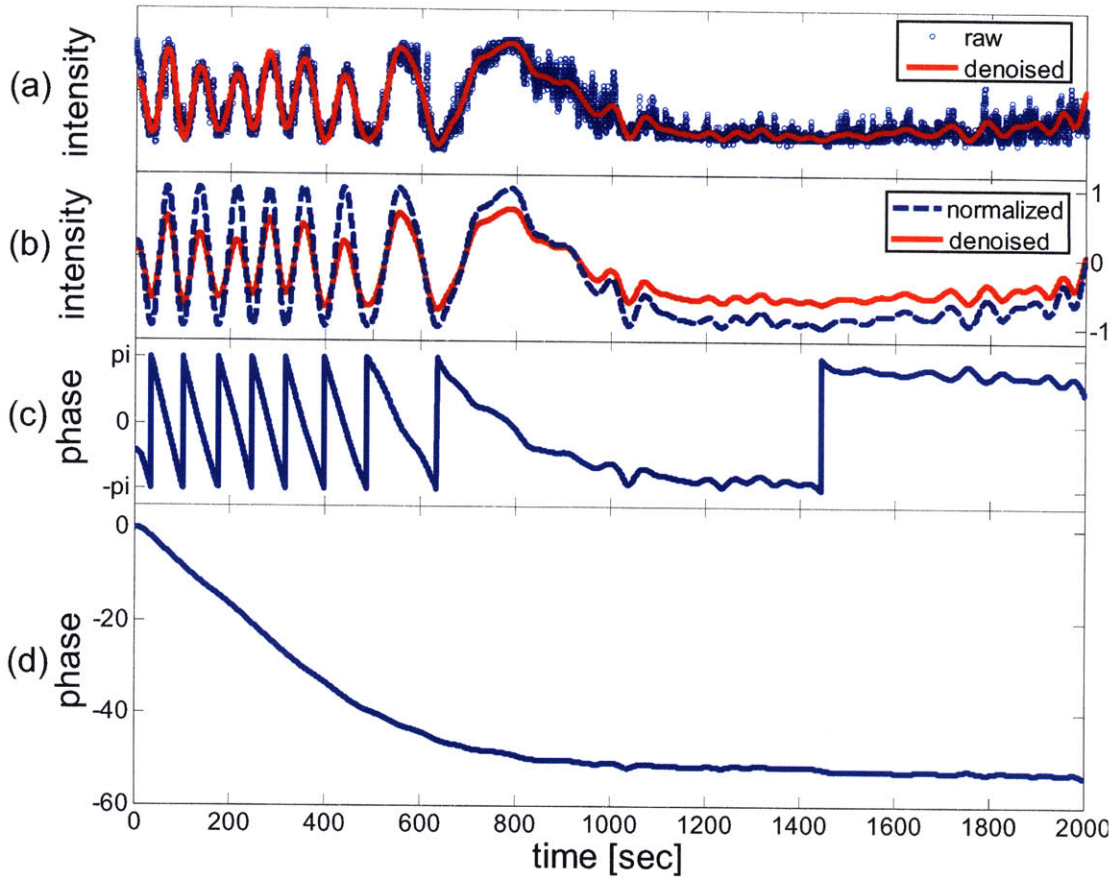

Figure 19. Procedure for retrieving phase information from interference intensity during the calibration experiment. (a) Noise reduction of raw signal by low-pass filtering. (b) Normalization of denoised signal to make signal oscillate between -1 and 1. (c) Retrieval of phase by applying $\cos^{-1}$ function. (d) Phase unwrapping by adding or subtracting 2π at every discontinuity.

Figure 20 shows the variation in normalized ΔOPL calculated from Figure 19 (d) knowing that d_0 is the initial thickness of Nafion® 117 membrane (178 μm), and water content measured by the micro-balance as a function of time while dehydrating the Nafion® sample. The water content started from ~10 and decreased to 1 within 2000 sec. Most of the loss in the water content occurred within 1000 sec. The observed trend in the variation of the normalized ΔOPL was very similar to that observed for the water content. Indeed, a linear relationship between the water content and the normalized ΔOPL (slope

= 0.003769) was found. However, the slope of 0.003769 can not always be used to convert the changes in ΔOPL to those in the water content because this linearity will change depending on whether Nafion® expands and shrinks isotropically or uni-directionally. The sample holder for the calibration experiment allowed virtually isotropic volume change, while that for diffusion experiment allowed only uni-directional volume change due to the friction between the glass plates and a Nafion® membrane.

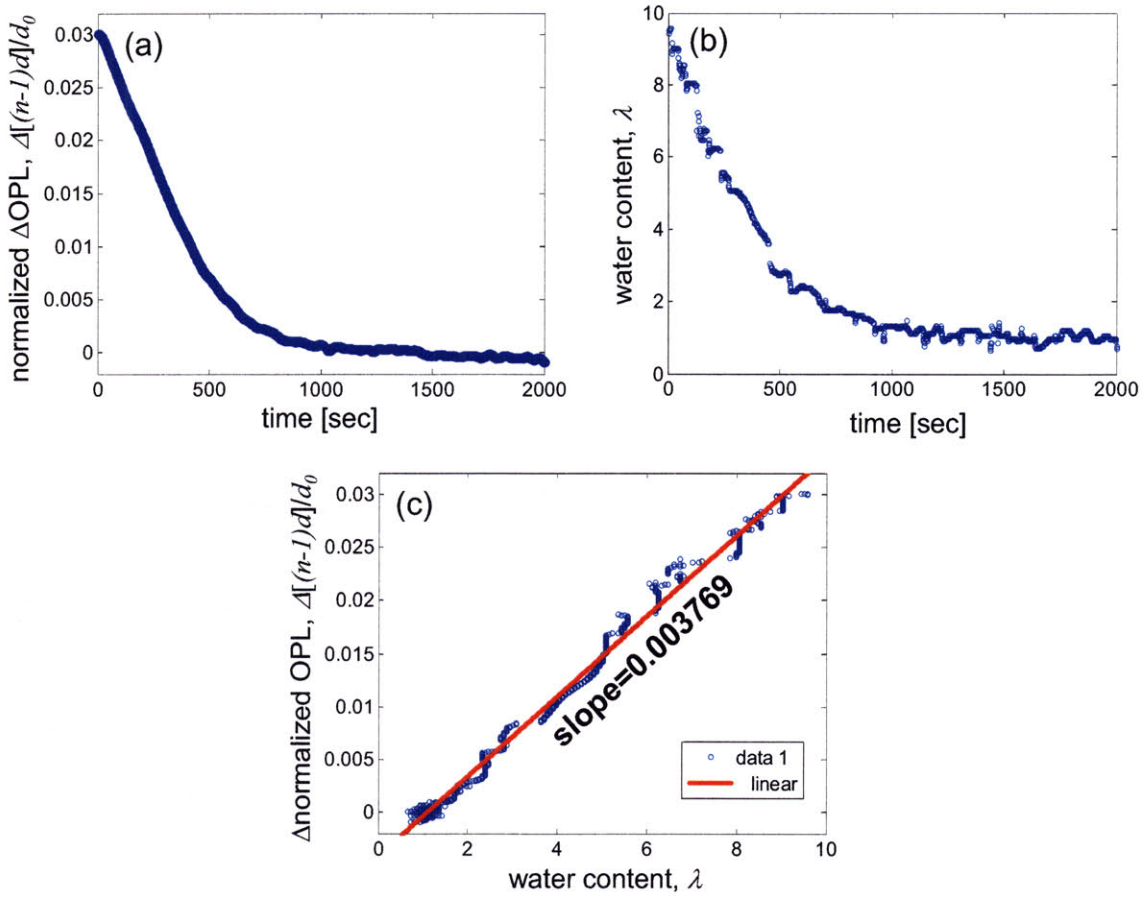

Figure 20. Results of calibration experiments. (a) Changes in optical path length during dehydration of Nafion® membrane, normalized by the initial thickness. (b) Changes in water content as a function of time. (c) Relationship between the optical path length and the water content.

3.3 Mathematical Modeling

Since there was no proper method to measure the changes in the optical path

length of Nafion® membranes constrained in two dimensions allowing evaporation of water from the surface of the membrane, a mathematical model was formulated to estimate the relationship between the water content and ΔOPL for the case of uni-directional swelling based on Lorentz-Lorenz rule, which is known to have less than 0.02 % error for estimating refractive indexes of liquid-liquid mixtures.[99] The refractive index of a mixture is estimated from the volume fraction of each constituent:[100]

$$\frac{n_{mixture}^2 - 1}{n_{mixture}^2 + 2} = \phi_{Nafion} \frac{n_{nafion}^2 - 1}{n_{nafion}^2 + 2} + \phi_{water} \frac{n_{water}^2 - 1}{n_{water}^2 + 2} \qquad \text{Eq. 18}$$

where ϕ is volume fraction and n is refractive index. By assuming incompressibility of Nafion® and water, volume fraction of Nafion® and water can be directly related to water mass ratio, m, which is defined as mass of water over mass of dry Nafion® and has the following relationship to water content, λ:

$$m = \frac{M_{water}}{EW_{Nafion}} \lambda = \frac{18}{1100} \lambda \qquad \text{Eq. 19}$$

In order to consider void volume in dry Nafion®, another parameter, f, needs to be introduced, which is defined as the fraction of water contributing to volume increase of Nafion®-water mixture. The relationship between volume fractions and the parameter, f, is illustrated in Figure 21. f can have a value between 0 and 1 and the summation of the volume fractions of Nafion® and water may not be unity because void volume of dry Nafion® can be shared by water.

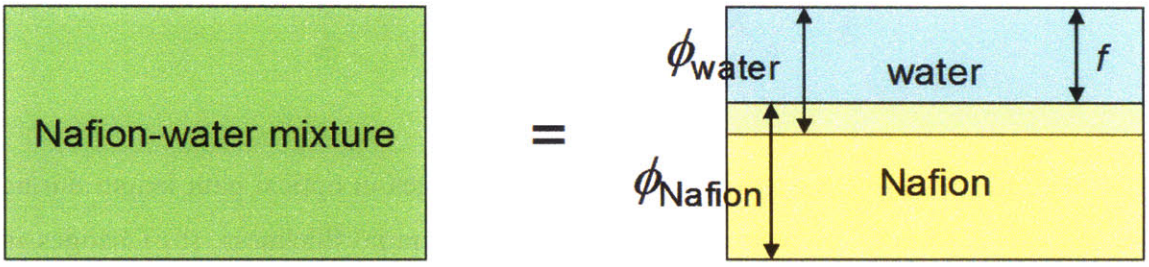

Figure 21. Relationship between volume fractions of Nafion®-water mixture and parameter, f.

Then, Eq. 18 is written as:

$$\frac{n_{mixture}^2-1}{n_{mixture}^2+2}=\frac{1}{1+fm\rho_{nafion}/\rho_{water}}\frac{n_{nafion}^2-1}{n_{nafion}^2+2}+\frac{m\rho_{nafion}/\rho_{water}}{1+fm\rho_{nafion}/\rho_{water}}\frac{n_{water}^2-1}{n_{water}^2+2}, \quad \text{Eq. 20}$$

where ρ is density. This can be rearranged to:

$$\frac{n_{mixture}^2-1}{n_{mixture}^2+2}=\left(k_{water}+\frac{k_{nafion}}{m}\right)\frac{m\rho_{nafion}}{1+fm\rho_{nafion}/\rho_{water}}, \quad \text{Eq. 21}$$

where k is molar refraction, R, divided by molecular weight, M, or:

$$k=\frac{R}{M}=\frac{n^2-1}{n^2+2}\frac{1}{\rho} \quad \text{Eq. 22}$$

In addition, the changes in the thickness of a Nafion® membrane can be related to m and f for two different swelling cases:

$$d=d_0\left(1+fm\rho_{nafion}/\rho_{water}\right), \text{ uni-directional swelling} \quad \text{Eq. 23}$$

$$d=d_0\left(1+\frac{1-\nu}{1+\nu}fm\rho_{nafion}/\rho_{water}\right), \text{ isotropic swelling} \quad \text{Eq. 24}$$

where d is swelled thickness and d_0 is dry thickness. ν is Poisson's ratio and when ν is 0.5 or the total volume of Nafion®-water mixture is conserved, the thickness change of isotropic swelling case is three times smaller than that of uni-directional swelling case for same amount of water uptake. Solasi[101,102] experimentally measured the Poisson's ratio of Nafion® membranes, which was found to be 0.4, and this will result in a reduced difference of thickness changes between the two swelling cases. If refractive index and thickness are measured both when the Nafion® membrane is wet and when it is dry, one can calculate m and f using Eq. 21 and either Eq. 23 or Eq. 24. Once f for Nafion® is determined, the relationship between the water content and the optical path length can be estimated from the equations.

3.4 Results of Ellipsometry and Discussion

Ellipsometry uses a linearly polarized light to examine a sample. The reflected light from the sample is polarized depending on the optical properties of the sample and the ratio of p-polarized (r_p) to s-polarized (r_s) light can be expressed as:

$$ratio=\frac{r_p}{r_s}=\tan\Psi\cdot e^{i\Delta}, \quad \text{Eq. 25}$$

where $\tan\Psi$ and $e^{i\Delta}$ represent the amplitude ratio and the phase difference between the two polarized lights. A spectroscopic ellipsometer measures Ψ and Δ as a function of the wavelength of the incident light and the optical properties of the sample is obtained by curve-fitting between the measured data and the calculated data from a layer model. The layer model used for the measurement of the thickness and the refractive index of Nafion® thin films is illustrated in Figure 22.

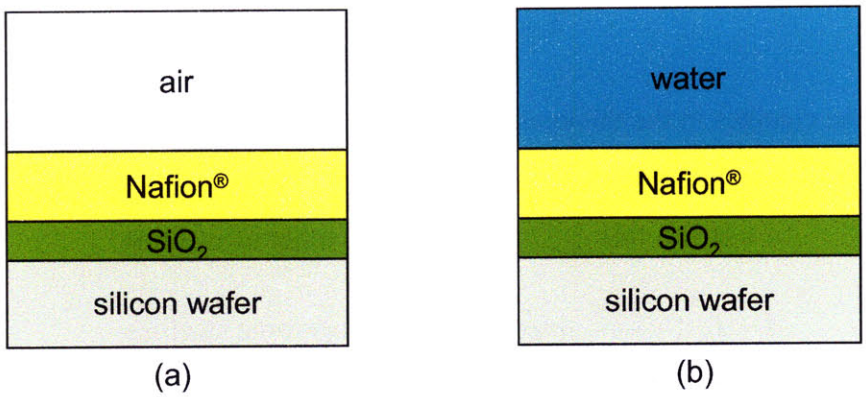

Figure 22. Layer models used for ellipsometry. Nafion® thin films are exposed to (a) air and (b) liquid water.

The dependency of the refractive index of Nafion® on wavelength was assumed to obey the Cauchy model:[103]

$$n(wavelength) = A + \frac{B}{wavelength^2} + \frac{C}{wavelength^4}, \qquad \text{Eq. 26}$$

where A, B, and C are coefficients to be determined by curve-fitting to the measured data of ellipsometry.

The results of curve-fitting between the measured amplitude ratio, Ψ, and the calculated values from the layer model are shown in Figure 23. The data for wet Nafion® thin films were taken after at least 30 minutes from the immersion of the samples in liquid water in order to allow them to equilibrate. Data taken after 1 hour did not show significant difference from those taken at 30 minutes, which confirmed that the samples reached the equilibrium within 30 minutes. In all cases including the ambient condition of air or water and thicknesses of thin films prepared at two different spin speeds, the layer model fitted the experimental data very well especially in the region near the wavelength

of 633 nm, which is the wavelength of the light source in the interferometry setup used for this study.

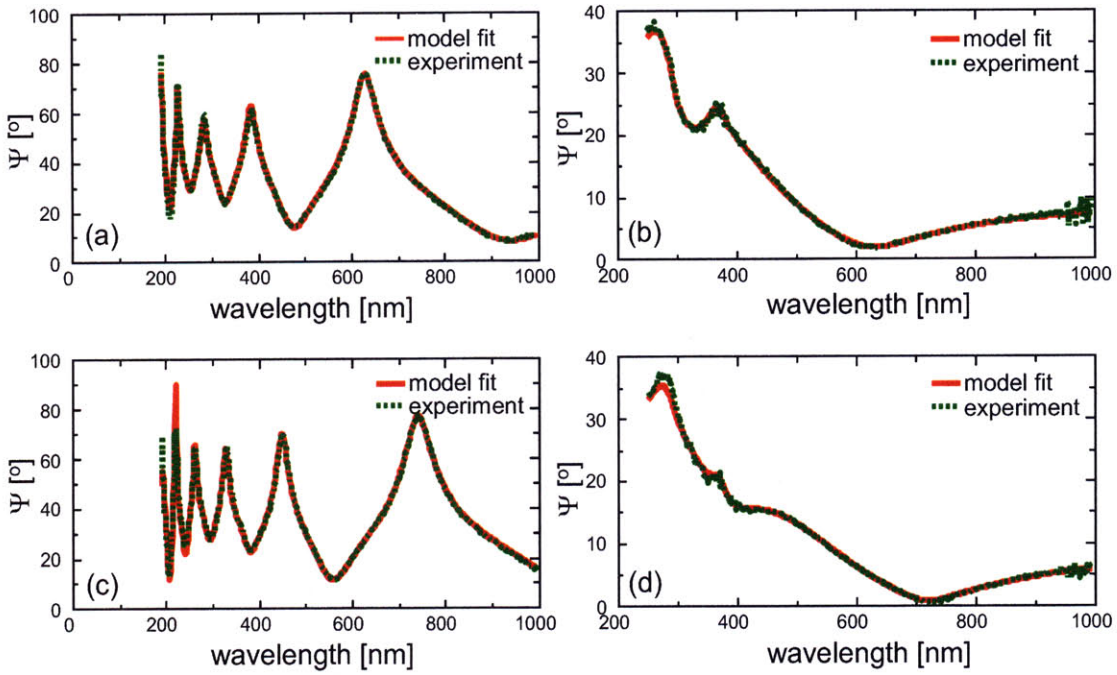

Figure 23. Results of curve-fitting the measured (dotted green) amplitude ratio of polarized lights to the calculated (solid red) values from the layer model of Nafion® thin films (a) spin-coated at 5000 rpm under air, (b) spin-coated at 5000 rpm under water, (c) spin-coated at 3000 rpm under air, and (d) spin-coated at 3000 rpm under water.

Table 2 summarizes the thickness and the refractive index of Nafion® thin films spin-coated at 5000 rpm and 3000 rpm under air or water. The refractive indexes were taken at the wavelength of 632.7 nm. In both cases, the thickness of the films increased by ~20% and the refractive index decreased by ~0.2 % when immersed in water. The increase in thickness is the result of swelling due to water uptake and the decrease in refractive index is the result of mixing water molecules that are optically less dense material and have smaller refractive index than Nafion®. If Nafion® had a significant fraction of void volume in its dry state, one would observe an increase in refractive index when Nafion® takes water because filling void volume with water molecules would result in an optically denser material. Therefore, the observation of the decrease in the refractive index and the increase in the thickness indicates that the void volume of Nafion® is

minimal and almost all the water molecules taken by Nafion® increases the total volume of the mixture. This can be shown more clearly if the parameter, f, in Eq. 21 is evaluated.

Table 2. Thickness and refractive index of Nafion® thin films prepared at the spin speed of 5000 rpm and 3000 rpm.

Sample	Thickness [nm]		Refractive index @ 632.7 nm	
	under air	under water	under air	under water
5000 rpm	476.31	577.44 (+21.2%)	1.3613	1.3583 (-0.22%)
3000 rpm	562.45	668.90 (+18.9%)	1.3617	1.3596 (-0.15%)

All the quantities in Eq. 21 except m and f were measured by ellipsometry or known. In order to evaluate m and f, Eq. 23 or Eq. 24 can be used, which requires a determination of whether the Nafion® thin films on the silicon wafer swelled isotropically or uni-directionally. For this purpose, scanning electron microscopy (SEM) was used. The same Nafion® thin film used for the ellipsometry was exposed to dry and humid environment under an SEM (FEI/Philips XL30 FEG ESEM) and 3 surface features were checked to see if there was lateral expansion.

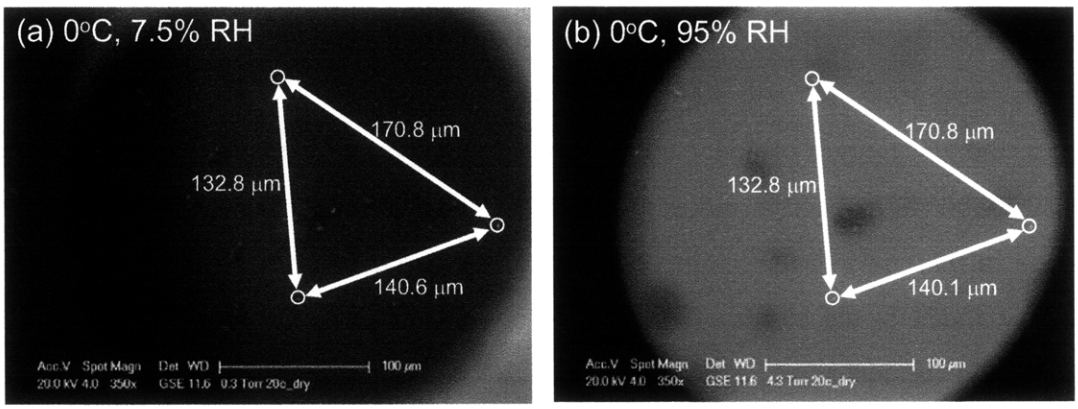

Figure 24. SEM images of Nafion® thin film spin-coated on silicon wafer under (a) 0°C, 7.5% RH and (b) 0°C, 95% RH. Distances among 3 surface features remained the same before and after hydration, which confirms no lateral expansion due to water uptake.

As shown in Figure 24, no significant lateral expansion was observed during the hydration of the sample, because of strong bonding between the Nafion® film and the silicon wafer. In addition, the fact that Nafion® thin film under water was not detached from the silicon wafer confirms uni-directional swelling. Therefore, the water content, m *or* λ, and f of Nafion® thin films were calculated using Eq. 21 and Eq. 23. The results are shown in Table 3.

Table 3. Water content and the fraction of water contributing to volume increase, f, measured from Nafion® thin films prepared at the spin speed of 5000 rpm and 3000 rpm, when immersed in liquid water.

Sample	Water content, λ (m)	f
5000 rpm	6.8 (0.1105)	0.9702
3000 rpm	6.1 (0.1002)	0.9541

It was found that f was 0.95~0.97 and water content of Nafion® thin films soaked in liquid water was 6~7. The fact that f of Nafion® thin films is close to 1 suggests that the void volume of dry Nafion® is close to 0 and the assumption of volume additivity and incompressibility for Nafion® and water mixture is valid with less than 5 % error. Maximum water content of Nafion® soaked in water is known to be ~22 which is roughly 3 times bigger than the values obtained from the ellipsometry experiments. The discrepancy comes from the difference in constraints imposed on Nafion® membranes. In other words, water content of 22 is obtained for a membrane allowed to swell three-dimensionally while water content of 6~7 can be taken by a membrane constrained in the lateral directions and allowed to swell only in the thickness direction. To generalize, water content of 6~7 can be absorbed per dimension in which Nafion® is allowed to swell. This indicates that a Nafion® membrane which is physically constrained between current collectors of a fuel cell may not reach water content of 22 even when it is exposed to liquid water.

Figure 25 shows the linear relationship between the water content and the normalized ΔOPL of Nafion® for uni-directional and isotropic swelling cases calculated by Eq. 21 ~ Eq. 24 with $f = 0.96$ found from the ellipsometry experiments. The slope in

the case of uni-directional swelling is 0.01086. In the case of isotropic swelling, the slope is calculated to be 0.00451 and 0.00345 with the assumption of ν = 0.4 and 0.5, respectively. These values are roughly 3 times smaller than that of uni-directional swelling case and close to 0.003769, which was obtained from the calibration experiments where the Nafion® sample was allowed to swell and shrink isotropically. The fact that the experimentally obtained slope lies between the estimations calculated from ν = 0.4 and 0.5 suggests that the Poisson's ratio of Nafion® membranes has a value between 0.4 and 0.5, and the model, described by Eq. 21 ~ Eq. 24, well predicts the changes in ΔOPL due to the water content changes.

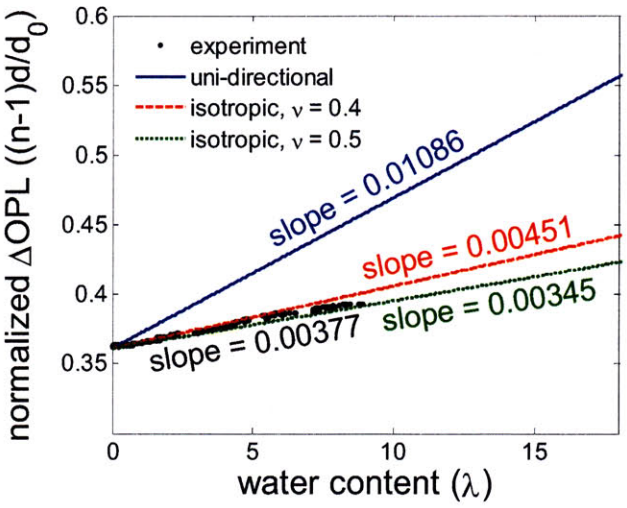

Figure 25. Relationship between the water content and the normalized optical path length of Nafion®.

To summarize, a linear relationship between the water content and the normalized ΔOPL was found both experimentally and mathematically. The proportionality can vary from 0.01086 to 0.00345 depending on the number of constraints on Nafion® membranes and the Poisson's ratio. The variation is caused by the fact that interferometry or ellipsometry can detect changes only in thickness direction. When water uptake causes changes also in the lateral direction, which is not observable by optical techniques, a proper adjustment is necessary in order to relate the changes in the optical path length to those in the total water content. However, in the case of the diffusion

experiments, where a Nafion® membrane was sandwiched by glass plates and the friction between the two prevented any swelling in lateral direction, the proportionality of uni-directional swelling should be used, which is:

$$\frac{1}{d_0}\frac{\partial \Delta OPL}{\partial \lambda} \approx \frac{1}{d_0}\frac{d[(n-1)d]}{d\lambda} = 0.01086 \qquad \text{Eq. 27}$$

Then, the relationship between the phase directly measured from the laser interferometry and the water content (λ) of Nafion® membrane is:

$$\lambda(x,t) = phase(x,t)\frac{wavelength}{2\pi \cdot d_0}\frac{1}{0.01086} + \lambda_0, \qquad \text{Eq. 28}$$

where the *wavelength* of He-Ne laser is 632.8nm and d_0 is the initial thickness of Nafion® membrane. λ_0 is the initial condition of the water content or $\lambda(x,\ t = 0) = \lambda_0$ with the initial phase distribution set to be 0 or $phase(x,\ t = 0) = 0$. Figure 17 (b) can be redrawn using Eq. 28 and $\lambda_0 = 1$ which was determined by comparing the weight of a Nafion® sample measured after taking it out of the drying oven and before assembling it into the sample holder. The only difference between Figure 17 (b) and Figure 26 is the scale bar of which the conversion is done using Eq. 28.

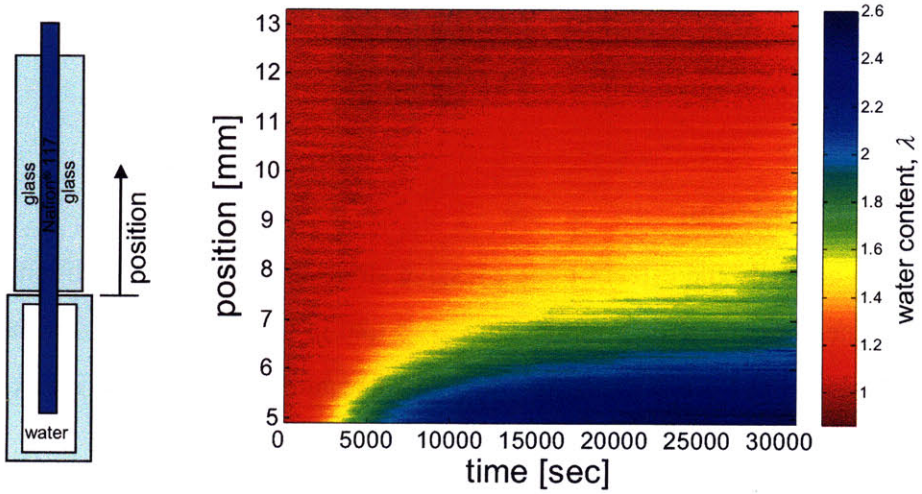

Figure 26. Distribution of the water content of a Nafion® 117 membrane absorbing water as a function of time and the distance from the water line.

Chapter 4. The Effect of Compressive Stress on the Optical Path Length of Nafion®

The sample holder for the visualization of water diffusion into Nafion® membranes inevitably had a clamping mechanism for two purposes: 1) to keep a sample membrane flat during the diffusion process and 2) to prevent water from evaporating from the surface of the sample. Without the clamping mechanism, a sample membrane develops wrinkles ruining the optical signal and the diffusion process is not one dimensional, which can make the analysis of diffusion more complicated or result in no detectable changes in water content due to a fast evaporation before reaching the upper region of the sample. One side effect of this clamping mechanism such as sandwiching between two glass plates is the compressive stress exerted on the sample membrane. This is not always disadvantageous because one can examine the effect of compressive stress on diffusion process, which will be discussed in Chapter 6. However, the effect of compressive stress on the optical path length of Nafion® membranes should be checked prior to that in order for the water content data measured from the laser interferometry to be meaningful. It is evident that higher compressive stress hinders the swell due to water uptake and suppresses the diffusion process, but it is not clear how much the optical path length of a Nafion® membrane with a fixed value of water content will change under compressive stress.

4.1 Mathematical Modeling

In order to evaluate the effect of compressive stress on the optical path length of a Nafion® membrane, a mathematical model similar to that in Chapter 3.3 was formulated. According to the Lorentz-Lorenz equation, the density and the refractive index of a material satisfy the following relationship:

$$\frac{1}{\rho}\frac{n^2-1}{n^2+2}=const, \qquad \text{Eq. 29}$$

where ρ and n are density and refractive index, respectively. When the properties of Nafion® (ρ = 1980 kg/m^3, n = 1.3615) are plugged into Eq. 29, the const is 1.12×10^{-4} m^3/kg. The density of Nafion® will change as a function of compressive stress:

$$\rho_{stressed} = \frac{\rho_0}{1-\sigma/K}, \qquad \text{Eq. 30}$$

where $\rho_{stressed}$, ρ_0, σ, and K are density under stress, initial density, compressive stress, and bulk modulus, respectively. The bulk modulus of Nafion® is not well known, but expected to be much larger than the Young's modulus as the Poisson's ratio approaches to 0.5. In order to estimate the upper limit of the effect of compressive stress on the optical path length, the bulk modulus of Nafion® can be assumed to have a similar value to the Young's modulus, which is 250 MPa in its dry state. Then, the variation of the refractive index of Nafion® can be evaluated from Eq. 29 and Eq. 30. In addition, the volume change of a Nafion® membrane, ΔV, under isotropic pressure, P, can be written as:

$$\frac{\Delta V}{V} = \frac{A(d_{stressed} - d_0)}{Ad_{stressed}} = -\frac{P}{K}, \qquad \text{Eq. 31}$$

where A, $d_{stressed}$, and d_0 are the area, the thickness under pressure and the initial thickness, respectively. P can be related to the compressive stress in the thickness direction, σ, by:

$$P = \frac{1}{3}\frac{1+\nu}{1-\nu}\sigma, \qquad \text{Eq. 32}$$

where strains in other directions than the thickness direction are assumed to be zero due to the friction between Nafion® and the compressing device. Then, Eq. 31 is rearranged to:

$$d_{stressed} = d_0 \frac{1}{1+\frac{1}{3}\frac{1+\nu}{1-\nu}\sigma/K} \approx d_0\left(1-\frac{1}{3}\frac{1+\nu}{1-\nu}\sigma/K\right), \qquad \text{Eq. 33}$$

The optical path length of a Nafion® membrane normalized by the initial thickness as a function of compressive stress can be evaluated using Eq. 29 ~ Eq. 33 with the assumption of $\nu = 0.4$ or 0.5 as plotted in Figure 27. A linear relationship between the normalized ΔOPL and compressive stress is found to be 4.887×10^{-4} MPa^{-1} and 1.659×10^{-4} MPa^{-1} for the case of $\nu = 0.4$ and 0.5, respectively. In the case of Nafion®-water mixture, the additional contribution of water to change the dependency of ΔOPL on compressive stress is insignificant because the bulk modulus of water is 2.2 GPa, which is much higher than that assumed for Nafion®.

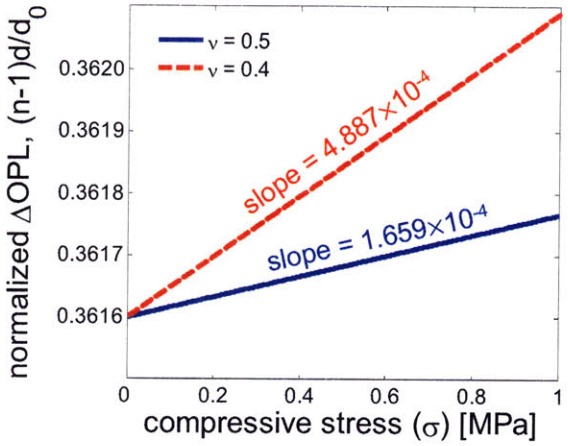

Figure 27. Relationship between compressive stress and the normalized optical path length of Nafion®.

4.2 Experimental

Even though the dependency of ΔOPL on compressive stress seems to be much smaller than that on water content, which is 0.01086 λ^{-1}, the comparison is valid only when it is known how much the variation in compressive stress develops in the sample holder for diffusion experiments. Therefore, another laser interferometry experiment was necessary to examine the relationship between the normalized ΔOPL and the compressive stress induced by the sample holder.

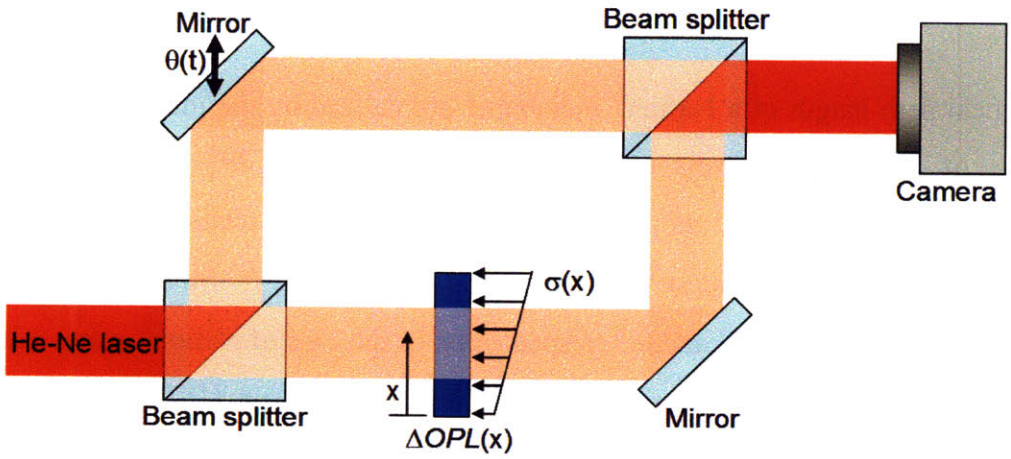

Figure 28. Mach-Zehnder interferometer with phase shifting capability for measuring the spatial distribution of ΔOPL induced by the spatial gradient in compressive stress.

A Nafion® 117 membrane with a spatially uniform water content was prepared by storing it in the ambient air and assembled into the sample holder shown in Figure 14 without the water chamber so that the water content of the sample did not change over time. The force exerted by the two compressive springs was adjusted to generate a spatial gradient in compressive stress intentionally. The Mach-Zehnder interferometer shown in Figure 13 was slightly modified to have the capability of phase shifting in the reference beam path as illustrated in Figure 28. Phase shifting was accomplished by translating the mirror in the reference beam path back and forth at a certain speed. The variation in the pattern of interference intensity can be analyzed to get the spatial distribution of ΔOPL of the sample under non-uniform compressive stress.

4.3 Laser Interferometry with Phase Shifting

The interference intensity detected by the experimental setup in Figure 28 can be described by:

$$intensity \Leftrightarrow \cos\left(\theta(t)+\frac{\Delta OPL(x)}{wavelength}2\pi\right), \qquad \text{Eq. 34}$$

where $\theta(t)$ is the phase shift controlled by translating the mirror in the reference beam path and $\Delta OPL(x)$ is the spatial distribution of the optical path length induced by the gradient in compressive stress. If a series of intensities (I_n) measured at 5 θ's with every $\pi/2$ interval, it is possible to retrieve $\Delta OPL(x)$ by the following equation:[104]

$$\frac{\Delta OPL(x)}{wavelength}2\pi = \tan^{-1}\left[\frac{2(I_2(x)-I_4(x))}{2I_3(x)-I_1(x)-I_5(x)}\right] \qquad \text{Eq. 35}$$

I_5 is used to reduce the effect of error or noise even though I_1 and I_5 should be the same since they are taken with 2π interval. In order to determine the relationship between t and θ, a time sequence of interference intensity was examined as shown in Figure 29. The agreement between the measured intensity and a cosine function was good and the period of the oscillation was determined to be ~2.7 sec. Correspondingly, a series of intensity images taken with 0.675 sec interval can be used to retrieve the spatial distribution of phase or $2\pi\Delta OPL/wavelength$. An example is shown in Figure 30. The phase information obtained by this procedure is wrapped with an interval of π due to the limitation of $\tan^{-1}$

function, which can be spatially unwrapped to get a smooth distribution by adding or subtracting π at the locations of discontinuity.

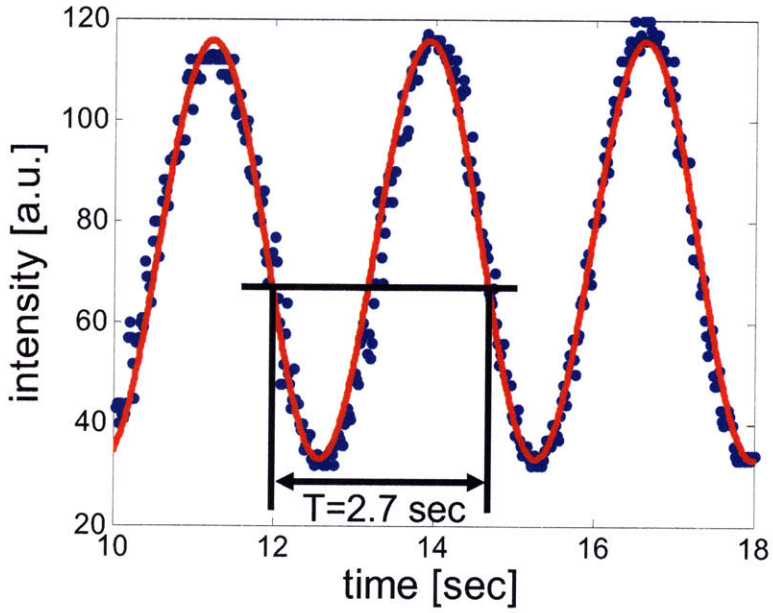

Figure 29. Variation of interference intensity at a fixed position as a function of time during the laser interferometry with phase shifting. The measured intensity (dot) is fitted to a cosine function (solid line).

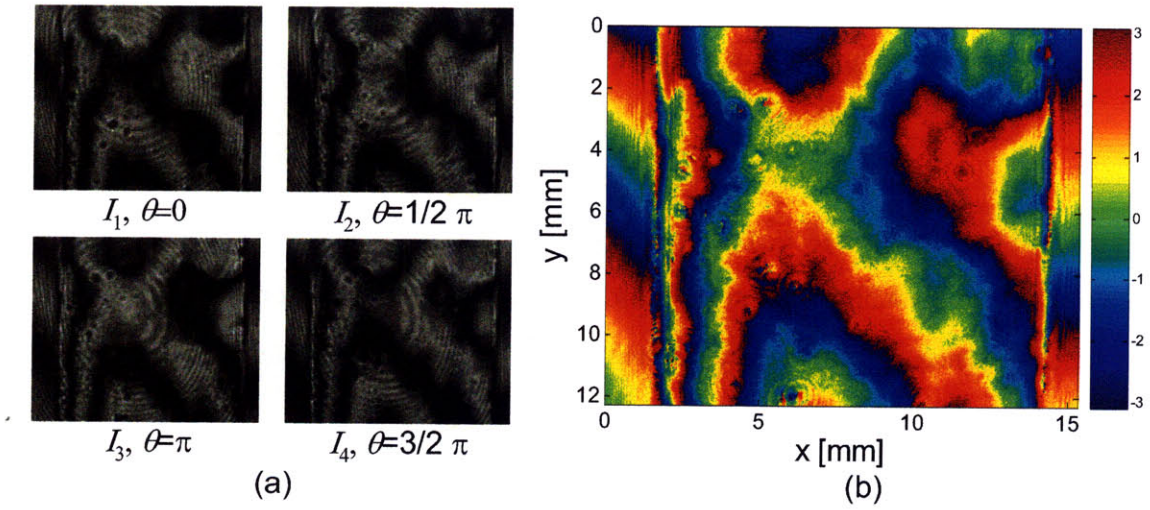

Figure 30. (a) Series of intensity images taken at the phase shifts with π/2 interval. (b) Reconstructed phase of a Nafion® 117 membrane assembled in the sample holder.

4.4 Results and Discussion

The $\Delta OPL(x)$ obtained from the laser interferometry with phase shifting is not a measurement of the absolute optical path length of a Nafion® membrane sample. In fact, only the difference between the optical path lengths or $\Delta OPL(x_1)$- $\Delta OPL(x_2)$ is meaningful. Therefore, a proper evaluation of the effect of compressive stress on $\Delta OPL(x)$ requires a comparison between $\Delta OPL(x)$'s under different conditions of compressive stress distribution. For this purpose, 3 different cases of compressive stress distribution were examined as shown in Figure 31, which shows the spatial distribution of unwrapped phase of a Nafion® membrane. These phase distributions can be converted to $\Delta OPL(x)$ by multiplying the wavelength of the laser and dividing with 2π.

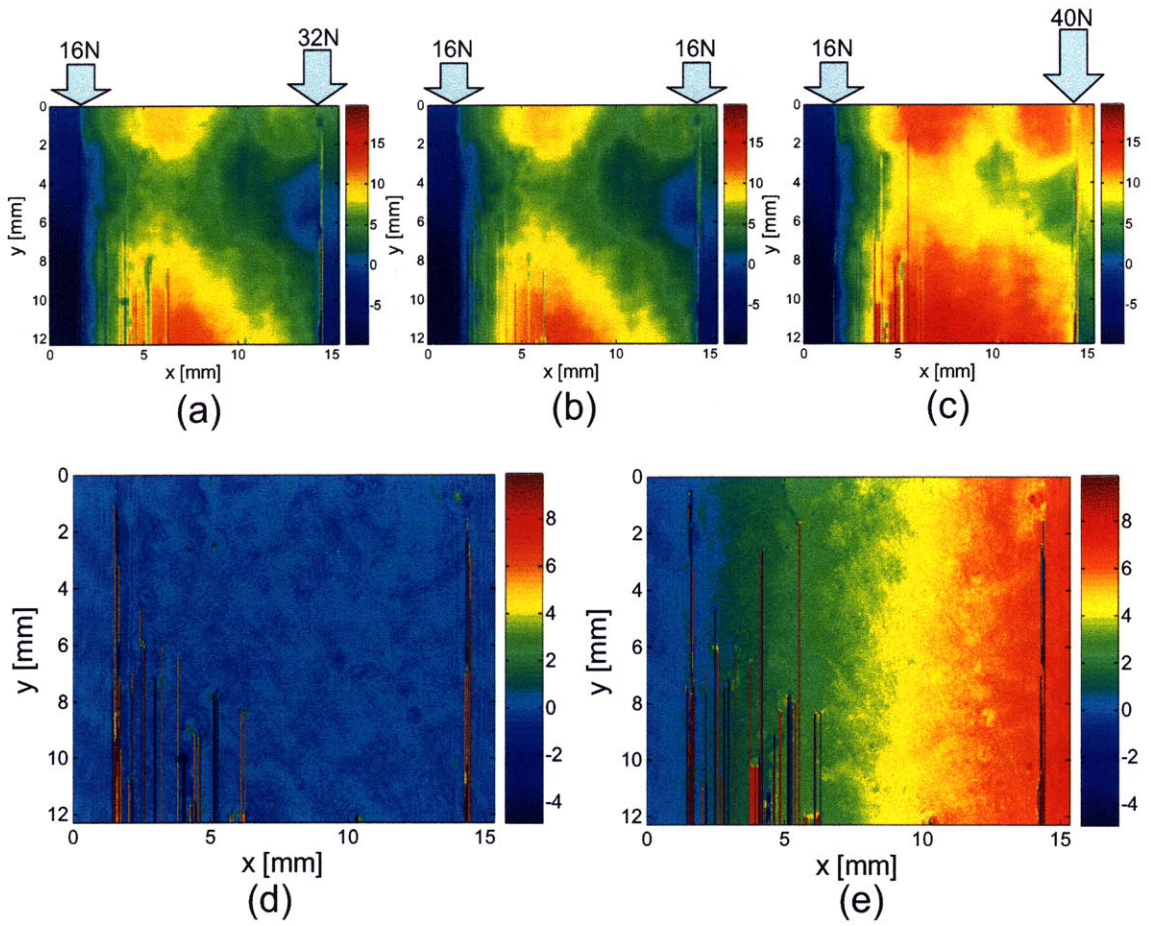

Figure 31. Spatial distributions of unwrapped phase of a Nafion® membrane due to the compressive stress with (a) moderate gradient, (b) no gradient, and (c) severe gradient. (d) Subtraction of (b) from (a). (e) Subtraction of (b) from (c).

The images (b) taken with no spatial gradient in compressive stress serves as a reference, which is subtracted from the image (a) or (c). The image (a) and (c) were taken with a moderate and a severe gradient in compressive stress which was controlled by adjusting the two springs of the sample holder differently. The image (d) and (e) show the true effects of the gradient in compressive stress and it is clear that the effect of a moderate gradient (12 MPa/m) is much smaller that that of a severe gradient (18 MPa/m). This trend is more evident when a line scan of the $\Delta OPL(x)$'s along a horizontal line (y = 1.2 mm) of the images in Figure 31 is compared to each other.

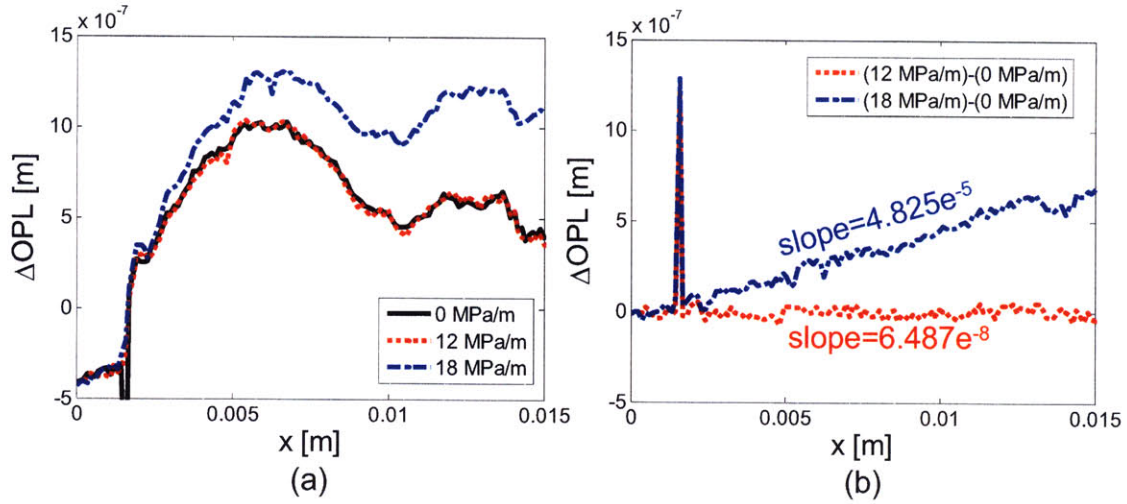

Figure 32. Line scans of the images of Figure 31 in the unit of ΔOPL. (a) Raw data. (b) Comparison to the reference case.

From Figure 32 (b), the dependency of the slope of $\Delta OPL(x)$ is found to be 6.487×10^{-8} m/m and 4.825×10^{-5} m/m for the two cases of different gradient in compressive stress. The dependency of $\Delta OPL(x)$ on the compressive stress can be determined by:

$$\frac{1}{d_0}\frac{d\Delta OPL}{d\sigma}=\frac{1}{d_0}\frac{d\Delta OPL}{dx}\frac{dx}{d\sigma} \qquad \text{Eq. 36}$$

using the measured quantities. The dependency is calculated to be 3.09×10^{-5} MPa^{-1} and 1.53×10^{-2} MPa^{-1} for the cases of the moderate and the severe gradient in compressive stress, respectively. The difference between the two values is bigger than expected considering the gradients of the two cases differ by only the factor of 1.5. This indicates

that the case of 18 MPa/m might cause a tilt of the sample holder and exaggerate ΔOPL.

In order to examine the effect of compressive stress when measuring the water content of Nafion® membranes from ΔOPL, it is necessary to compare typical variations in ΔOPL caused by the changes in the water content and the compressive stress developing during the diffusion experiments. The variation in the compressive stress is estimated to be 0.25 MPa at maximum when the size and the geometry of the sample holder are considered. This corresponds to ΔOPL of 0.68 μm for a Nafion® 117 membrane, which has the thickness of 178 μm, when the conversion rate of 1.53×10^{-2} MPa^{-1} is used. On the other hand, ΔOPL observed in most cases of the diffusion experiments is ~10 μm. Therefore, the error caused by directly converting ΔOPL to water content without considering the effect of compressive stress is less than 7 %. Furthermore, it is noted that the quantities used to calculate the ΔOPL of 0.68 μm due to compressive stress were chosen from the worst case, where 1) the greatest gradient of compressive stress developable in the sample holder and 2) the largest dependency between the ΔOPL and stress among the calculated and measured values were assumed.

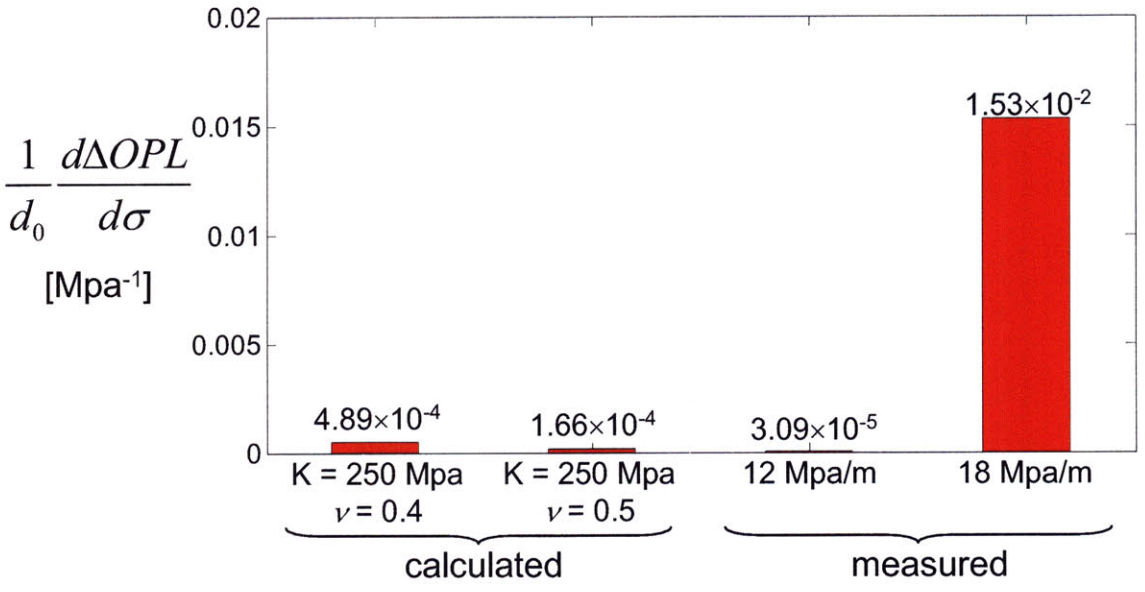

Figure 33. Comparison of the dependency of ΔOPL on compressive stress.

Figure 33 compares the dependencies of ΔOPL on compressive stress, which was

calculated or measured experimentally. It would be more natural to believe that the value of 1.53×10^{-2} MPa^{-1} used to calculate the ΔOPL of 0.68 μm is not realistic. The use of the other values for the error analysis will decrease the estimated error by the factor of $10^{2\sim3}$ leading to the error less than 0.2 %, which is totally negligible. Therefore, it is concluded that the effect of compressive stress induced by the clamping mechanism of the sample holder is not significant and the direct conversion of ΔOPL to the water content of Nafion® membranes is valid.

Chapter 5. Mathematical Procedure for Evaluating the Coefficients of Diffusion and Electro-osmotic Drag

In the previous chapters, a new method was introduced to visualize and quantify the changes of the water content in Nafion® membranes using laser interferometry with spatial and temporal resolutions of 12 μm and 500 Hz, respectively. The use of this technique combined with a governing equation enables the evaluation of two important transport properties, the coefficients of diffusion and electro-osmotic drag, which dictate the water balance within Nafion® membranes during the fuel cell operation. This chapter explains mathematical procedures to evaluate those properties, which can vary with the water content, by using the data of water content as a function of time and position. In addition, the validity of the mathematical procedure is examined by numerical simulations.

5.1 Formulation of the Governing Equation

The governing equation for one dimensional diffusion and electro-osmosis is derived from an infinitesimally thin slice of a Nafion® membrane illustrated in Figure 34.

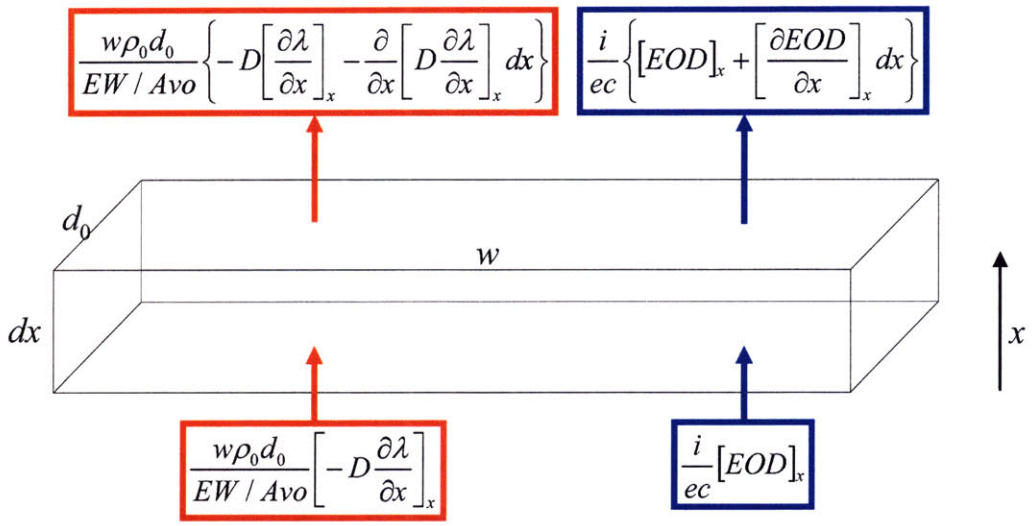

Figure 34. Water flux due to diffusion (in red) and electro-osmosis (in blue) in and out of an infinitesimally thin control volume in the unit of the number of water molecules per time.

The consideration for the mass balance of the control volume leads to:

$$\frac{\partial \lambda}{\partial t} = \frac{\partial}{\partial x}\left(D\frac{\partial \lambda}{\partial x}\right) - \frac{i}{d_0 \cdot w \cdot ec}\frac{EW}{Avo \cdot \rho_0}\frac{\partial EOD}{\partial x}, \qquad \text{Eq. 37}$$

where the symbols used are explained in Table 4.

Table 4. Symbols used in the governing equation.

Symbol	Value	Dimension	Comment
λ		dimensionless	water content, # of water molecules per SO_3^-
t		sec	time
x		m	position
D		m^2/sec	chemical diffusion coefficient
i		Amp	proton current
d_0		m	initial thickness of Nafion® membrane
w		m	width of Nafion® membrane
ec	1.602×10^{-19}	C	elementary charge
EW	1100	g/mol	equivalent weight of Nafion®
Avo	6.022×10^{23}	mol^{-1}	Avogadro's number
ρ_0	1.98	g/cm^3	initial density of Nafion®
EOD		dimensionless	electro-osmotic drag coefficient

Since D and EOD can vary as a function of the water content, Eq. 37 can be expanded as:

$$\frac{\partial \lambda}{\partial t} = \frac{\partial D}{\partial \lambda}\left(\frac{\partial \lambda}{\partial x}\right)^2 + D\frac{\partial^2 \lambda}{\partial x^2} - \frac{i}{d_0 \cdot w \cdot ec}\frac{EW}{Avo \cdot \rho_0}\frac{\partial EOD}{\partial \lambda}\frac{\partial \lambda}{\partial x} \qquad \text{Eq. 38}$$

5.2 Determination of Chemical Diffusion Coefficients

The results of the laser interferometry combined with the linear relationship between the water content and the optical path length of Nafion® membranes provide distributions of the water content as a function of time and position. Consequently, all the spatial and temporal derivatives in Eq. 38 can be evaluated by partially differentiating the measured data. In the case of experiments with diffusion only, the electro-osmotic term of

Eq. 38 vanishes because proton current is zero and an equation for pure diffusion with concentration-dependent chemical diffusion coefficients is:

$$\frac{\partial \lambda}{\partial t} = \frac{\partial D}{\partial \lambda}\left(\frac{\partial \lambda}{\partial x}\right)^2 + D\frac{\partial^2 \lambda}{\partial x^2} \qquad \text{Eq. 39}$$

Then, there are two unknown quantities left, D and $\partial D/\partial \lambda$, which should remain the same if calculated along an equi-λ line. Therefore, a dataset of [$\partial \lambda/\partial t$, $(\partial \lambda/\partial x)^2$, $\partial^2 \lambda/\partial x^2$] evaluated along an equi-λ line will satisfy the diffusion equation with common D and $\partial D/\partial \lambda$. In other words, the trajectory of [$\partial \lambda/\partial t$, $(\partial \lambda/\partial x)^2$, $\partial^2 \lambda/\partial x^2$] will sit on a single plane, of which the normal vector is (-1, $\partial D/\partial \lambda$, D). However, this procedure for determining D and $\partial D/\partial \lambda$ is applicable only when the data set of [$\partial \lambda/\partial t$, $(\partial \lambda/\partial x)^2$, $\partial^2 \lambda/\partial x^2$] has enough curvature so that the normal vector of a plane containing the trajectory can be uniquely found. This is the case when the trajectory is evaluated along a low equi-λ line as illustrated in Figure 35 (a). All the data of spatial and temporal derivatives of water content were evaluated from a numerical simulation and the uncertainty of determining D and $\partial D/\partial \lambda$ from the normal vector of the fitted plane was found to be less than 3 %.

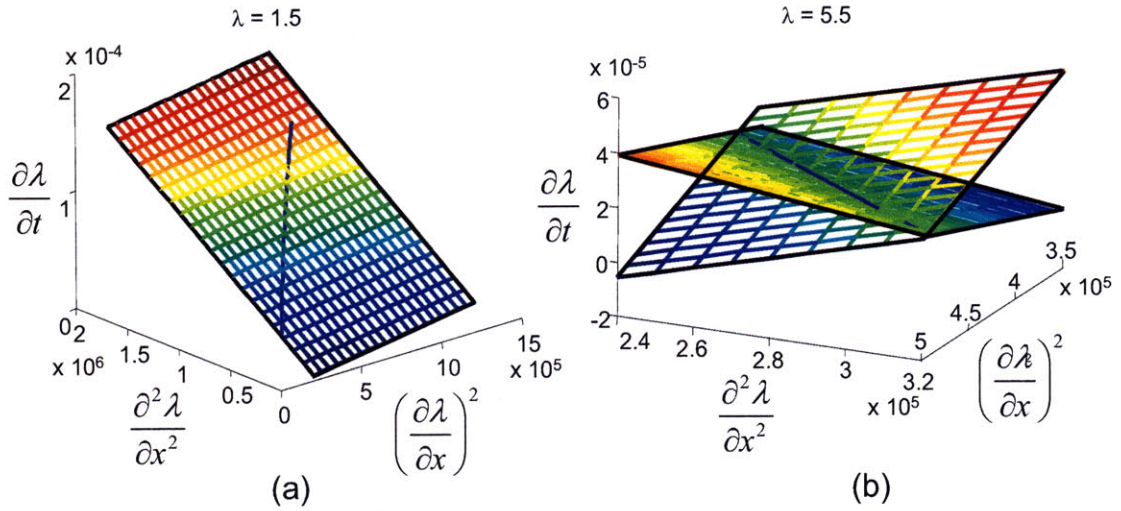

Figure 35. Mathematical procedure for determining D and $\partial D/\partial \lambda$. The trajectory of [$\partial \lambda/\partial t$, $(\partial \lambda/\partial x)^2$, $\partial^2 \lambda/\partial x^2$] evaluated along an equi-λ line of (a) 1.5 and (b) 5.5.

In the case of a high equi-λ line, however, the trajectory tends to become almost straight and it is difficult to determine a unique plane containing the trajectory as shown in Figure 35 (b). This problem can be resolved by numerical integration of D with respect to the water content. First, D and $\partial D/\partial\lambda$ are determined at a low equi-λ line. Then, D for the next λ is determined by adding $\partial D/\partial\lambda \times d\lambda$ to the previous D. For the next equi-λ line, it is not necessary to find an equation of a plane since D is already determined from the previous step, and only $\partial D/\partial\lambda$ is left to be unknown, which can be easily determined by linear fitting between $(\partial\lambda/\partial t - D\partial^2\lambda/\partial x^2)$ and $(\partial\lambda/\partial x)^2$. By repeating the procedure, it is possible to obtain D as a function of water content.

The validity of the mathematical procedure explained above was checked by a numerical simulation. For this purpose, a profile of chemical diffusion coefficients as a function of water content was predefined as shown in Figure 36 and the corresponding distribution of water content diffusing from one side of the simulated domain was generated as a function of time and position by an explicit method with the time and the space interval of 1 sec and 10 μm, respectively.

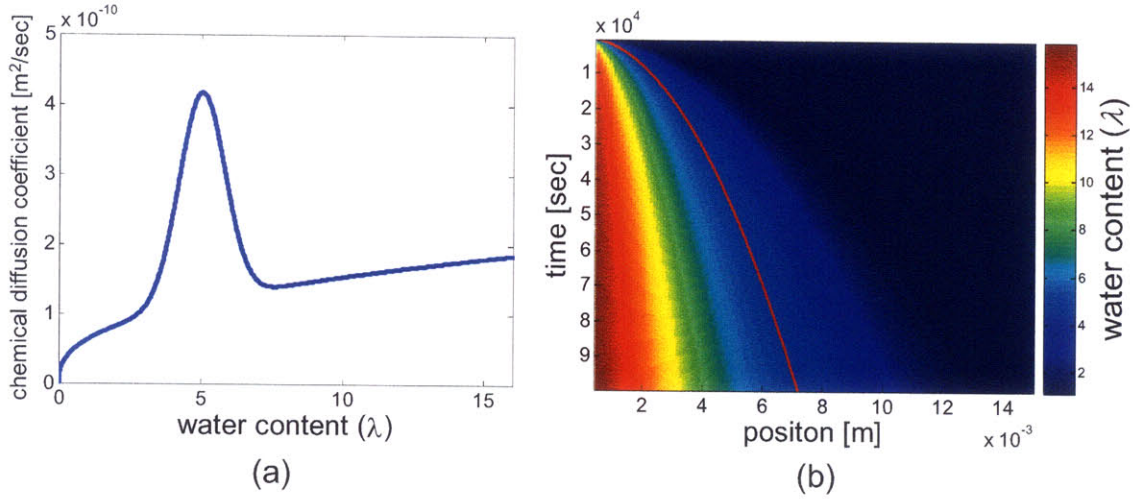

Figure 36. (a) A predefined profile of chemical diffusion coefficients as a function of water content and (b) the temporal and spatial distribution of water content generated from (a) with the indication of a contour line of $\lambda = 5$ (solid red line).

Although the shape of the chemical diffusion coefficient profile was determined so that it

resembled those found from the papers of Springer[105] and Motupally,[106] it is not physically meaningful and only serves as the reference with which a profile back-calculated from the data of water content distribution using the mathematical scheme will be compared. The first step of the mathematical scheme is to obtain maps of the spatial and temporal derivatives of the water content as shown in Figure 37.

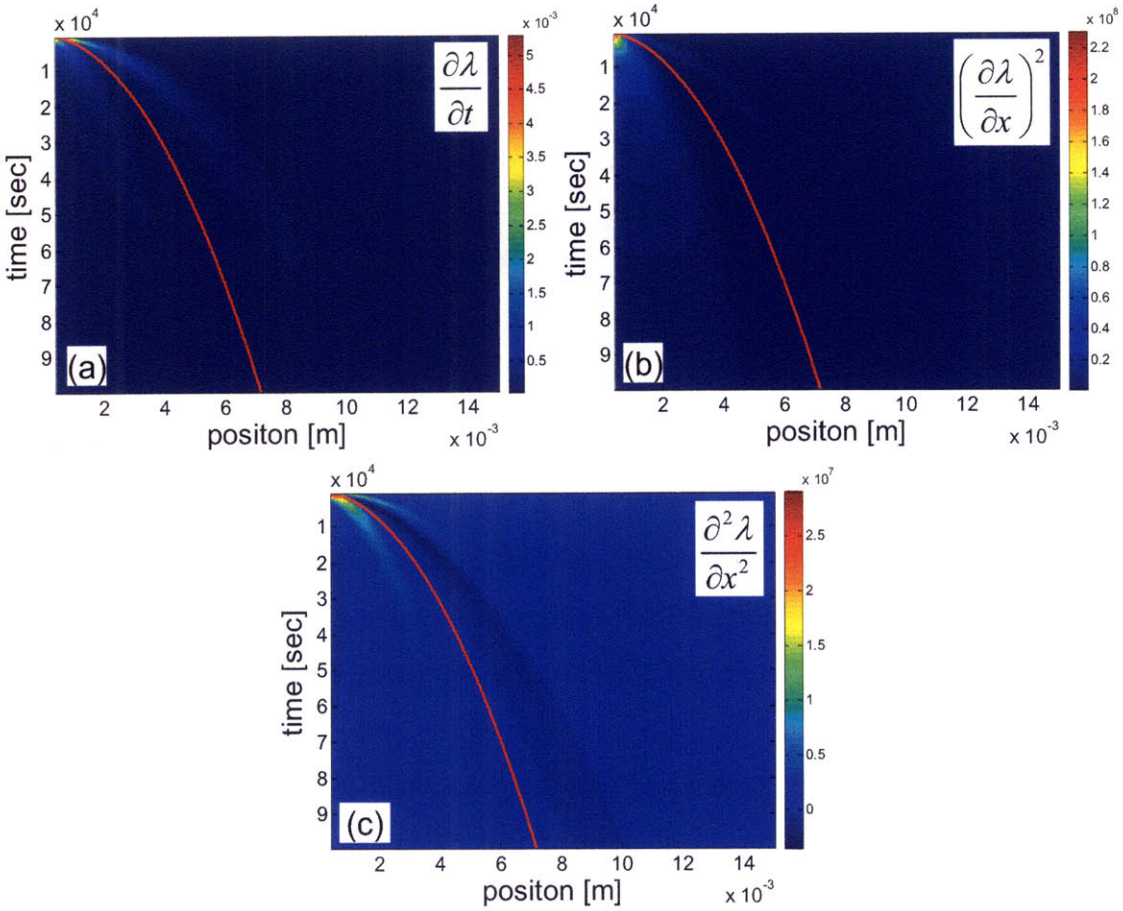

Figure 37. Distribution of (a) $\partial\lambda/\partial t$, (b) $(\partial\lambda/\partial x)^2$, and (c) $\partial^2\lambda/\partial x^2$ with the indication of a contour line of $\lambda = 5$.

The next step is to collect the values of the three derivatives along an equi-λ line as indicated by a solid red line in Figure 36 and Figure 37 for an example of $\lambda = 5$. The data set of these values forms a trajectory similar to those in Figure 35, which is used for three dimensional surface fitting or two dimensional line fitting depending on the curvature of the trajectory. The chemical diffusion coefficients as a function of water content can be

obtained by the method of numerical integration explained above and the results are shown in Figure 38.

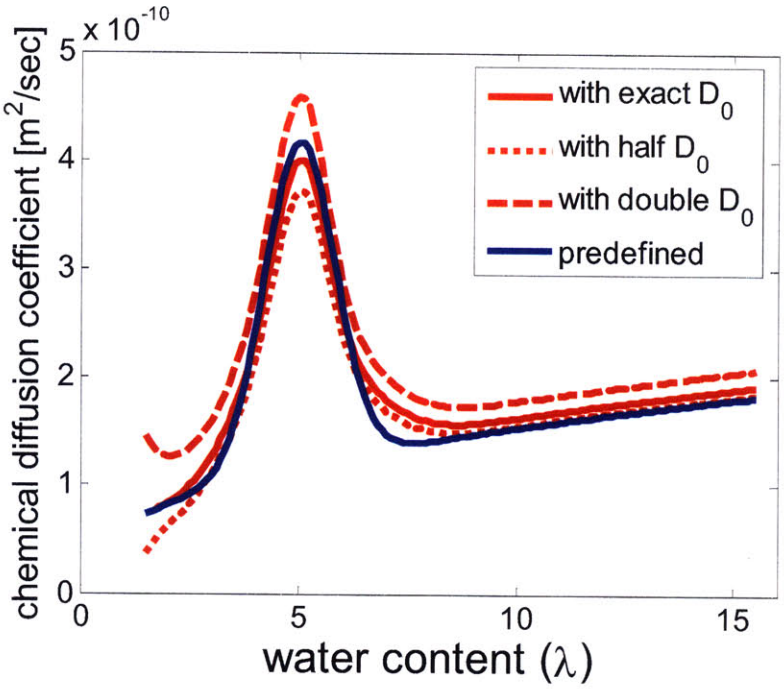

Figure 38. Comparison of the profile of the chemical diffusion coefficients back-calculated from the distribution of water content as a function of time and position to the predefined profile with various initial values of the numerical integration.

The agreement between the predefined profile of the chemical diffusion coefficients and that back-calculated from the distribution of water content as a function of time and position is decent in general. In addition, the effect of the uncertainty in the initial value for the numerical integration was examined by intentionally changing the initial value to the double or the half of the exact one because the initial value determined by the surface fitting may contain an error depending on the quality of the fitting and the curvature of the data. Fortunately, the effect is not significant and the back-calculated chemical diffusion coefficients follow the predefined profile very well in both the cases.

It is also important to examine the tolerance of this mathematical procedure to the noise which may be included in the data of water content distribution experimentally measured by laser interferometry. The data of water content distribution in Figure 36 (b) was intentionally contaminated by random noise as shown in Figure 39 (a) and the spatial

and temporal derivatives of the water content were evaluated again. Since the water content data contained noise, the evaluation of the derivatives required local curve fitting of a certain width of the data to a polynomial and taking the derivative of it. The data width of 500 sec and 0.5 mm were arbitrarily chosen for the evaluation of temporal and spatial derivatives, respectively. In fact, these widths should be selected carefully because too small width will make the evaluated derivatives very noisy while too large width will result in the loss of the fine details of the water content data. Figure 39 (b) is the comparison between the predefined profile and the back-calculated profile from Figure 39 (a).

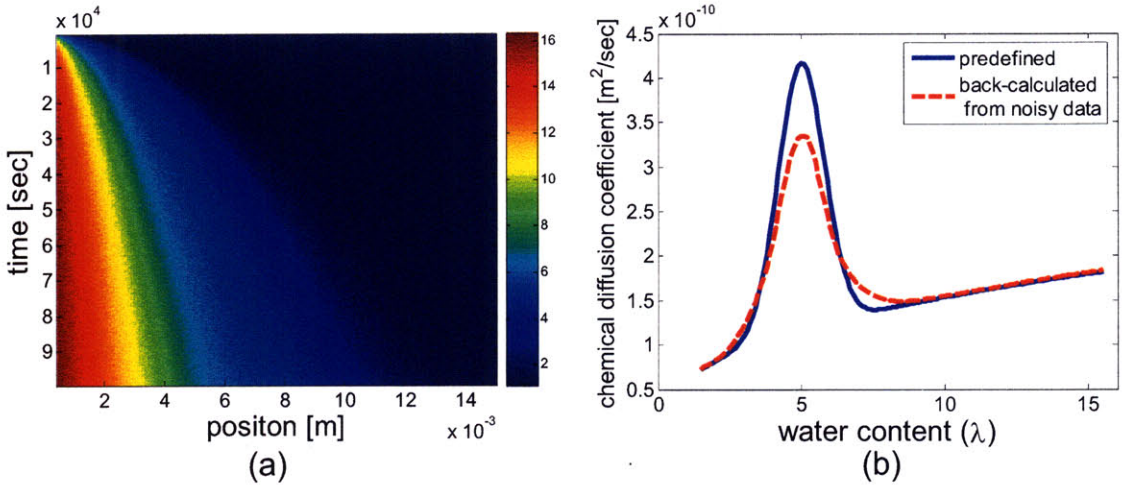

Figure 39. (a) Distribution of water content contaminated by random noise. (b) The profile of chemical diffusion coefficients back-calculated from (a). Data width of 500 sec and 0.5 mm were used for the evaluation of temporal and spatial derivatives, respectively.

The agreement between the two profiles is still good even with the noise level of ~3 % though the profile back-calculated from the noisy data fails to capture the sharp features of the predefined profile. It is also noted that the data width of 500 sec and 0.5mm for the evaluation of the local derivatives were appropriate.

5.3 Determination of Electro-osmotic Drag Coefficients

When proton flux is introduced to a Nafion® membrane, the last term of Eq. 38 is no longer zero and it is necessary to solve for 3 unknowns, D, $\partial D/\partial\lambda$, and

$\partial EOD / \partial \lambda$, which can be determined simultaneously using 4 dimensional surface fitting. However, this is practically impossible especially when the data of water content distribution as a function of time and position measured by laser interferometry is very susceptible to noise. Therefore, a different approach is used to reduce the number of unknowns. Although it is impossible to control diffusion process which naturally occurs with concentration gradient, electro-osmosis can be easily controlled by turning on and off the proton current through Nafion® membranes. If a step function as illustrated in Figure 40 is introduced in controlling proton current and the transient responses of water uptake before and after the step are compared, the effect of diffusion is separated from that of electro-osmosis and only $\partial EOD / \partial \lambda$ remains unknown as explained in Eq. 40 ~ Eq. 42.

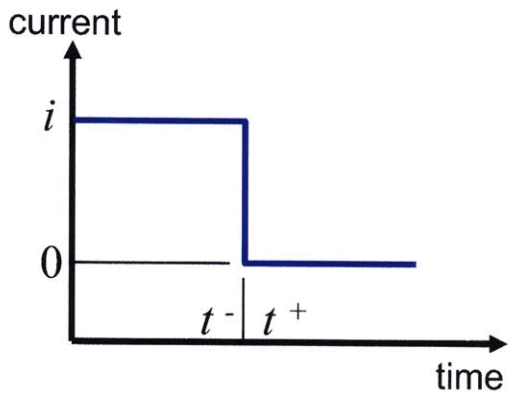

Figure 40. Step function in controlling proton current in order to turn on and off the electro-osmosis.

$$\left.\frac{\partial \lambda}{\partial t}\right|_{t^-} = \frac{\partial D}{\partial \lambda}\left(\frac{\partial \lambda}{\partial x}\right)^2 + D\frac{\partial^2 \lambda}{\partial x^2} - \frac{i}{d_0 \cdot w \cdot ec}\frac{EW}{Avo \cdot \rho_0}\frac{\partial EOD}{\partial \lambda}\frac{\partial \lambda}{\partial x} \qquad \text{Eq. 40}$$

$$\left.\frac{\partial \lambda}{\partial t}\right|_{t^+} = \frac{\partial D}{\partial \lambda}\left(\frac{\partial \lambda}{\partial x}\right)^2 + D\frac{\partial^2 \lambda}{\partial x^2} \qquad \text{Eq. 41}$$

$$\left.\frac{\partial \lambda}{\partial t}\right|_{t^-} - \left.\frac{\partial \lambda}{\partial t}\right|_{t^+} = -\frac{i}{d_0 \cdot w \cdot ec}\frac{EW}{Avo \cdot \rho_0}\frac{\partial EOD}{\partial \lambda}\frac{\partial \lambda}{\partial x} \qquad \text{Eq. 42}$$

Since partial derivatives of water content can be evaluated from the results of laser interferometry and all the other values are constant, $\partial EOD / \partial \lambda$ as a function of λ can be

determined by comparing the left and right hand sides of Eq. 42 and subsequently integrated to get the coefficient of electro-osmotic drag as a function of water content. The integration constant can be determined from the fact that $EOD(\lambda = 0) = 0$, which means that no water molecules are dragged when there are no water molecules in Nafion® membranes.

The validity of the mathematical procedure for determining the coefficients of electro-osmotic drag was also examined by a numerical simulation. The simulation was performed in a similar way to that for determining chemical diffusion coefficients. The profiles of chemical diffusion and electro-osmotic drag coefficients were predefined as shown in Figure 41.

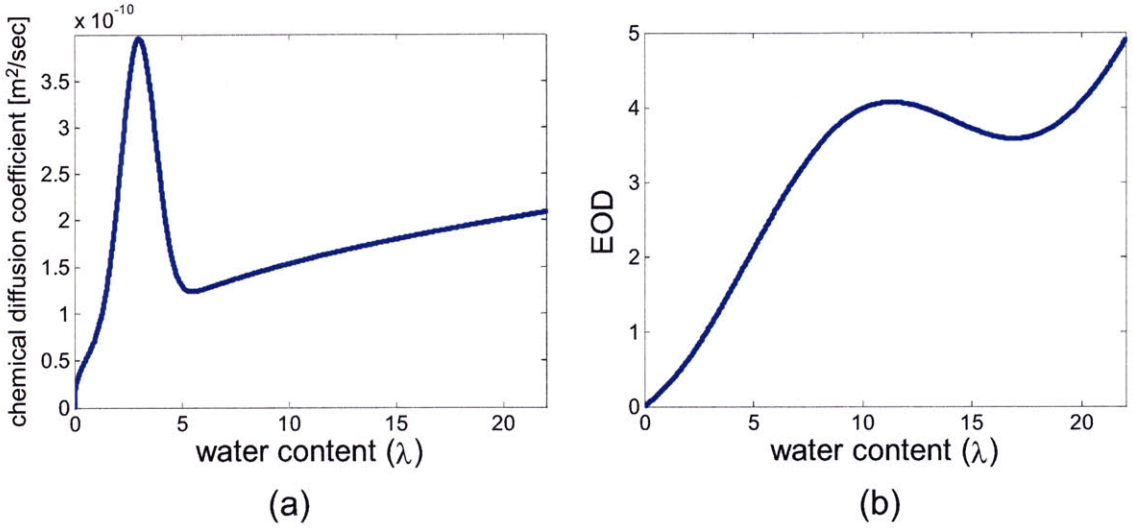

Figure 41. Predefined profiles of (a) chemical diffusion coefficients and (b) electro-osmotic drag coefficients as a function of water content. The predefined profile of electro-osmotic drag serves as a reference to which a back-calculated profile will be compared for examining the feasibility of the mathematical scheme.

The profile of chemical diffusion coefficients is similar to that for used for the diffusion simulation in the previous section, but slightly modified so that the maximum value of the chemical diffusion coefficients takes place at $\lambda = 3$. The profile of electro-osmotic drag was arbitrarily made up to have an overall magnitude similar to those found in the literature.[18,77-79] These profiles are not physically meaningful, but serve as a reference to

which a back-calculated profile will be compared for evaluating the feasibility of the mathematical scheme. The wavy feature in the profile of electro-osmotic drag coefficients was intentionally introduced to check how well the numerical integration reproduces the predefined profile which is more complex than one with monotonic increase.

Another predefined profile required for the numerical simulation is a step function of the proton current controlling, which is shown in Figure 42.

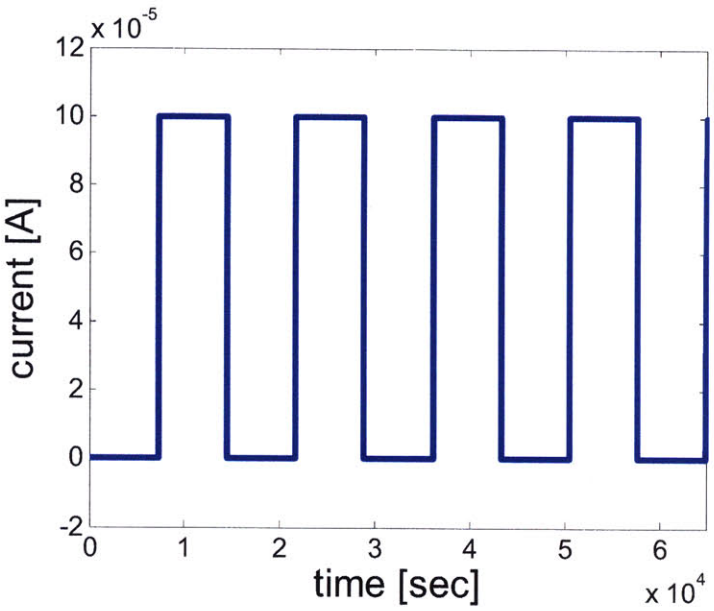

Figure 42. Profile for a step function to control the proton current. Steps between 100 μA and 0 μA are repeated at every 2 hours.

All of these predefined profiles in Figure 41 and Figure 42 combined with the governing equation of Eq. 38 generated a distribution of water content as a function of time and position while diffusion and electro-osmosis were occurring simultaneously. The simulation used an explicit algorithm with the time and space interval of 1 sec and 10 μm, respectively, and the result is shown in Figure 43. The equi-λ lines indicated by a solid red line for an example of $\lambda = 5$ have wavy features, which clearly show the effects of the step function in controlling the proton current.

It is now possible to back-calculate the coefficients of electro-osmotic drag from the distribution of water content using Eq. 42 at any instance when the step of the proton current occurs. The 8^{th} step was chosen because it provides the finest evaluation of

$\partial EOD / \partial \lambda$ as a function of λ. The procedure is illustrated in Figure 44.

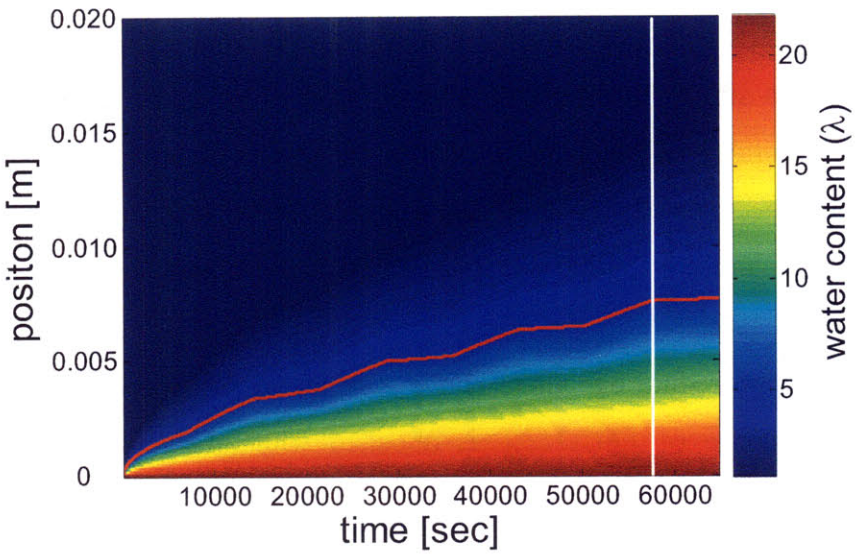

Figure 43. Distribution of water content as a function of time and position while water is absorbed by diffusion and electro-osmotic drag from the bottom (position = 0 m) to the top (position = 0.02 m). The solid red line is an equi-λ line of $\lambda = 5$. The solid white line indicates the 8th step of the proton current.

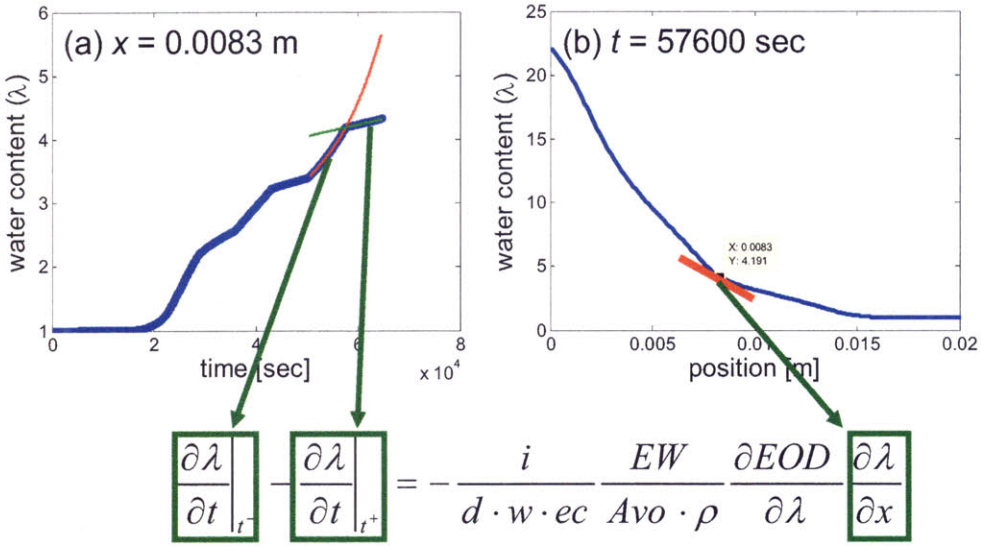

Figure 44. Procedure for evaluating $\partial EOD / \partial \lambda$ as a function of λ from partial derivatives of water content. (a) Evaluation of the temporal derivative before and after the step. (b) Evaluation of the spatial derivative.

The evaluation of a temporal derivative before after the step was performed by local fitting of the data of water content distribution with a time span of 2 hours, which is the interval between steps, to a polynomial and taking its derivative. A spatial derivative was also evaluated in a similar manner with a space span of 0.5 mm. Then, the difference between the temporal derivatives is divided by the spatial derivative to get a value of $\partial EOD/\partial\lambda$ at a specific water content. The example shown in Figure 44 is for the case of x = 0.0083 m and t = 57600 sec (the 8th step) from which $\partial EOD/\partial\lambda$ can be evaluated for $\lambda = 4.191$.

When the procedure explained above is repeated for every position along t = 57600 sec, a sequence of $\partial EOD/\partial\lambda$ is obtained with an enough resolution to be integrated in terms of λ, as shown in Figure 45.

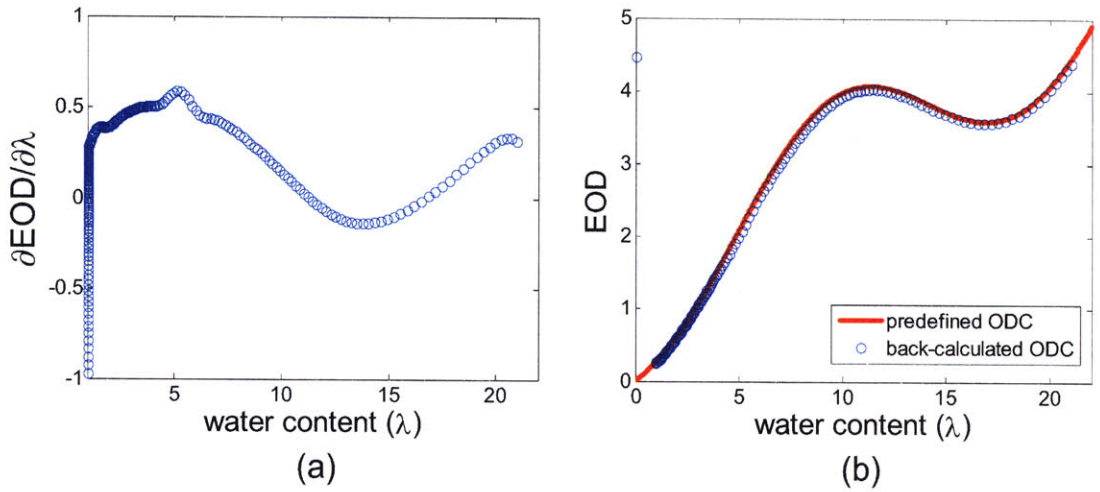

Figure 45. (a) $\partial EOD/\partial\lambda$ as a function of water content evaluated from the data of water content distribution. (b) Coefficients of electro-osmotic drag obtained by the numerical integration of $\partial EOD/\partial\lambda$ in terms of λ.

The agreement between the predefined profile of electro-osmotic drag coefficients and the back-calculated one is very good, which confirms the feasibility of the mathematical procedure.

The effects of the uncertainty which may be included in the measurement of the distribution of water content was examined by adding random noise normally distributed

with standard variation of 0.2 to the data of Figure 43, as depicted in Figure 46.

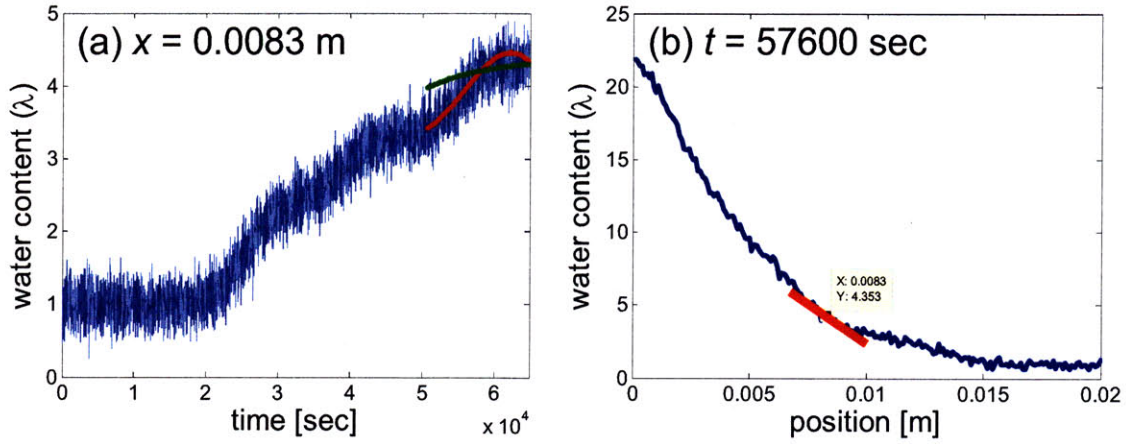

Figure 46. Water content distribution with intentional random noise taken at the same position and time as Figure 44. (a) Temporal distribution. (b) Spatial distribution.

The same procedure for back-calculating the coefficients of electro-osmotic drag was followed and the results are compared with those from the clean data in Figure 47.

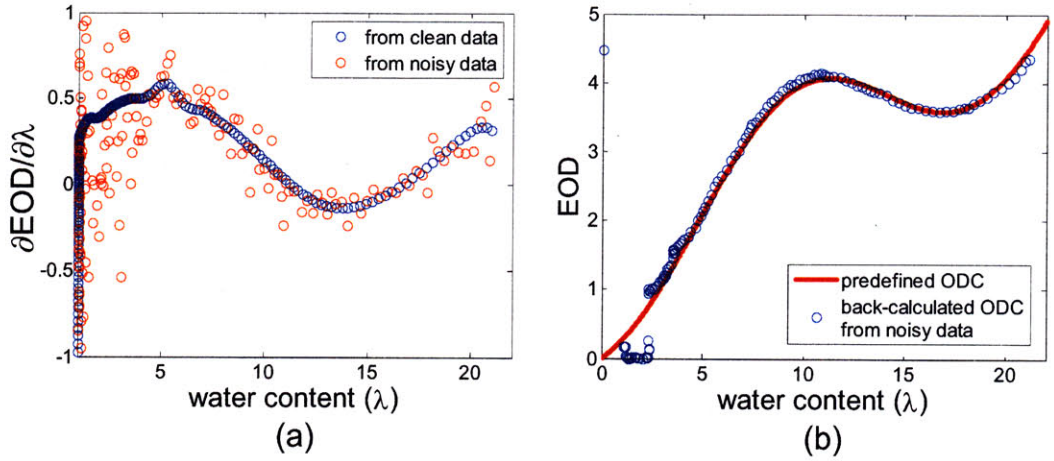

Figure 47. (a) Comparison of $\partial EOD / \partial \lambda$ as a function of water content evaluated from the clean data and the noisy data. (b) Coefficients of electro-osmotic drag obtained by the numerical integration of $\partial EOD / \partial \lambda$ evaluated from the noisy data.

The data of $\partial EOD / \partial \lambda$ evaluated from the noisy data was found to scatter more than that from the clean data especially in the region of low water content. However, the

corresponding *EOD* as a function of λ decently reproduced the predefined profile by virtue of integration, which inherently reduces the effect of noise.

To conclude Chapter 6, mathematical procedures to evaluate the coefficients of diffusion and electro-osmotic drag as a function of water content from the distribution of water content as a function of time and position were developed. The procedures rely on the direct observation of local partial derivatives of water content as input data to the governing equation. The feasibility of the mathematical schemes was confirmed by numerical simulations. It was also found that they are quite robust to noise which may be included during the measurement of water content by laser interferometry.

Chapter 6. Experimental Determination of Chemical Diffusion Coefficients

There have been various studies to experimentally determine the water diffusion coefficients in Nafion® membranes.[16,19,74-76] The determination of diffusion coefficients was carried out mostly through NMR (Nuclear Magnetic Resonance) studies.[16,74-76] However, NMR technique allows only the measurements of self-diffusion coefficients, not chemical diffusion coefficients which describe the transport of water under concentration gradient and better explain the net flux of water within the membranes during fuel cell operation. Even though chemical diffusion coefficients can be calculated from self-diffusion coefficients using a thermodynamic relationship,[16,105,106] the conversion requires a measurement of the water content of Nafion® as a function of water activity which is time consuming and adds uncertainty in evaluating chemical diffusion coefficients.

In the previous chapters, it has been demonstrated that the laser interferometry is a powerful tool to visualize and quantify the changes of the water content in Nafion® membranes with adequate temporal and spatial resolutions to capture the water transport phenomena. Also, the use of water content distribution measured by the laser interferometry combined with the governing equation allows the evaluation of the chemical diffusion coefficients as a function of the water content as discussed in Chapter 5.

In this chapter, the experimental results of water diffusion into Nafion® membranes are presented. The experimental setup enables the determination of the chemical diffusion coefficients under various compressive stresses, which will give valuable information on the water transport in Nafion® membranes constrained between current collectors of a fuel cell. In addition, the results of methanol diffusion experiments are presented, which will not only prove the versatileness of the technique, but also contribute to the study of direct methanol fuel cells.

6.1 Experimental

The Mach-Zehnder interferometer shown in Figure 13 and the sample holder

shown in Figure 14 were used to detect changes in water content during diffusion processes of water or methanol. Dry samples of Nafion® 117 were prepared in the same way as explained in Chapter 2. Diffusion of water or methanol into Nafion® samples was introduced by immersing the bottom side of an initially dry membrane into liquid water or pure liquid methanol. Two glass plates sandwiched the Nafion® sample to keep it flat during the measurement and prevent evaporation of water or methanol from the surface. The variation in the optical path length was monitored by the interferometer as a function of time and position. 2 compressive springs (Associated Spring, 020-089) were used to control the stress level in Nafion® samples. The springs had a spring constant of 1.26 N/mm and the pitch of the thread used for controlling the length of the springs was 1.27 mm/turn. The number of turns defined the force exerted by the springs, which was chosen to be 10, 20, and 25 turns. Correspondingly, the force exerted by one of the springs was 16, 32, and 40 N. The Nafion® samples had an area of 50 mm × 12.7 mm. Since the glass plates were rigid enough and no bending was observed with these force conditions, a uniform pressure was imposed on the samples, which were 50.4 kPa, 100.8 kPa, and 126 kPa as summarize in Table 5.

Table 5. Pressure conditions imposed on Nafion® samples

# of turns	Thread pitch	Spring constant	Force	Sample area	Pressure
10	1.27 mm/turn	1.26 N/mm	2×16 N	50 mm × 12.7 mm	50.4 kPa
20			2×32 N		100.8 kPa
25			2×40 N		126 kPa

6.2 Results of Water Diffusion Experiments

Figure 48 (a), (c) and (e) show the variation of interference intensity during the water diffusion process under various pressure conditions as a function of time and the distance from the liquid water in which the bottom side of the Nafion® samples were immersed. These signals were treated by the signal processing procedure detailed in Chapter 2 to obtain the corresponding distributions of ΔOPL and subsequently converted to the distributions of water content by using the linearity, $\partial \Delta OPL / \partial \lambda = 0.01086 d_0$, discussed in Chapter 3.

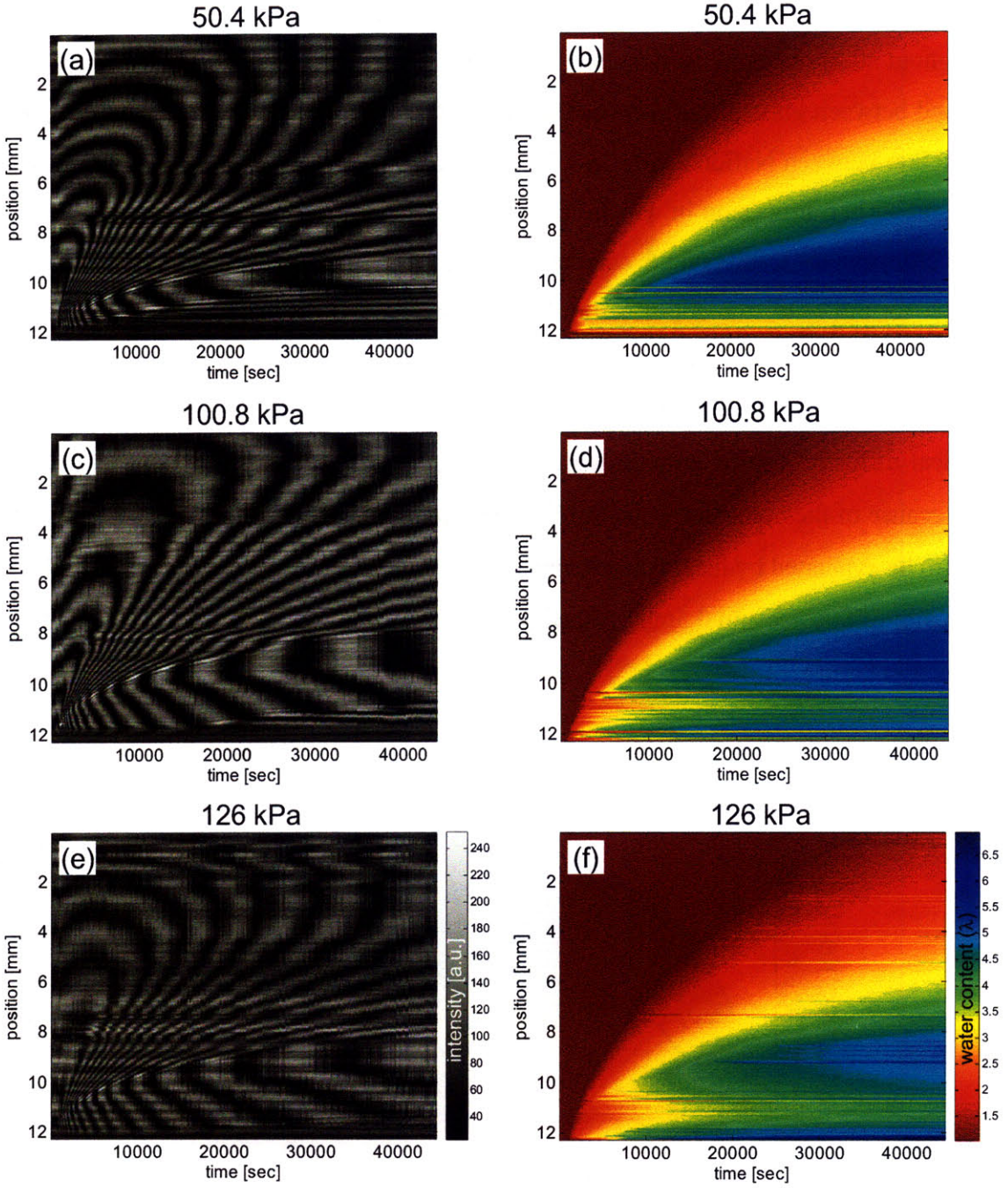

Figure 48. Distributions of the water content of Nafion® 117 membrane absorbing water, converted from interference intensity as a function of time and position under various conditions of compressive stress: (a) intensity under 50.4 kPa, (b) water content under 50.4 kPa, (c) intensity under 100.8 kPa, (d) water content under 100.8 kPa, (e) intensity under 126 kPa, and (f) water content under 126 kPa.

It is observed that the water uptake of Nafion® membranes is suppressed as the compressive stress increases. It is also noted that the maximum water content obtained throughout all of the experiments never exceeded 7 because the Nafion® membranes were clamped between glass plates and swelling in the lateral direction was not allowed due to the friction between Nafion® and glass. This confirms that water content of only 6~7 can be absorbed per dimension in which Nafion® is allowed to swell, which was the finding of the ellipsometry results on the constrained Nafion® membranes discussed in Chapter 3. In order for the water content of Nafion® membranes to exceed 7, the friction force must be overcome and slip must occur, which is not taken into account in our processing. Therefore, only the upper portion of the water content data was used for evaluating the chemical diffusion coefficients through the mathematical procedure detailed in Chapter 5.2. Because of the noise in the measured water content, λ (x, t), the partial derivatives of λ had to be evaluated by local curve fitting of λ (x = const, t) and λ (x, t = const) with the data width of 500 sec and 0.5mm, respectively. One example of taking partial derivatives is shown in Figure 49.

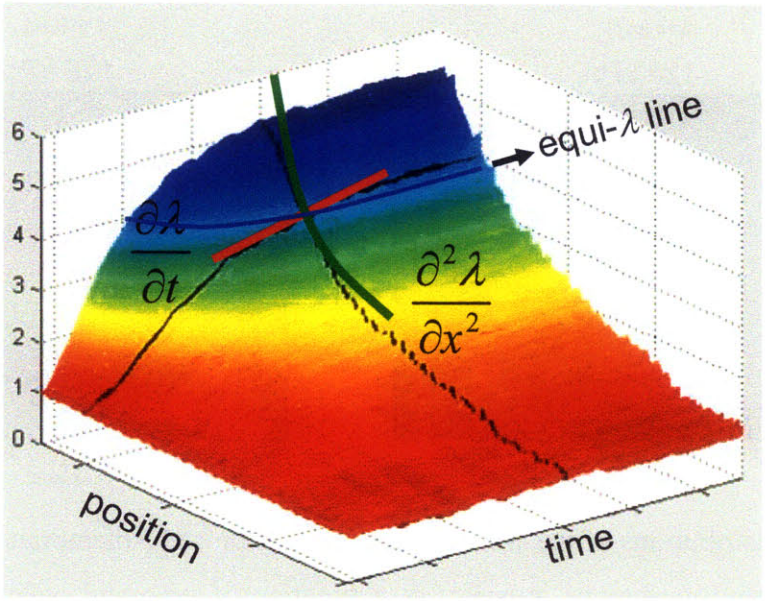

Figure 49. Evaluation of the spatial and temporal derivatives of water content experimentally determined by the laser interferometry.

These local curve fittings were repeated along an equi-λ line to generate a data set of

$[\partial\lambda/\partial t,\ (\partial\lambda/\partial x)^2,\ \partial^2\lambda/\partial x^2]$ and the mathematical procedure was performed to obtain the chemical diffusion coefficients as a function of the water content. It was already shown in Chapter 5 that these local curve fittings can effectively reduce the effects of noise and successfully retrieve the chemical diffusion coefficients. In order to examine this experimentally, two data sets of λ (x, t) collected along two vertical lines spaced by 1.2 mm were used to evaluate the chemical diffusion coefficients by the same mathematical procedure as shown in Figure 50. Even though the two data sets were measured from a single experiment by virtue of the laser interferometry setup, they can be considered independent of each other because the two vertical lines were apart enough compared to the microstructure of Nafion®, which has the length scale of ~10 nm.

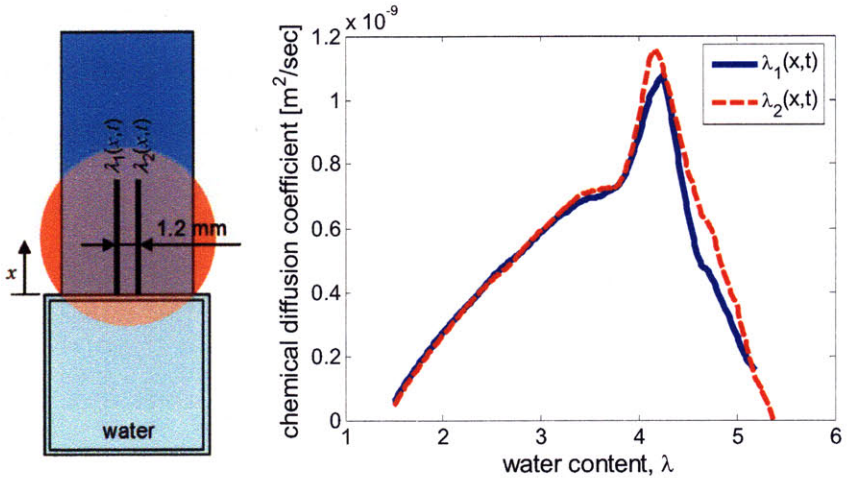

Figure 50. (a) Experimental setup for the diffusion of water with the indication of the vertical lines where two data sets of λ_1(x, t) and λ_2(x, t) were collected. (b) The chemical diffusion coefficients evaluated from λ_1(x, t) and λ_2(x, t) as a function of the water content.

The agreement between the two cases is very good except the slight difference of the peak values and the deviation in the high water content region. The decrease of peak height due to the noise was expected from the results of the simulation shown in Figure 39, but the difference between the two cases is not significant (~8 %). The deviation in the high water content is the results of insufficient data points for the linear fitting. In

other words, the number of data points included in a low equi-λ line is larger than that of a high equi-λ line, which makes the linear fitting performed on a high equi-λ line less reliable. Nevertheless, the general agreement between the chemical diffusion coefficients evaluated from two different locations of a Nafion® membrane verifies that the effect of the noise in the optical measurement of the water content is negligible. In addition, the result shown in Figure 50 confirms the assumption of one-dimensional diffusion and the repeatability of the mathematical procedure for extracting transport properties from the optical measurements of the water content of Nafion® membranes.

In general, the profile of the chemical diffusion coefficients shown in Figure 51 has a bell shape, which is in agreement with the results of Motupally,[106] who calculated the chemical diffusion coefficients of water by combining the self-diffusion coefficients and the equilibrium sorption of water into Nafion® membranes through the Darken factor. It is also found that the overall magnitude of the chemical diffusion coefficients decreases and the peak diffusivity occurs at lower water content as compressive stress increases.

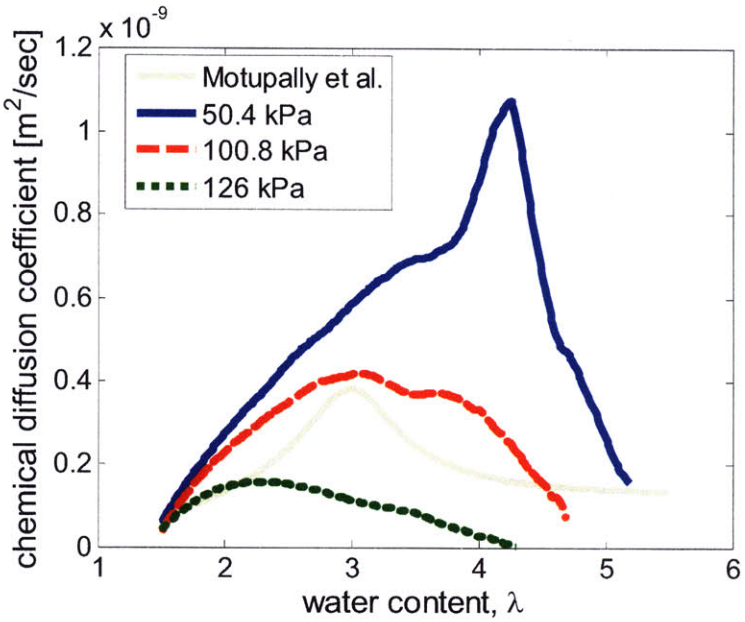

Figure 51. Chemical diffusion coefficients of water in Nafion® 117 membrane under compressive stresses of 50.4 kPa, 100.8 kPa, and 126 kPa as a function of water content, compared with the data from Motupally.[106]

6.3 Relationship between Chemical and Self- Diffusion Coefficients

In order to explain the effects of compressive stress on diffusion coefficients, the relationship between self-diffusion coefficients and chemical diffusion coefficients should be considered:[16,106]

$$D = D_{self} \frac{\partial \ln a_w}{\partial \ln \lambda}, \qquad \text{Eq. 43}$$

where D, D_{self}, a_w, and λ are chemical diffusion coefficient measured in this thesis, self-diffusion coefficient, activity of water, and water content, respectively. The detailed derivation of Eq. 43 can be found in Appendix B.

Jayakody[76] measured the self-diffusion coefficients of water in Nafion® membranes under high pressure conditions using the NMR technique and found that the activation volume which is related to the decrease of the self-diffusion coefficients due to pressure ranged from 2.7 cm^3/mol to 13.2 cm^3/mol depending on the water content. However, the pressure conditions used in this thesis, 126 kPa at maximum, are too small to cause significant decrease in the self-diffusion coefficients. Therefore, it is proposed that the Darken factor, $\partial \ln a_w / \partial \ln \lambda$, is the parameter sensitive to pressure changes in order to explain the variations in the chemical diffusion coefficients due to pressure shown in Figure 51. Unfortunately, the measurement of the equilibrium relationship between the water activity and the water content of Nafion® membrane under compressive stress, which is necessary for evaluating the Darken factor, is not available from the laser interferometry or any other experimental techniques. However, Choi[24] modeled the sorption of water in Nafion® as a function of the water activity by considering chemically and physically absorbed water molecules which were balanced by the pressure internally built up within the membrane structure due to swelling. The equation of Choi[24] for the sorption can modified to include the effect of the pressure applied externally:

$$\left\{ \lambda_{i,V} - \frac{\lambda_{i,m} K_1 a_{i,V}}{(1-a_{i,V})} \left[\frac{1-(\nu+1)a_{i,V}^{\nu} + \nu a_{i,V}^{\nu+1}}{1+(K_1-1)a_{i,V} - K_1 a_{i,V}^{\nu+1}} \right] \right\}^{-1}$$
$$= a_{i,V}^{-1} \exp\left\{ \frac{\overline{V}_i}{RT} \left[\frac{\kappa \lambda_{i,V}}{\lambda_{i,V} + \overline{V}_M / \overline{V}_i} + P_{ext} - S\sigma \cos\theta \left(1 + \frac{\overline{V}_M}{\overline{V}_i \lambda_{i,V}} \right) \right] \right\} - 1 \qquad \text{Eq. 44}$$

where P_{ext} is the pressure applied externally and $\lambda_{i,V}$ is the water content of Nafion® equilibrated in water vapor at the activity of $a_{i,V}$. The other parameters are listed in Table 6.

Table 6. Parameter values employed in Eq. 44. Adapted from the Reference.[24]

Parameters	Value	Unit	Comment
$\overline{V}_M$	537	cm^3/mol	partial molar volume of Nafion®
$\overline{V}_i$	18	cm^3/mol	partial molar volume of water
S	210	m^2/cm^3	specific pore surface area
K_1	100	dimensionless	first ionization of constant of sulfuric acid
ν	4-6	dimensionless	number of chemical equilibrium steps of reaction
$\lambda_{i,m}$	1.8	dimensionless	monolayer coverage being bound
σ	72.1	mN/m	surface tension of water
θ	98	dimensionless	contact angle of saturated water vapor in Nafion®
κ	183	atm	effective spring constant of Nafion®

When the sorption of water into Nafion® equilibrated in water vapor with various values of P_{ext} is evaluated using Eq. 44, one can observe the decrease of the equilibrium water content at a fixed water activity as shown in Figure 52. However, the changes in the Darken factor evaluated from these water sorption curves by numerical differentiation are still minimal even though P_{ext} of 10 MPa was used, which is much bigger than the pressure conditions used for the diffusion experiments of this thesis. Therefore, it is concluded that one or more of the parameters listed in Table 6 should vary as a strong function of the pressure applied externally. Possible candidates are S, K_1, ν, $\lambda_{i,m}$ and κ. After various tests for sensitivity of the Darken factor to these parameters, it was found that the Darken factor or the water content at which the inflection of water sorption curve occurs is most sensitive to changing the monolayer coverage of Nafion®, $\lambda_{i,m}$.

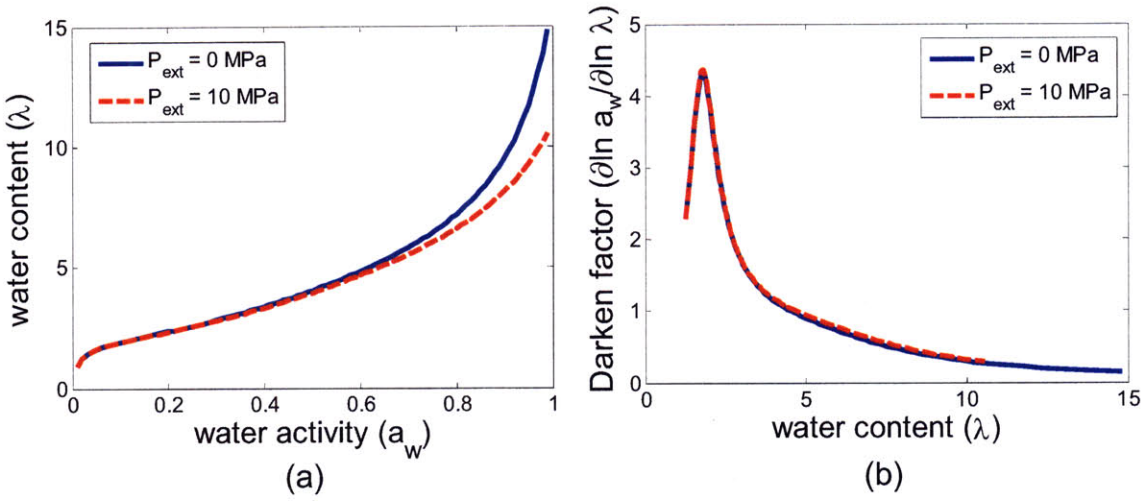

Figure 52. (a) Sorption of water into Nafion® as a function of the activity of water vapor evaluated by Eq. 44. (b) Darken factor, $\partial \ln a_w / \partial \ln \lambda$, calculated by numerical differentiation of the profile of water sorption. P_{ext} of 10 MPa results in no significant change.

Thampan[35] estimated the monolayer coverage, $\lambda_{i,m}$, from the specific pore surface area, S, using the following equation:

$$\lambda_{i,m} = \frac{S}{\rho_0} \frac{EW}{Avo \cdot A}, \qquad \text{Eq. 45}$$

where A is the surface area occupied by a water molecule on the pore surface and estimated to be 1.05×10^{-15} cm^2. Both Choi[24] and Thampan[35] used a constant monolayer coverage of 1.8 assuming the specific pore surface area, S, to be a constant value of 210 m^2/cm^3, which was calculated by Divisek[107]. However, this might not be accurate because $\lambda_{i,m} = 1.8$ always makes the peak value of the chemical diffusion coefficient occur at $\lambda = 1.8$, which does not agree with the finding of Springer[105] and Motupally[106] who showed that the peak occurred when $\lambda = 3$. In addition, the experimental results of this thesis show that the water content at which the maximum of the chemical diffusion coefficient is observed shifted from 4.2 to 2.2 as the compressive stress increases. Therefore, it is proposed that the monolayer coverage may not be constant, but decrease with increasing compressive stress in Nafion® because all of the pore surface area, S, may not be available for water uptake and the effective area can decrease as the compressive stress

increases.

In order to check the effect of changing $\lambda_{i,m}$, the sorption of water into Nafion® was evaluated again using Eq. 44 with $\lambda_{i,m}$ of 4.2, 3.2, and 2.2, which corresponded to the peak position of the chemical diffusion coefficients found in the diffusion experiments with the pressure condition of 50.4 kPa, 100.8 kPa, and 126 kPa, respectively. It is clear from Figure 53 that the water uptake is suppressed and the peak position of the Darken factor decreases with decreasing $\lambda_{i,m}$. Also, the maximum value of the evaluated Darken factor is found to be ~4.5 which indicates that the chemical diffusion can be enhanced due to the concentration gradient up to 4.5 times of the self diffusion.

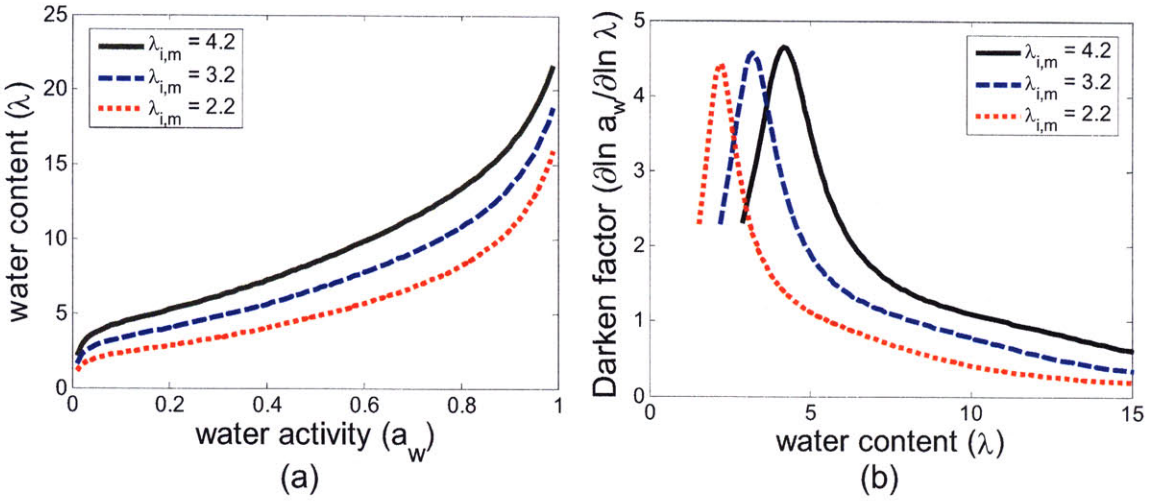

Figure 53. (a) Sorption of water into Nafion® as a function of the activity of water vapor evaluated by Eq. 44 with $\lambda_{i,m}$ of 4.2, 3.2, and 2.2. (b) Darken factor, $\partial \ln a_w / \partial \ln \lambda$, calculated by numerical differentiation of the profiles of water sorption.

The evaluated Darken factors can be used to calculate the chemical diffusion coefficients from Eq. 43 if the self-diffusion coefficients are known. Motupally[106] fitted six values of the self-diffusion coefficients measured by Zawodzinski[16] to get an empirical expression for the self-diffusion coefficients as a function of the water content:

$$D_{self} = 6.31\times10^{-11}(\lambda - 0.0209\lambda^2 - 0.501) \quad [m^2/\text{sec}], \qquad \text{Eq. 46}$$

which is plotted in Figure 54 (a).

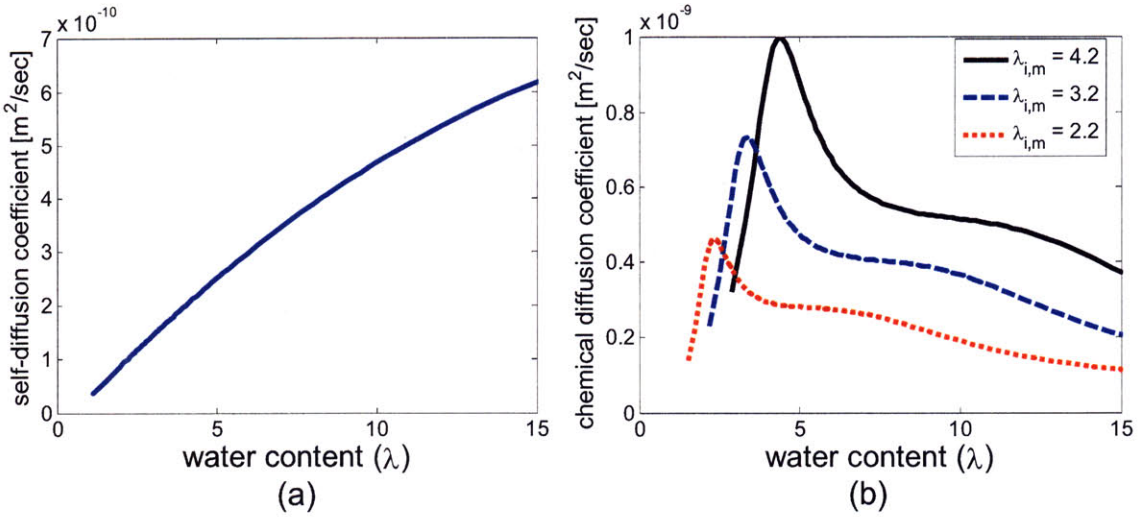

Figure 54. (a) Self-diffusion coefficients of water in Nafion® evaluated from the empirical expression of Eq. 46.[16,106] (b) Chemical diffusion coefficients calculated from Eq. 43 and the Darken factors evaluated with $\lambda_{i,m}$ of 4.2, 3.2, and 2.2.

The chemical diffusion coefficients calculated from Eq. 43 and the Darken factors evaluated with $\lambda_{i,m}$ of 4.2, 3.2, and 2.2 are plotted in Figure 54 (b), which shows similar features to those of Figure 51 such as the overall decrease of the magnitude of the chemical diffusion coefficients and the shift of the peak position. Therefore, it is concluded that the monolayer coverage, $\lambda_{i,m}$, is closely related to the compressive stress applied externally and determines the water content at which the peak value of the chemical diffusion coefficients is obtained.

6.4 Methanol Diffusion Experiments

The chemical diffusion coefficients of methanol can also be evaluated by taking the same procedures as done for water. One required step prior to this is the determination of the relationship between the methanol content and the optical path length of Nafion® membranes. The relationship is estimated by the calibration experiment and the mathematical model developed in Chapter 3.

6.4.1 Calibration Experiment

A Nafion® 117 membrane equilibrated in pure liquid methanol (Sigma-Aldrich,

≥99.8 %) was quickly assembled in the sample holder shown in Figure 18 after removing the droplets of methanol on the surface of the sample. During the evaporation process of methanol, the decrease in ΔOPL and the changes in the weight were measured by the Mach-Zehnder interferometer and the micro-balance, respectively. The variation in the interference intensity was converted to the decrease in the phase which is proportional to ΔOPL, as shown in Figure 55.

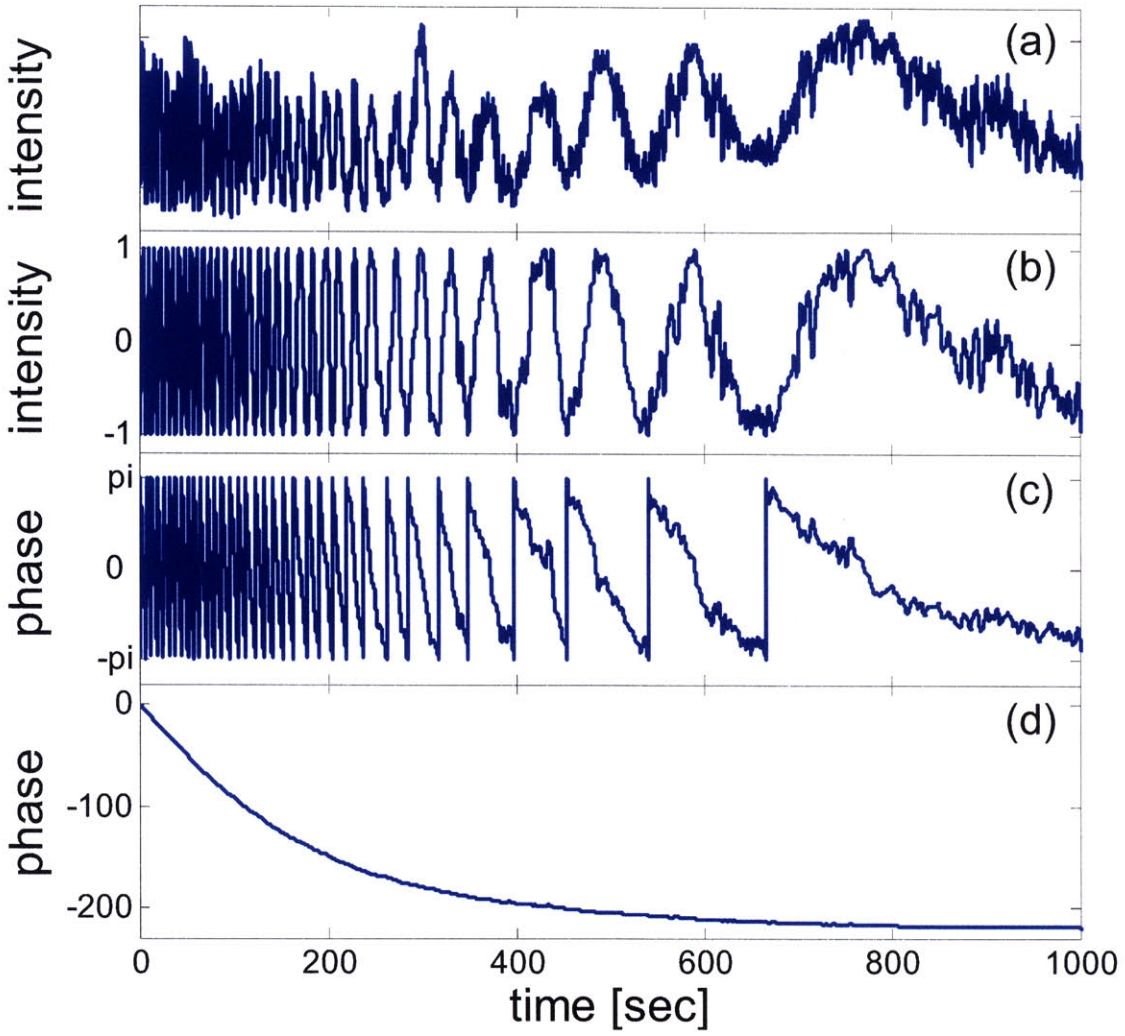

Figure 55. Procedure for retrieving phase information from interference intensity during the methanol calibration experiment. (a) Raw intensity. (b) Normalized intensity. (c) Wrapped phase. (d) Unwrapped phase.

ΔOPL converted from the unwrapped phase data and the methanol content, λ_m, calculated

from the changes in the weight are shown in Figure 56.

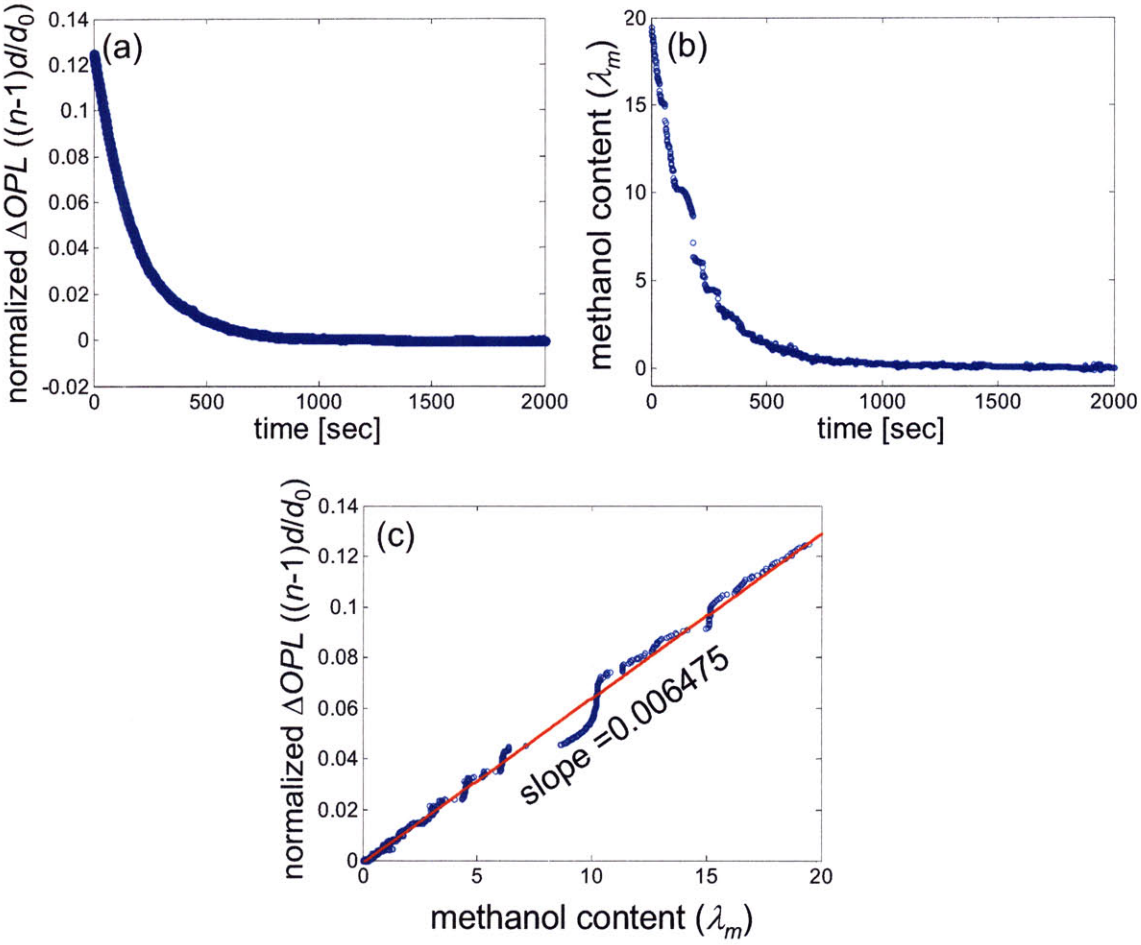

Figure 56. Results of the methanol calibration experiment. (a) Changes in ΔOPL during the evaporation of methanol, normalized by the initial thickness. (b) Changes in methanol content as a function of time. (c) Relationship between ΔOPL and methanol content.

The linear relationship between the ΔOPL and the methanol content of Nafion® is clearly seen, and the linearity was found to be:

$$\frac{1}{d_0}\frac{\partial \Delta OPL}{\partial \lambda_m} \approx \frac{1}{d_0}\frac{d[(n-1)d]}{d\lambda_m} = 0.006475 : \text{isotropic swelling} \qquad \text{Eq. 47}$$

However, this value is valid only for isotropic swelling and can not be used for experiments for methanol diffusion because the sample holder allows only uni-directional swelling.

6.4.2 Mathematical Modeling

As detailed in Chapter 3, the refractive index and the thickness of Nafion®-methanol mixture can be estimated based on the Lorentz-Lorenz rule and Eq. 21, Eq. 23, and Eq. 24 are rewritten as:

$$\frac{n_{mixture}^2 - 1}{n_{mixture}^2 + 2} = \left(k_{methanol} + \frac{k_{nafion}}{m} \right) \frac{m\rho_{nafion}}{1 + fm\rho_{nafion} / \rho_{methanol}} \quad \text{Eq. 48}$$

$$d = d_0 \left(1 + fm\rho_{nafion} / \rho_{methanol}\right): \text{ uni-directional swelling} \quad \text{Eq. 49}$$

$$d = d_0 \left(1 + \frac{1-\nu}{1+\nu} fm\rho_{nafion} / \rho_{methanol} \right): \text{ isotropic swelling} \quad \text{Eq. 50}$$

m is redefined as the ratio of methanol mass to that of dry Nafion® and has the following relationship to methanol content, λ_m:

$$m = \frac{M_{methanol}}{EW_{Nafion}} \lambda_m = \frac{32}{1100} \lambda_m \quad \text{Eq. 51}$$

In other words, λ_m is the number of methanol molecules contained in Nafion® per SO_3^-. The relationship between λ_m and $\Delta OPL = (n\text{-}1)d$ can be plotted using the equations and f = 0.96 found from the ellipsometry and ν = 0.4 or 0.5, as shown in Figure 57.

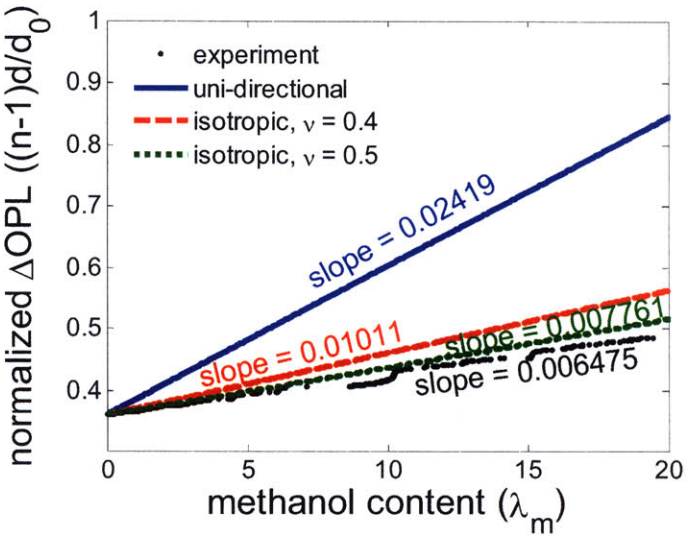

Figure 57. Relationship between λ_m and the normalized ΔOPL of Nafion®.

For the case of isotropic swelling, the slope between ΔOPL and methanol content is

estimated to be 0.01011 and 0.007761 with the assumption of ν = 0.4 and 0.5, respectively, both of which are higher than the experimental result, 0.007761. This may indicate that the swelling of Nafion® membranes during the calibration experiment for methanol uptake deviated from isotropic swelling. Methanol uptake leads to much more swelling than water uptake and can significantly decrease the Young's modulus of Nafion®. This effect makes the assumption of isotropic swelling invalid because the tension required to maintain the sample flat during the optical measurements is no longer small enough to be ignored when applied to a material with small Young's modulus. Nevertheless, a linear relationship between ΔOPL and λ_m was found from both experiments and calculations. The dependency for the case of uni-directional swelling is estimated to be:

$$\frac{1}{d_0}\frac{\partial \Delta OPL}{\partial \lambda_m} \approx \frac{1}{d_0}\frac{d[(n-1)d]}{d\lambda_m} = 0.02419 : \text{uni-directional swelling} \qquad \text{Eq. 52}$$

Eq. 52 will be used for converting ΔOPL to λ_m during the experiments for methanol diffusion.

6.4.3 Experimental Determination of Chemical Diffusion Coefficients of Methanol

Experiments for methanol diffusion were performed by using the sample holder shown in Figure 14 and the Mach-Zehnder interferometer shown in Figure 13. The bottom end of the Nafion® sample was immersed in pure liquid methanol (Sigma-Aldrich, ≥99.8 %) and the uptake of methanol was observed for about 14 hours. In order to examine the effect of compressive stress on the diffusion of methanol, the pressure exerted on the sample membranes was controlled by adjusting the spring force of the sample holder. The pressure conditions used were 50.4 kPa and 126 kPa. The interference intensities as a function of time and position captured during the diffusion process were processed by the method detailed in Chapter 2 to get the phase distribution. Then, the distribution of methanol content was obtained using the linear relationship of Eq. 52. The results are summarized in Figure 58. Similarly to the results from the water diffusion experiments, the data below ~8 mm was difficult to analyze because the slip between the glass plates and the Nafion® samples took place after the methanol content reached ~3. The increase in the thickness of Nafion® membranes with the methanol content of ~3 for

the case of uni-directional swelling can be estimated by Eq. 49, which results in the increase of ~21.1 %. In the case of water swelling, the maximum water content above which the slip occurred was found to be 6~7, which correspond to the thickness increase of 18.7~21.7 %. The consistency of these maximum thickness increases due to water uptake and methanol uptake indicates that Nafion® membranes can withstand about 20 % of thickness changes regardless of the diffusing liquid under the uni-directional swelling condition, although Nafion® membranes in free state swells much more in methanol than in water.

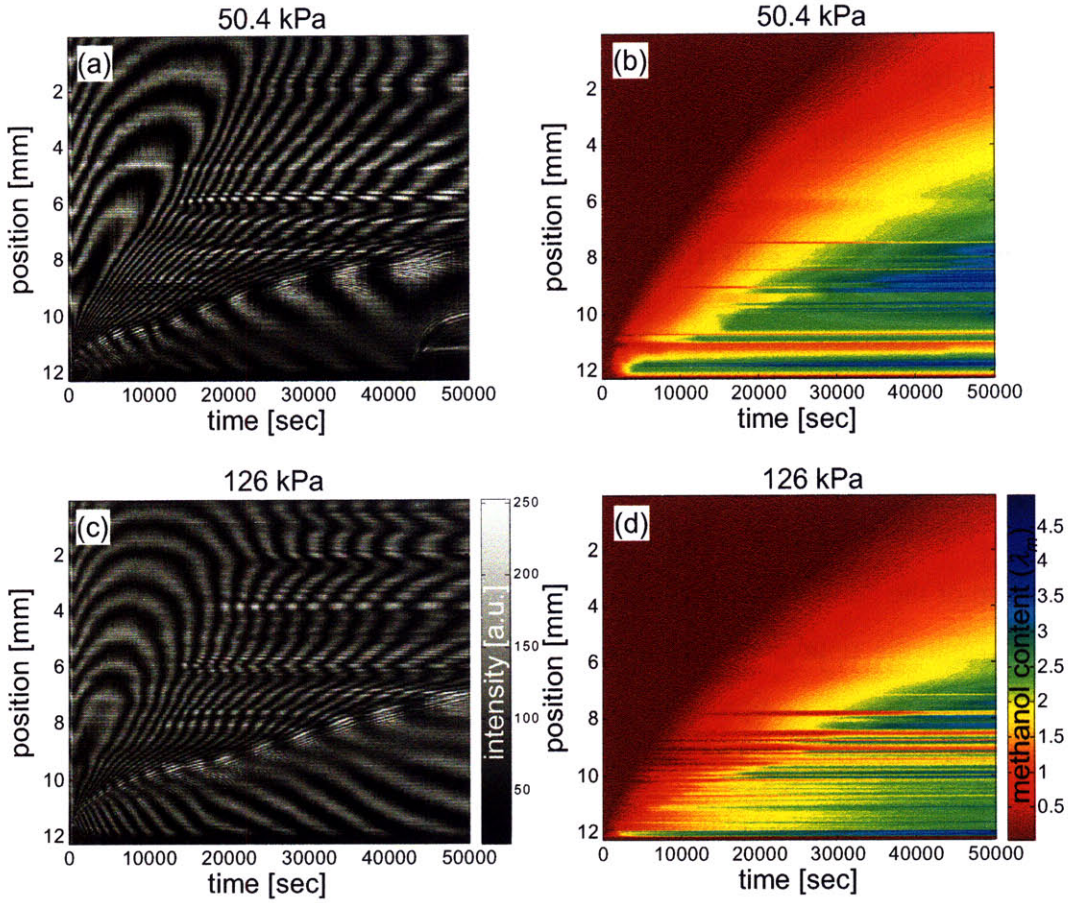

Figure 58. Distributions of the methanol content of Nafion® 117 membrane absorbing pure methanol (Sigma-Aldrich, ≥99.8 %), converted from interference intensity as a function of time and position under various conditions of compressive stress: (a) intensity under 50.4 kPa, (b) methanol content under 50.4 kPa, (c) intensity under 126 kPa, and (d) methanol content under 126 kPa.

Skou[108] and Gates[109] measured the methanol uptake of Nafion® 117 membranes in free state and found λ_m of 22 and 27, respectively. Assuming that isotropic swelling occurred in free Nafion® membranes, these values of methanol content correspond to the thickness increase of 36~42 %. The difference between the maximum thickness increases in isotropic and uni-directional swelling cases implies that the constraints in lateral directions limit not only swelling in the lateral directions, but also in the thickness direction, probably due to the 3 dimensional structure of the backbones of Nafion®. This effect is more severe for the case of methanol uptake, which showed a bigger difference between the two swelling cases than the case of water uptake.

The effect of the compressive stress on the speed of methanol uptake can be seen by comparing Figure 58 (b) and (d). However, the suppression of methanol uptake due to the compressive stress was subtle probably because the pressure of 50.4 kPa already hindered methanol diffusion significantly. In order to see the effect of compressive stress, the chemical diffusion coefficients of methanol were evaluated by the same procedure as detailed in Chapter 6.2. For this, local partial derivatives of the methanol content data were evaluated and subsequently used for evaluating D and $\partial D / \partial \lambda$, which are the two unknowns of the governing equation of Eq. 39. The results are shown in Figure 59.

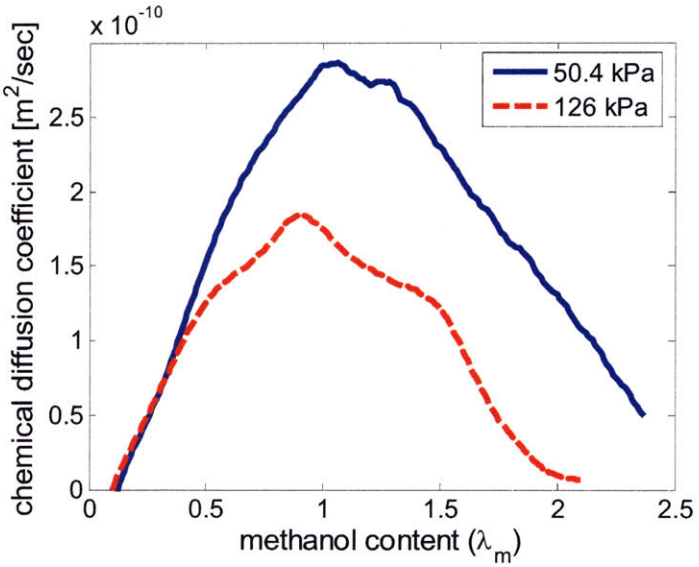

Figure 59. Chemical diffusion coefficients of methanol in Nafion® 117 membranes under compressive stresses of 50.4 kPa and 126 kPa as a function of methanol content (λ_m).

Similar trends to those from the water diffusion experiments are found: a bell shape profile with the decreasing overall magnitude and the peak position shifting down to the lower methanol content with increasing compressive stress. However, the overall magnitude of methanol chemical diffusion coefficients under the compressive of 50.4 kPa is quite smaller than that of water chemical diffusion coefficients.

There have been several studies to measure the self-diffusion coefficients of methanol in Nafion® membranes using the NMR technique.[80,110,111] The measured self-diffusion coefficients of methanol were in the range of $3\sim9\times10^{-10}$ m^2/sec depending on the researchers and did not vary much as a function of the methanol concentration. It is noted that the NMR technique required equilibrated samples which were prepared by immersing them into a water-methanol mixture, probably due to the lack of another proper method. This is why the self-diffusion coefficients of methanol did not drop sharply even at a very low concentration of methanol since the presence of water molecules would ease the transport of methanol. Therefore, a direct comparison between the chemical diffusion coefficients under no effect of water, shown in Figure 59, and the self-diffusion coefficients measured by NMR is not valid. However, it is noted that the overall magnitude of the self-diffusion coefficients of methanol and water is in a similar range.

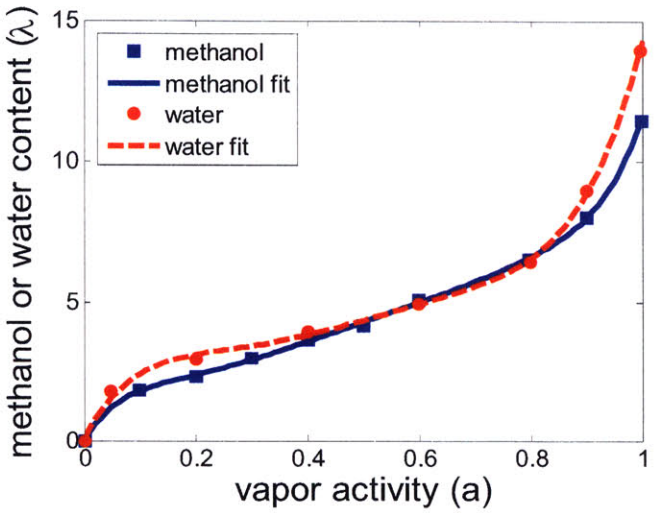

Figure 60. Water and methanol uptake as a function of the vapor activity. Adapted from the Reference.[112]

Jalani[112] measured the methanol and water uptake of a Nafion® 112 membrane equilibrated in a known vapor pressure of methanol or water at 30 °C as shown in Figure 60. Each data set of water or methanol sorption was fitted to a polynomial and the Darken factor of Eq. 43, required to correlate self and chemical diffusion coefficients, was evaluated by numerical differentiation, as shown in Figure 61.

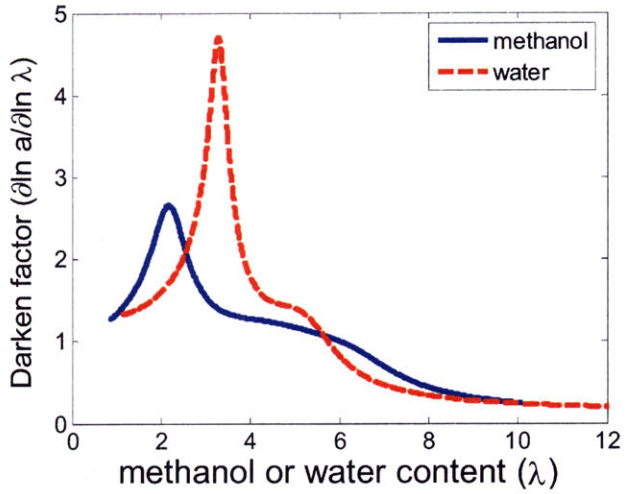

Figure 61. Darken factors as a function of methanol or water content calculated from the polynomial fits of the sorption data measured by Jalani.[112]

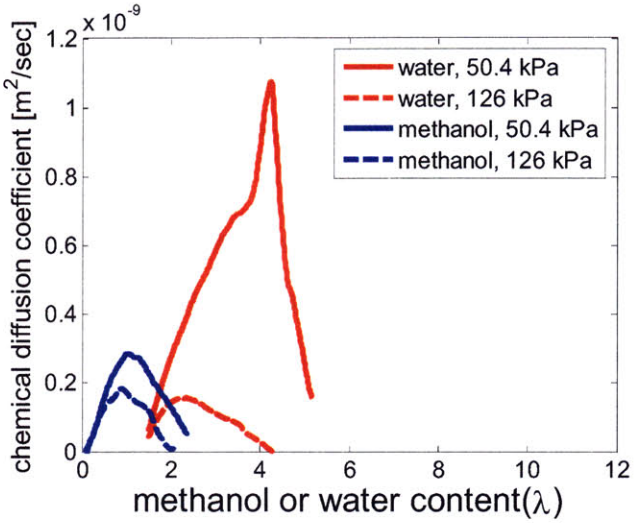

Figure 62. Comparison of the chemical diffusion coefficients of methanol and water. The general shape of the profiles agrees well with the Darken factors evaluated from the sorption data of methanol and water shown in Figure 61.

If the self-diffusion coefficients of methanol do not significantly change as a function of methanol content or compressive stress, the profile of the Darken factor will determine the profile of the chemical diffusion coefficients. Even though the Darken factors plotted in Figure 61 were evaluated from the sorption data obtained from a Nafion® membrane in free state, it is expected that the peak of each profile will shift to a lower methanol or water content by a similar amount and the height of the peak will not change significantly with increasing compressive stress, in a similar way shown in Figure 53 (b). Therefore, the use of Figure 61 for comparing the data shown in Figure 51 and Figure 59 is still valid. For the comparison, the experimentally determined chemical diffusion coefficients of methanol and water are plotted together in Figure 62. It is found that the maximum value of Darken factor for methanol is ~2.7 while that for water in ~4.7, which can explain the smaller chemical diffusion coefficients of methanol than those of water assuming that the self-diffusion coefficients of the two liquid are in a similar range. The peak position of the Darken factor of methanol is smaller that that of water, which also agrees with the experimental findings.

Even though there are not as many research efforts for theoretical modeling of methanol transport in Nafion® membranes as those for water, Chen[113] investigated the behavior of methanol in the mixture with Nafion®, protons, and water molecules by molecular simulation technique and concluded that all the species behaved as nanofluidics and traveled via the hydrophilic sulfonic acid groups. Therefore, it is believed that the transport mechanism of methanol would not be much different from that of water.

Even though the transport mechanisms are similar qualitatively, there may be a difference in the quantitative values of the properties resulting from the difference in the molar volume: $V_{m,methanol}$ = 40.4 cm^3/mol vs. $V_{m,water}$ = 18 cm^3/mol. This difference can be related to the higher slope of the equilibrium sorption data of methanol than that of water in the low λ_m or λ regions shown in Figure 60, which means each increase in the methanol content causes larger swell and more increase in the activity or the escaping tendency than water. Correspondingly, the Darken factor for methanol is evaluated to be smaller than that for water and thus the chemical diffusion coefficient. However, in the higher λ_m or λ regions, this trend breaks possibly due to the much greater uptake of

methanol into Nafion® and the following plastic deformation of the membrane.

6.5 General Discussion on the Diffusion of Water and Methanol in Nafion® Membranes

The profiles of the chemical diffusion coefficients of both pure water and pure methanol have been determined by using the water or methanol content data as a function of time and position measured by the laser interferometry, combined with the governing equation. The profiles showed a bell shape, which agrees well with the expectation derived from the self-diffusion coefficients and the sorption data via the Darken equation. One unique feature of the experimental and analytical technique developed in this thesis is the capability of determining the chemical diffusion coefficients in Nafion® membranes under compressive stress. It was found that the overall amplitude of the chemical diffusion coefficients was suppressed and the water or methanol content at which the maximum occurred shifted to lower values as the compressive stress increased.

Since the self-diffusion coefficients did not vary much within the range of compressive stress applied in this thesis,[76] the second term of the Darken equation, which can be evaluated from the equilibrium sorption data of water or methanol, is believed to have a strong dependency on compressive stress. By examining the sensitivity of the parameters in the model[24] for the equilibrium sorption of water, it was found that the monolayer coverage, $\lambda_{i,m}$, is the most suitable parameter to describe the effect of compressive stress on the chemical diffusion process. $\lambda_{i,m}$ is closely related to the specific pore surface area, S, and is regarded as a constant in many modeling studies.[24,35] From the observations of the experimental results and the comparison with the model for the equilibrium sorption, however, it is proposed that S and $\lambda_{i,m}$, that are linearly correlated, changes as a function of the compressive stress. This hypothesis is not unreasonable because not all the hydrophilic pores of Nafion® will be equally vulnerable to swelling when the membrane absorbs water molecules. In the case of no compressive stress, the hydrophilic pores experience relatively smaller resistance when they swell, resulting in the higher specific pore surface area, S. On the other hand, in the case of high compressive stress, the hydrophilic pores in general will undergo larger resistance to swell and the water molecules taken into the membrane will be concentrated at some

portions of hydrophilic pores where the water molecules are easily accommodated.

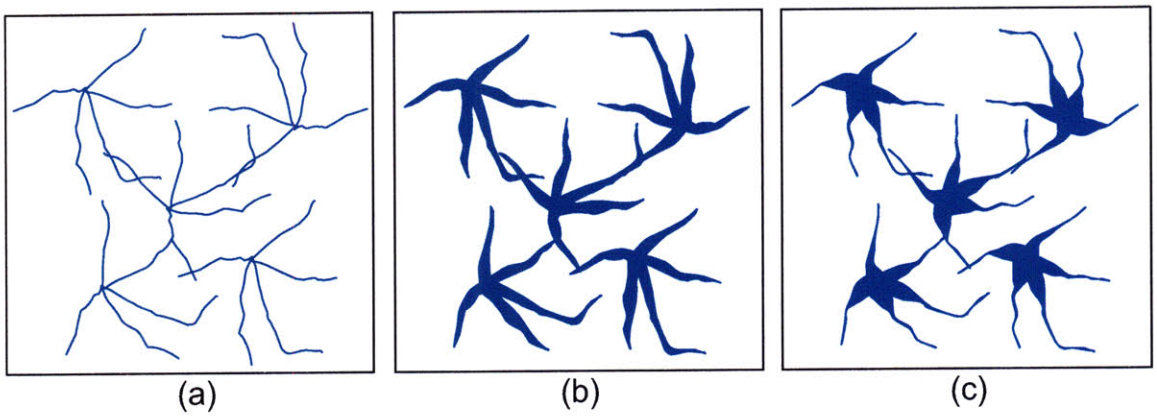

Figure 63. Schematic of Nafion® swelling under compressive stress. (a) Initial dry state, $\lambda = 0$. Lines represent collapsed hydrophilic pores. (b) Swelled state under no compressive stress. (c) Swelled state under high compressive stress.

This concept is illustrated in Figure 63. In (a), a Nafion® in dry state has collapsed hydrophilic pores. In (b), most of the surface area of hydrophilic pores can be associated with water molecules under no compressive stress, resulting in higher S. In (c), water molecules of the same amount as in (b) are concentrated in the middle of hydrophilic pores without being associated with some surface area which is not available under high compressive stress, resulting in smaller S.

In other words, not all the surface area of the collapsed hydrophilic pores is available for water uptake, but only a portion of it is effectively available depending on the compressive stress applied on Nafion®. If this hypothesis is true, the compressive stress will decrease the effective S and thus $\lambda_{i,m}$, which can nicely explain the experimental observations that the peak value of the chemical diffusion coefficients occurred at lower water content as the compressive stress increased. In fact, the peak position of the chemical diffusion coefficients corresponds to the peak position of the Darken factors, which occurs at the water content where the inflection of the sorption curve takes place. This inflection is related with the transition of the mechanism for water sorption. When a dry Nafion® membrane starts to take water, first a few water molecules are chemically bound to the sulfonic sites, which constitute the monolayer coverage. This

type of chemical sorption has a stronger driving force coming from the large enthalpy change of hydrating the sulfuric acid groups compared to physical sorption. Reucroft[114] measured the molar enthalpy of water sorption into Nafion® 117 membrane by microcalorimetry and found that 83 kJ per mole of Nafion® 117 was released for hydrating the membrane till $\lambda = 1$ and then decreased to ~50 kJ/mol for the case of $\lambda = 6$. This indicates that the enthalpic effect of hydrating Nafion® membranes vanishes as the sulfonic sites are associated with water molecules. When all the available sulfonic sites are occupied by the initial water molecules, the mechanism of physical sorption becomes dominant, which is obtained by the balance between the entropic effects of mixing Nafion®-water and the elastic deformation of the polymer matrix. The decrease of Gibbs free energy caused by mixing Nafion® with water molecules can be calculated by Eq. 53:

$$\Delta G_m = nRT(x_{nafion} \ln x_{nafion} + x_{water} \ln x_{water}), \qquad \text{Eq. 53}$$

where x's are mole fractions. Assuming $T = 300$ K, typical Gibbs free energy of mixing is less than 2 kJ per mole of Nafion®, which is much smaller than the contribution from the enthalpic effect. Correspondingly, the water uptake by physical sorption requires a greater increase of water activity within Nafion® membranes than that by chemical sorption. Because of the transition between the two different sorption mechanisms, the inflection in the sorption curve takes place when the water content reaches the monolayer coverage and makes the Darken factor maxed.

A direct verification of the hypothesis that the monolayer coverage decreases with increasing compressive stress would not be easy, which requires the measurements of the pore size distribution with a given water content under various compressive stresses. Although the measurement of the pore size distribution can be done by NMR cryoporometry,[115] the compression of a Nafion® sample with a given water content may squeeze out water molecules and the water content of the sample is no longer the same. However, the experimental observation of the decrease in the self-diffusion coefficients at a given water content with increasing pressure[76] may support the hypothesis because the schematic shown in Figure 63 (c) can exhibit smaller self-diffusion coefficients than (b) due to the less connectivity between the hydrophilic pores of (c), even though the average water contents of the two cases are the same. Therefore, the experimental observation of the effect of pressure on the self-diffusion is not adverse to the model. In addition, this

observation agrees with the view of Kreuer[116] on the conductivity activation volumes of Nafion®, who suggested that pressure could result in a more dendritic microstructure with narrower hydrophilic channels and a decreased conductivity.

Chapter 7. Experimental Determination of Electro-osmotic Drag Coefficients

There have been various studies to experimentally determine the coefficients of electro-osmotic drag.[18,77-82] The determination of electro-osmotic drag coefficients requires a careful measurement of water flux due to proton conduction and usually involves mathematical modeling to factor out the effects of diffusion, which is not trivial.[18,79] Fuller[78] and Zawodzinski[77] calculated the coefficients of electro-osmotic drag by a similar method using a concentration cell and electrochemical modeling. Unfortunately, there has not been a common agreement on the values of electro-osmotic drag coefficients. In addition, the fact that both the coefficients of diffusion and electro-osmotic drag may change as a function of the water content makes the required experiments or modeling more complicated.

As detailed in Chapter 6.3, the use of the data of water content distribution measure by the interferometry as a function of time and position enables the evaluation of the coefficients of electro-osmotic drag as a function of the water content. In this chapter, the mathematical concept is proved experimentally and the measured coefficients of electro-osmotic drag are presented.

7.1 Experimental

A dry Nafion® membrane was installed in the sample holder and left to absorb water by diffusion and electro-osmotic drag for 18 hours. In order to generate proton flux through a Nafion® membrane and induce electro-osmotic drag, the sample holder was slightly modified as shown in Figure 64. Two platinum wire electrodes were introduced at the both ends of a Nafion® sample. One electrode was inserted into the water chamber so that the bottom end of Nafion® could contact the electrode through liquid water. The other electrode was directly attached to the top end of the sample. When potential difference was applied between the two electrodes, the electrolysis of water occurred in the water chamber to generate protons, which were transferred through Nafion® and reduced at the other electrode to generate hydrogen gas. Proton current was controlled by a galvanostat (EG&G, model 263A). The reliability of the mathematical procedure for

extracting the electro-osmotic drag coefficients increases with greater proton current density. However, the large ohmic resistance of the sample limits the maximum current since the experiment began with a dry Nafion® membrane and the length of the sample was 8 cm. After a few trials, 0.1 mA through the cross section area of 0.0226 cm^2 corresponding to 4.43 mA/cm^2 was chosen in order not to make the galvanostat exceed its potential limit of 10 V. The spring force was adjusted so that the compressive stress applied to the sample was 50.4 kPa, which was the smallest one of the three conditions used for the diffusion experiments, to help the proton conductivity of the sample increase quickly. The variations in the water content during water uptake were monitored by the Mach-Zehnder interferometer shown in Figure 13.

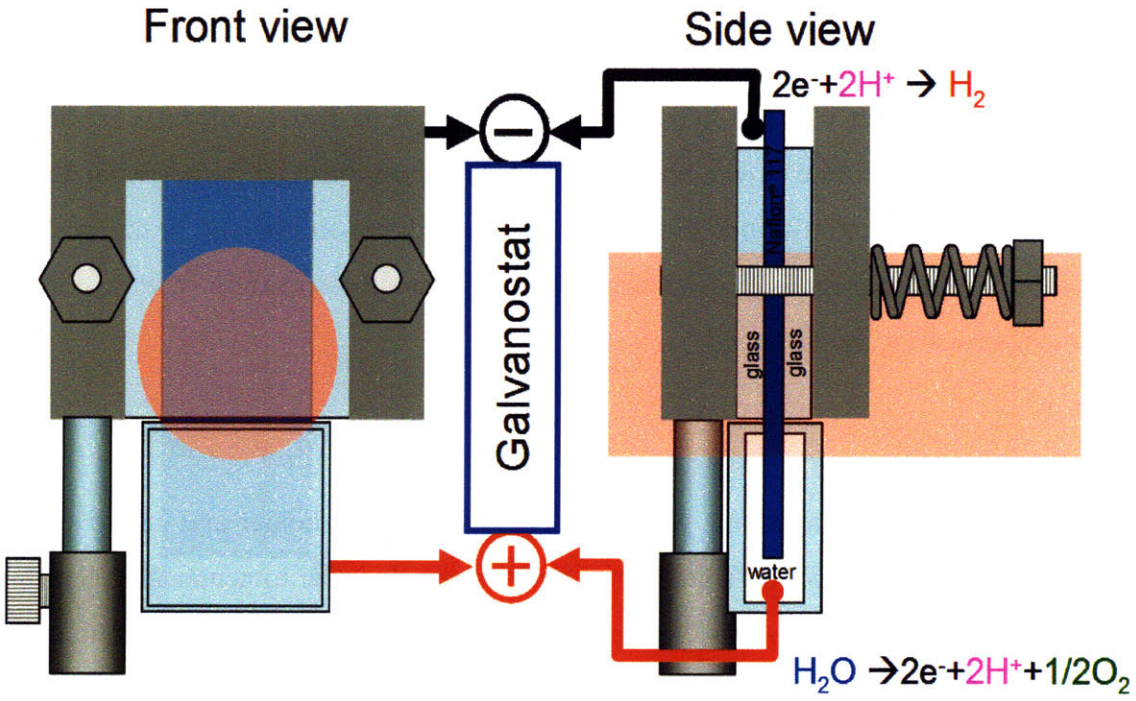

Figure 64. Nafion® sample holder for electro-osmosis of water. The membrane is connected to a galvanostat through platinum wire electrodes.

7.2 Results and Discussion

Figure 65 shows the variation in the interference intensity and the corresponding water content distribution during the diffusion and electro-osmosis process controlled by a step function in proton current with the interval of 2 hours or 7200 sec between steps.

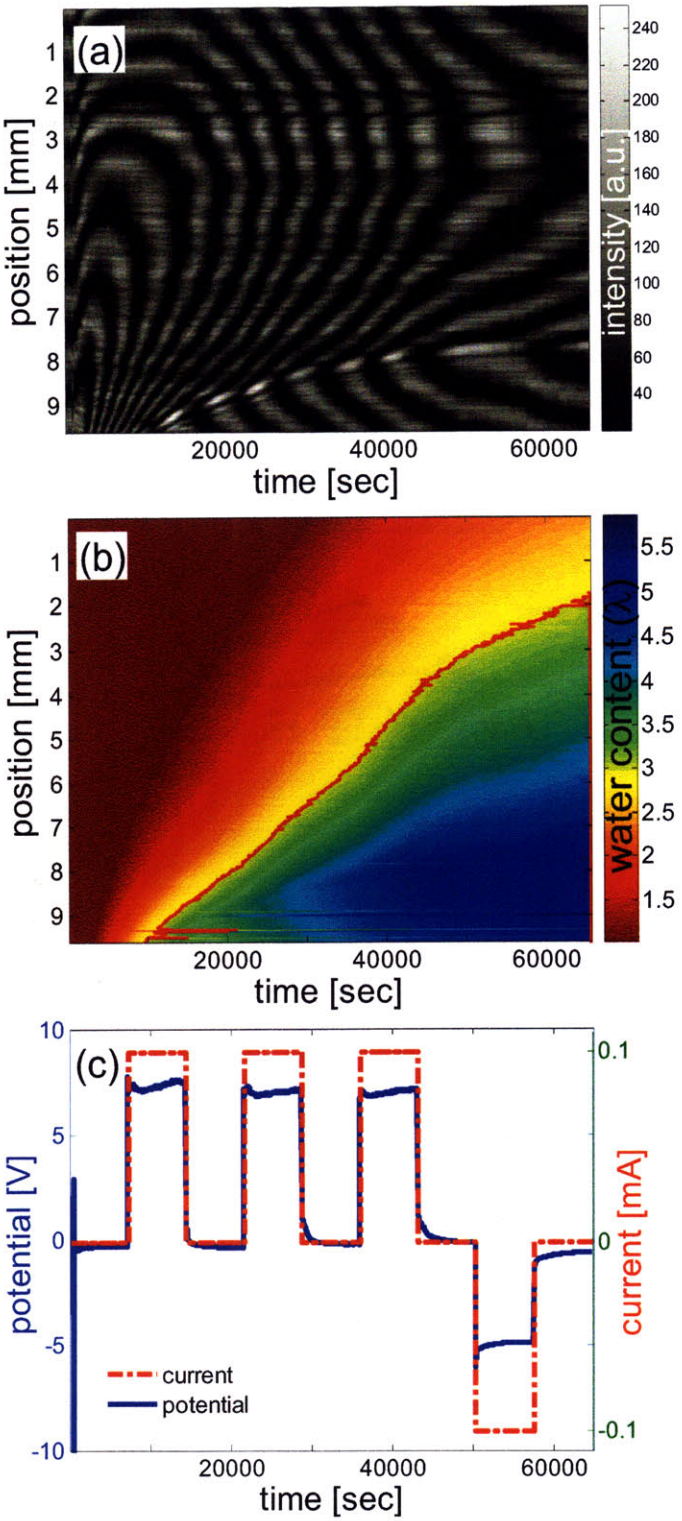

Figure 65. (a) Variations in interference intensity during diffusion and electro-osmotic drag. (b) Corresponding distribution of water content as a function of time and position, with the indication of a contour line of $\lambda = 3$ (solid red). (c) Step function for controlling the proton current.

Figure 65 (b) shows a similar wavy feature to the simulation result in Figure 43, as indicated by a contour line of $\lambda = 3$, due to the proton current controlling described by (c). The water uptake by diffusion was aided by electro-osmosis when a positive proton current was applied, while a negative proton current diminished the water uptake. In order to evaluate the coefficients of electro-osmotic drag, the partial derivatives of the water content were determined at a specific time when the step in proton current occurred, as shown in Figure 66.

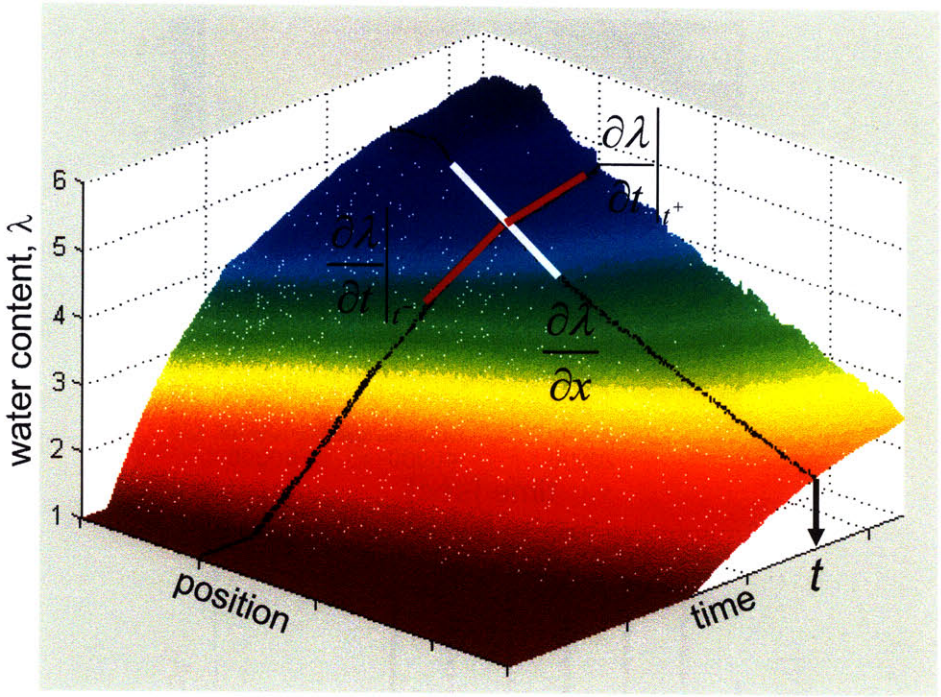

Figure 66. Evaluation of spatial and temporal derivatives of water content near current step at a time, t, when the current step occurred.

The procedure for calculating the coefficients of electro-osmotic drag was followed at every event of the current step with appropriate sign flips between rising and falling edges. The result is summarized in Figure 67. The coefficients of electro-osmotic drag at the first current step (*time* = 7200 sec) were not evaluated because the available range of water content was too narrow or $\lambda(time = 7200 \text{ sec}, x) < 3$. As pointed out in Chapter 6.3, the evaluation of electro-osmotic drag coefficients requires an integration constant of

$EOD(\lambda = 0) = 0$ because only $\partial EOD / \partial \lambda$ is calculated by the mathematical procedure. Therefore, the data from t = 14400 sec was aligned so that the linear fit of the data satisfied the condition of $EOD(\lambda = 0) = 0$. The other data sets were aligned so that the value of *EOD* at $\lambda = 3$, which was commonly available from all the data sets, had the same value under the assumption that *EOD* varied as a function of only λ.

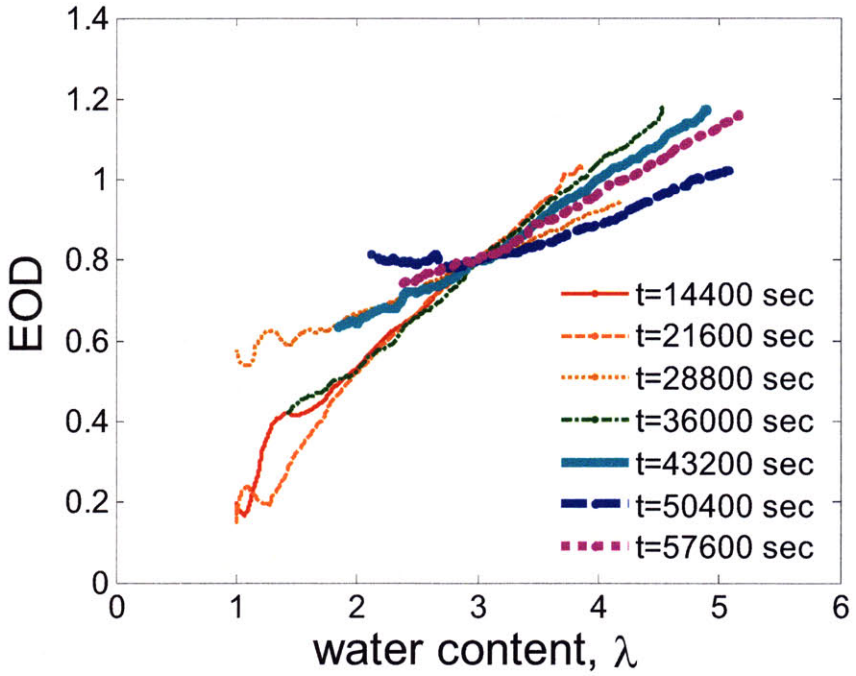

Figure 67. Electro-osmotic drag coefficients as a function of the water content evaluated at each current step.

It is clear that the coefficients of electro-osmotic drag increases from 0 to 1.2 with increasing water content, which agrees with the data obtained by Weng[79] and Fuller[78] as shown in Figure 68. It was pointed out by Choe[14] using molecular dynamics simulations that there are two competing mechanisms which determine the *EOD*. As the water content of Nafion® increases, the environment in Nafion® become more favorable for the Grotthuss mechanism of proton transport, which will result in the decrease in *EOD* because Grotthuss mechanism does not involve the transport of water molecules. At the same time, the environment of higher water content is also favorable for the diffusive motion of hydroniums (H_3O^+) which can more easily drag the water molecules

surrounding hydroniums. As a result, the simulational results by Choe[14] showed a slight increase of *EOD* from 0.92 to 1.23 as the water content increased from 4.1 to 12.7, which agreed with the data from Zawodzinski[77] and Fuller.[78] However, the rest of the *EOD* data shown in Figure 68 suggests that the *EOD* is strongly dependent on the water content. Unfortunately, the data obtained in this thesis can not provide the clear answer to the discrepancy because the available range of data was limited below $\lambda = 5$. Key factors required to fully understand the mechanism of the electro-osmotic drag will be the fraction of the contribution of the Grotthuss mechanism to the total proton conduction and the degree of proton hydration as a function of the full range of water content. None of these factors are easy to determine experimentally. However, the experimental data of *EOD* measured in this thesis may suggest that the Grotthuss mechanism does not yet actively contribute to the proton conduction and the physical dragging of water molecules by the diffusive motion of hydroniums is enhanced with the increasing water content at least in the range of $\lambda < 5$. In other words, the increase of β due to the increased water content exceeds the decrease in the second term of Eq. 14.

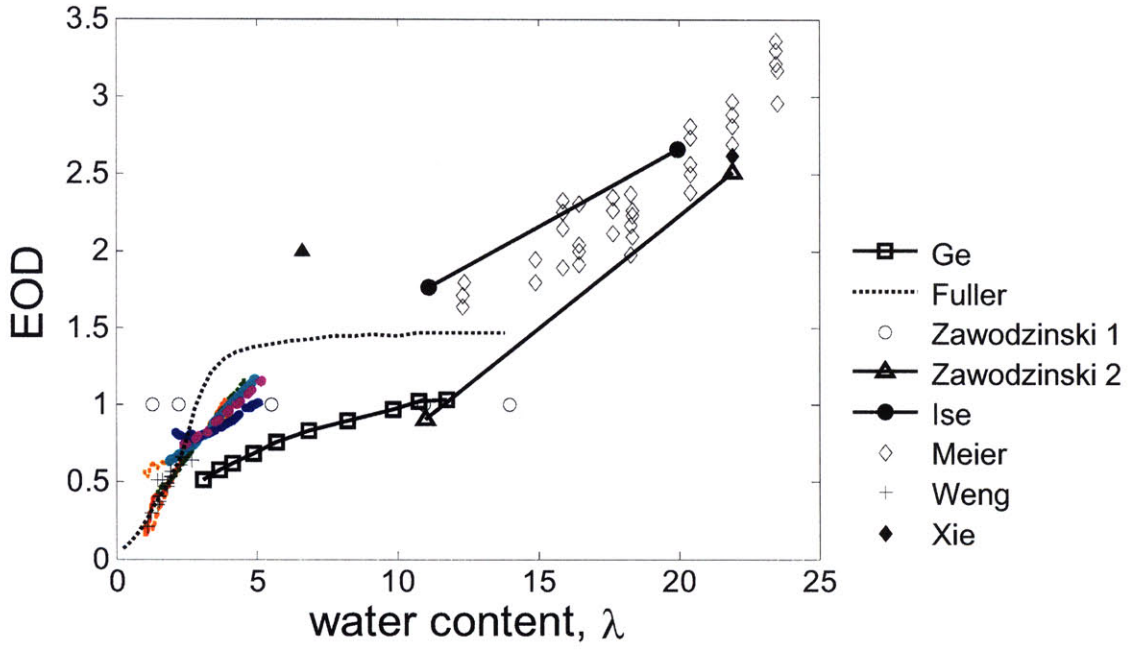

Figure 68. Comparison of the electro-osmotic drag coefficients obtained in this thesis (colored lines) with data from Ge,[18] Fuller,[78] Zawodzinski 1,[77] Zawodzinski 2,[67] Ise,[117] Meier,[118] Weng,[79] and Xie.[119]

As mentioned above, one of the limitations of this technique is that the measurable water content range is quite narrow, typically less than 6, which results from clamping Nafion® membranes between glass plates, indicating that constrained membranes can not reach the maximum water content of those in a free state. Another limitation is a very small proton current density applied through the membrane, typically less than 5 mA/cm^2, due to the enormous ohmic drop through a long Nafion® membrane (~8 cm). Even with this small current density, however, it was found that the coefficients of electro-osmotic drag increased with increasing water content, which demonstrated the sensitivity of the technique. A better sample holder design with a shorter length will allow more accurate measurements of electro-osmotic drag coefficients.

Chapter 8. Application of the Laser Interferometry for Monitoring a Nafion® Membrane in a Fuel Cell

The laser interferometry technique can also be utilized for in-situ monitoring Nafion® membranes installed in fuel cells because any changes of the membranes will be represented as the variations in the optical path length. Three main factors that change during the fuel cell operation are water content, stress, and temperature. All of these factors can vary spatially and temporally and the corresponding ΔOPL can be captured by an interferometer. Then, the measured ΔOPL can be converted to the factors of interest if the relationship among the factors and ΔOPL is established. Chapter 3 and Chapter 4 discussed the effects of water content and stress individually and it was found that the effect of stress is minimal compared to that of water content. Although it is out of the scope of this thesis to experimentally examine the effect of temperature, one can speculate that the refractive index or optical density of Nafion® will decrease as temperature increases because of the thermal expansion, while the thickness will increase. Consequently, the two effects cancel out each other and ΔOPL, which is the product of the two, will not vary significantly as a function of temperature. The Lorentz-Lorenz relation of Eq. 29 was used to verify this with the information on the thermal expansion coefficient, α, of Nafion® measured to be 1.47×10^{-4} by Takamatsu.[120] For the case of uni-directional expansion, the thickness and the density of a Nafion® membrane are written as:

$$\rho = \frac{\rho_0}{\left[\alpha(T-25^\circ C)+1\right]} \qquad \text{Eq. 54}$$

$$d = d_0\left[\alpha(T-25^\circ C)+1\right] \qquad \text{Eq. 55}$$

where ρ_0 and d_0 are the density and the thickness at 25°C, respectively. These two equations combined with Eq. 29 enable plotting ΔOPL as a function of temperature, as shown in Figure 69. The coefficient was found by a linear fitting:

$$\frac{1}{d_0}\frac{d\Delta OPL}{dT} = -5.97\times10^{-6}\ {}^\circ C^{-1} \qquad \text{Eq. 56}$$

When the typical variations in temperature and water content of 50 °C and 10 are assumed and $1/d_0(\partial\Delta OPL/\partial\lambda) = 0.01086$ found from Chapter 3 is used, ΔOPL due to

temperature change corresponds to ~0.3 % of ΔOPL due to water content change.

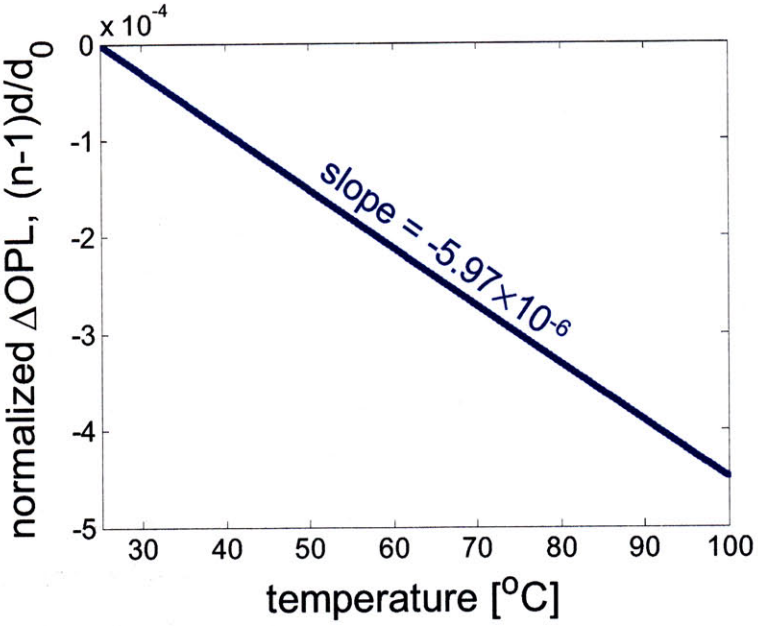

Figure 69. Relationship between temperature and the normalized ΔOPL of Nafion®.

Generally speaking, the ΔOPL of Nafion® is much more sensitive to material going in and out of it than other factors which are not accompanied by mass transport. Therefore, it is concluded that the variation of ΔOPL detected during the fuel cell operation can be mostly attributed to the changes in the water content.

A difficulty in applying the laser interferometry to a membrane assembled in a fuel cell comes from the fact that the components of a fuel cell except the membrane are not usually transparent, which block the optical access to the membrane. As a solution to overcome this, the rest of this chapter demonstrates the feasibility of detecting ΔOPL of a Nafion® membrane in an in-plane configuration. Although one can use a transparent fuel cell specially designed for the optical measurement, it would be more desirable if a commercially available fuel cell can be used.

8.1 Experimental

A dry Nafion® 117 membrane with the size of 25 mm × 70 mm was installed in a fuel cell (Electrochem, 5 cm^2 active area) as illustrated in Figure 70. The width of the

sample, 25 mm, was chosen as a minimum which can cover the whole area of the gas flow channels for the proper sealing, and also minimize the attenuation of the laser intensity and the effect of diffraction.

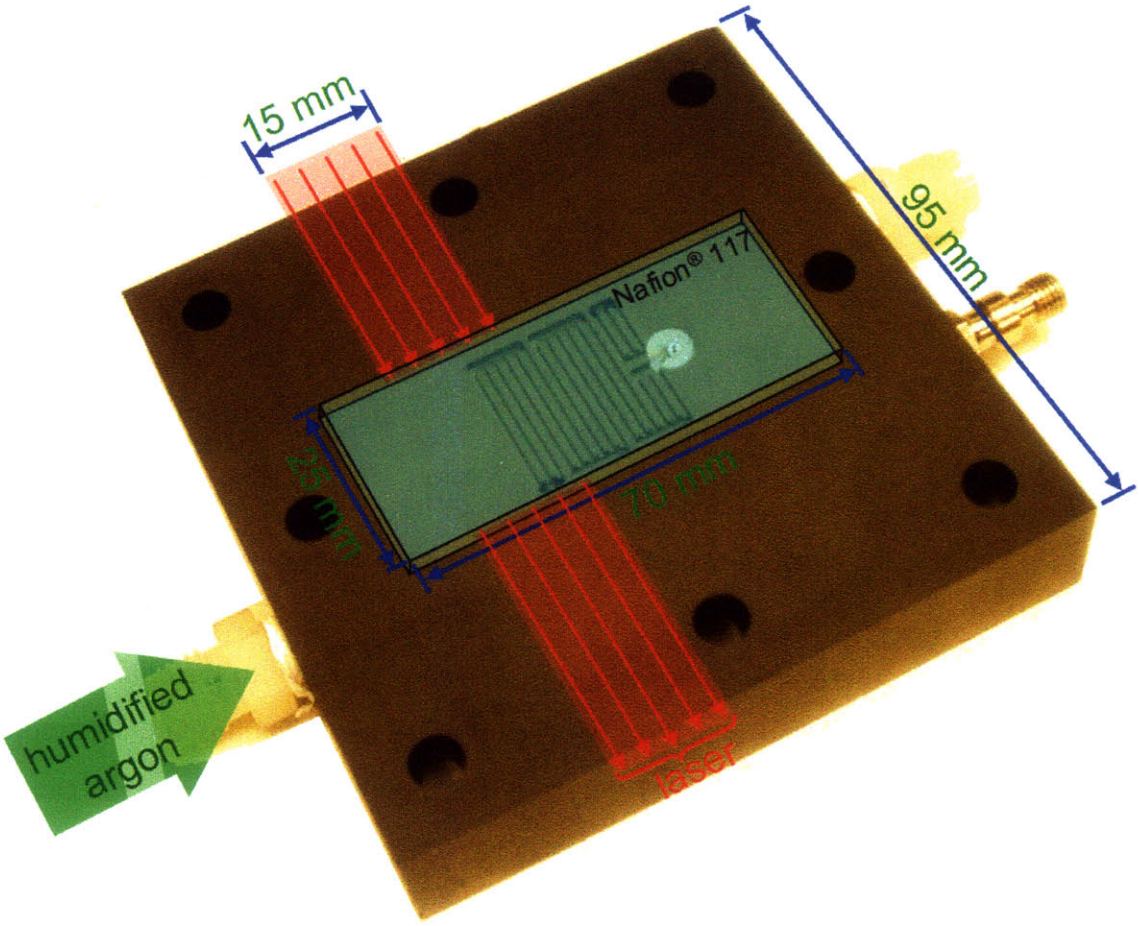

Figure 70. Nafion® 117 membrane installed in a fuel cell (Electrochem, 5 cm^2 active area) for the laser interferometry. The thickness of the membrane is not to scale. The other half of the fuel cell is omitted for illustration purpose, which was assembled to make the flow channels in both of the halves sealed during the actual experiment.

Argon gas saturated in a humidifying chamber at room temperature was provided through the flow channels of the fuel cell at ~20 cc/min to introduce changes in the water content of the membrane. 15 mm out of the total length of the membrane was observed by the interferometer and ~1/4 of the observed length was directly under the flow channel area. In order to see the effect of local humidification more clearly and more quickly, gas diffusion layers were not attached to the sample membrane, which would buffer and

smooth out the humidity from the flow channels. The variations in ΔOPL were measured by the same Mach-Zehnder interferometer shown in Figure 13.

8.2 Results and Discussion

Figure 71 shows a snap shot of the interference pattern obtained from the experimental setup of Figure 70 before the humidification started. In spite of the long distance of 25 mm, the laser beam penetrated the sample and interfered with the reference beam.

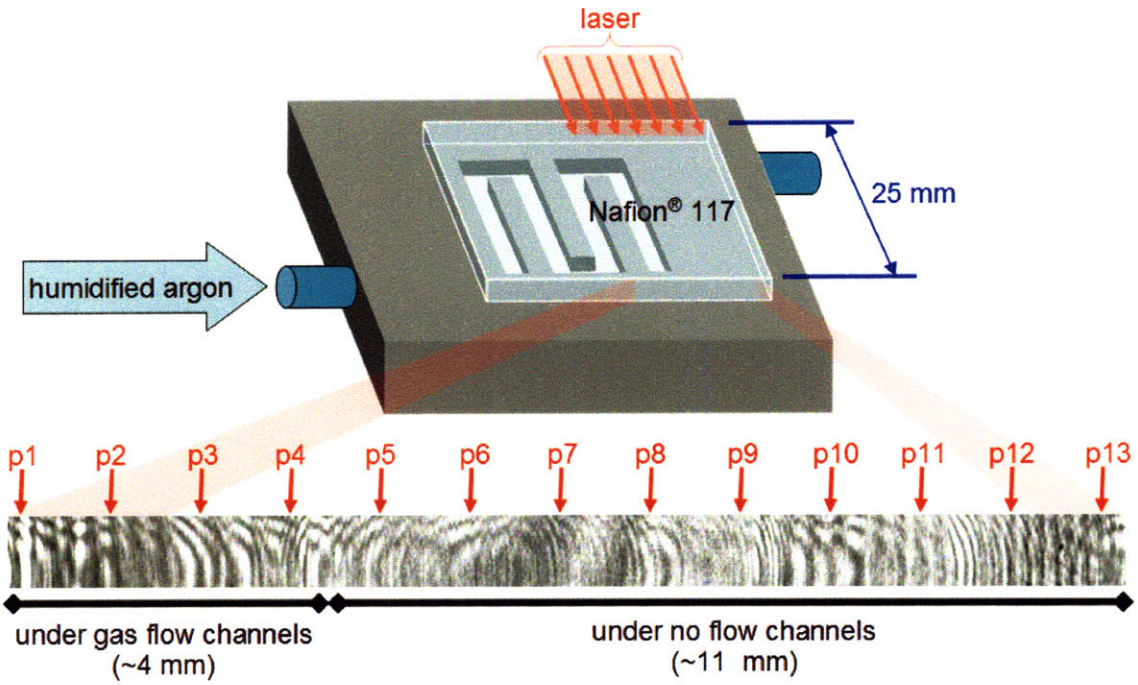

Figure 71. An image of interference pattern from the Nafion® 117 membrane assembled in a fuel cell with the indications for the position (p1~p13) where the temporal variations of intensity are analyzed. The illustration of the membrane and the fuel cell is not to scale.

However, the interference pattern shows a lot of ringing due to the effects of the diffraction through the membrane and the slit formed between the two current collectors of the fuel cell. When the humidified argon was provided to the flow channels, the intensity changed as a function of time. The variations in intensity along a horizontal line connecting the centers of the rings in Figure 71 are shown in Figure 72.

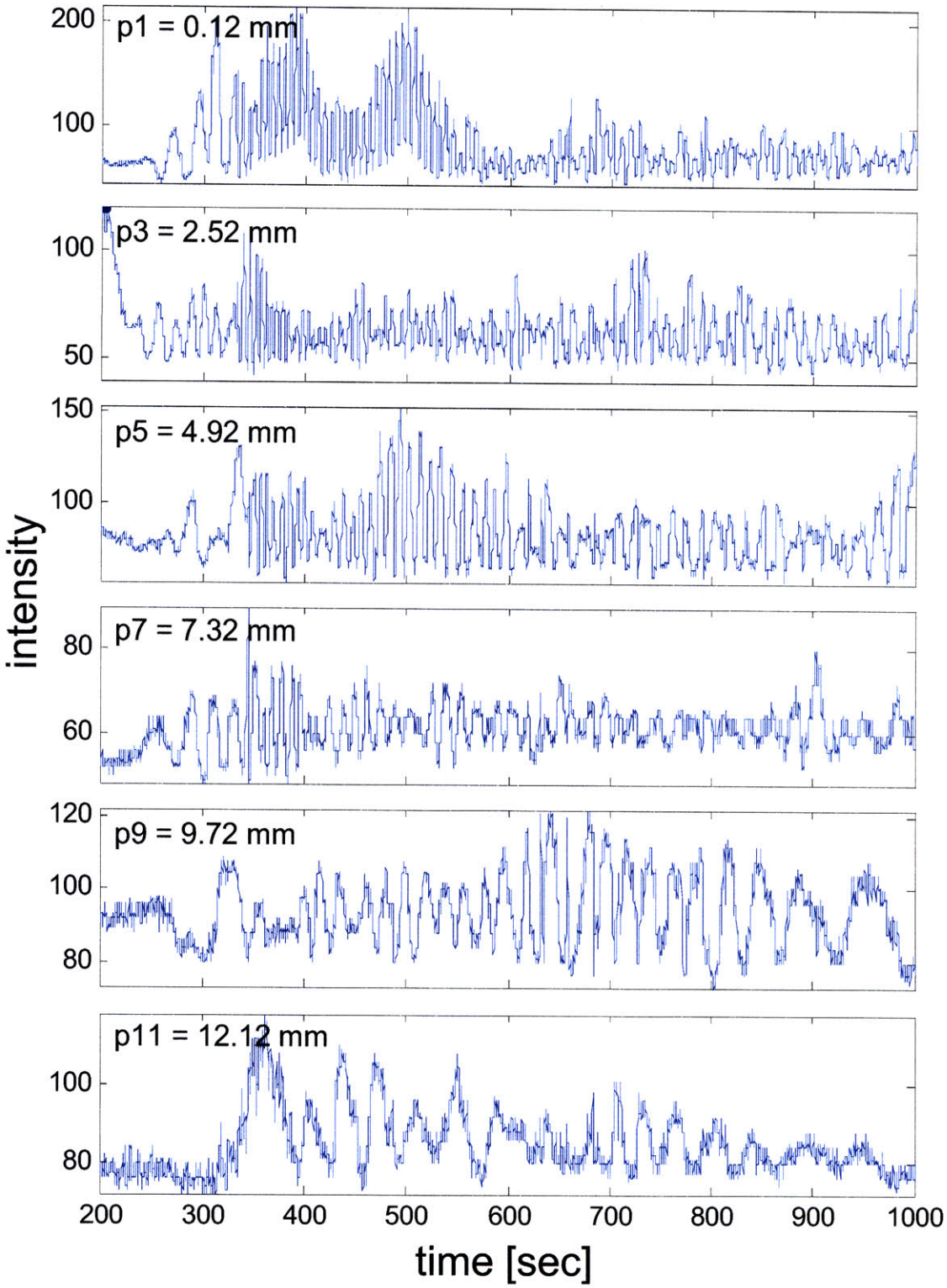

Figure 72. Variations in intensity at selected positions (p1, p3, p5, p7, p9, and p11) as a function of time during the humidification started at time = 100 sec.

It is clear that the frequency of intensity variation decreased as the distance from the flow channel area increased, which confirms that the interference intensity properly represented the changes in the water content of the sample membrane. Even though the conversion of the variations in interference intensity to the corresponding water content can be done by following the steps explained in Chapter 2, the large fluctuation in the amplitude of the intensity oscillation made it difficult to use an automated algorithm for the conversion. Instead, the peaks of each intensity oscillation at the selected positions were manually counted to generate a discrete set of the water content variation. Although the data set is discrete, the resulting temporal resolution is not bad because of relatively faster oscillation of the intensity from the in-plane configuration compared to that of cross-plane configuration, which is due to the huge difference in the optical path: 25 mm vs. 0.178 mm. The distributions of the water content at selected positions as a function of time are shown in Figure 73.

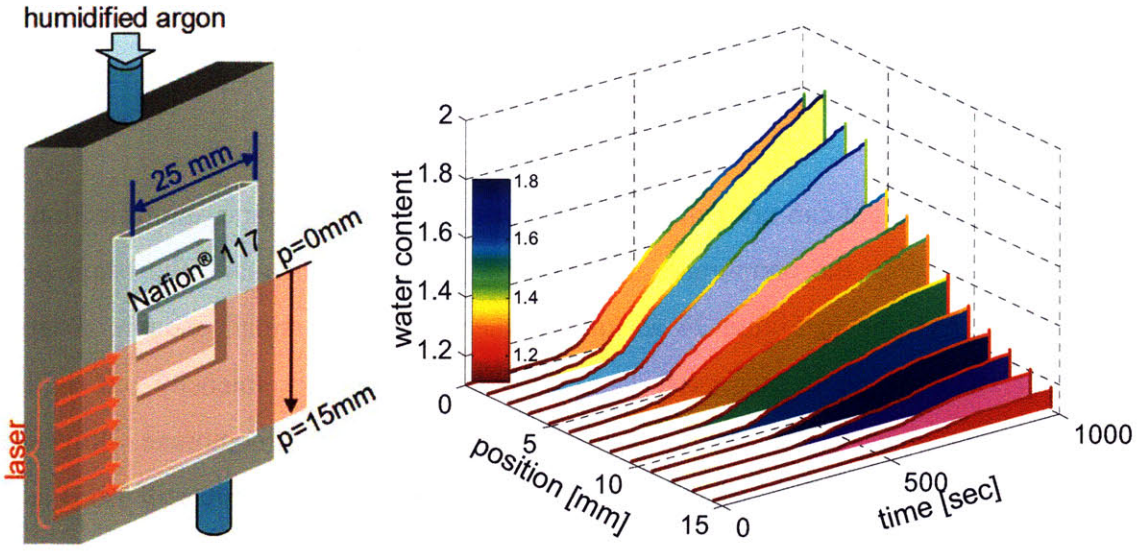

Figure 73. Water content change of Nafion® 117 membrane in a fuel cell at selected positions as a function of time, monitored by laser interferometry. Laser penetrated the width of 25mm. Only 1/4 (~4 mm) of observed length was under gas flow channels through which humidified argon passed.

It is clearly observed that that the area under flow channels (position = 0 ~ 4 mm) was

humidified more uniformly and rapidly compared to the rest which was not under flow channels and showed the characteristics of diffusion. The distribution of the water content was converted from ΔOPL using Eq. 28 which is for uni-directional swelling since the physical width of the sample, 25 mm, did not change during the humidifying process. It is noted that the water content at a given position is an averaged value due to the nature of the laser interferometry setup, which provides only one datum in space per entire penetration of the sample. This concept is illustrated in Figure 74.

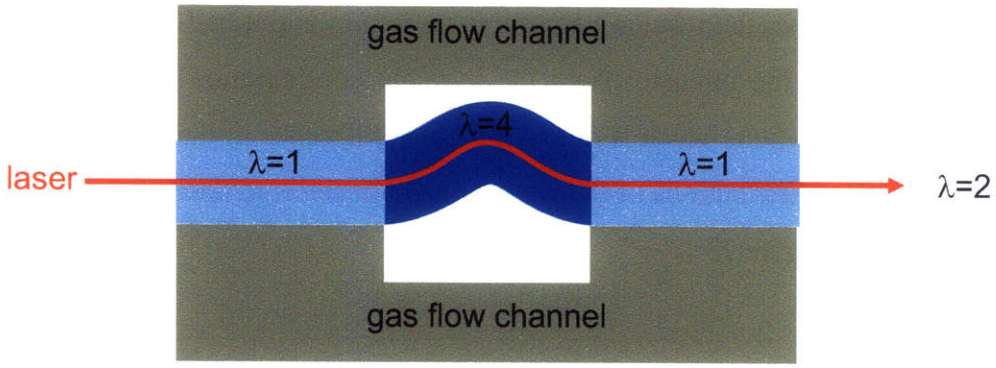

Figure 74. Averaging effect of the laser interferometry. Local swelling due to non-uniform humidification results in the average water content of 2.

Although the laser light can not bend along the shape of the membrane, the reflection at the interface between the membrane and gas flow channels will make the beam path similar to the red line in Figure 74 as long as the curvature is small enough. A large amount of study would be necessary to connect the interference intensity out of this complex optical object to the accurate water content of a Nafion® membrane. However, the data shown in Figure 73 obtained without the complex analysis are still valid as a rough but quick measure of the water content distribution as a function of time and position with enough resolutions for in-situ monitoring Nafion® membranes assembled in fuel cells.

Chapter 9. Concluding Remarks and Perspectives

A laser interferometry technique has been developed to measure the changes in the water content of Nafion® membranes with temporal and spatial resolutions. This technique allows not only in-situ monitoring of fuel cell membranes during the operation, but also the evaluation of the fundamental transport properties. The coefficients of diffusion and electro-osmotic drag were calculated by simply combining the measured data with the governing equation without many assumptions or constitutive equations. One unique feature of this procedure is that the dependency of these coefficients on the water content of the membrane can be obtained from a single set of experiment. This eliminates the tedious and time-consuming preparation of samples equilibrated at given activities of water vapor. In addition, this technique enables the evaluation of the chemical diffusion coefficients which is more appropriate to describe the net flux of water under the concentration gradient than the self-diffusion coefficients.

The chemical diffusion coefficients were found to decrease significantly with increasing compressive stress. Even though one can easily speculate the trend, this thesis has provided the first quantitative evidence of the effect of compressive stress on the chemical diffusion coefficients. In addition, it was found that the maximum water content of a constrained Nafion® membranes was limited compared to those in free state. In other words, water content of only 6~7 can be absorbed per each dimension in which Nafion® is allowed to swell. These observations suggest that a Nafion® membrane installed in a fuel cell undergoes spatially non-uniform compressive stress due to the corrugated design of the current collectors and consequently the diffusion speed or the amount of swell due to water uptake will differ from location to location. These non-uniform distributions of stress and swell may result in an early failure of the membrane when cycled between low and high relative humidity, although the effect can be alleviated by the presence of the gas diffusion layer.

The use of the laser interferometry for in-situ monitoring of fuel cells enables the direct measurements of the water content of Nafion® membranes because the optical path penetrates only the membranes which are transparent. Even though the experiments for demonstrating the feasibility of this gave only one dimensional distribution of the water content as a function of time, it is possible to reconstruct a two dimensional distribution if

multiple sets of one dimensional data are combined by tomographic method, as illustrated in Figure 75.

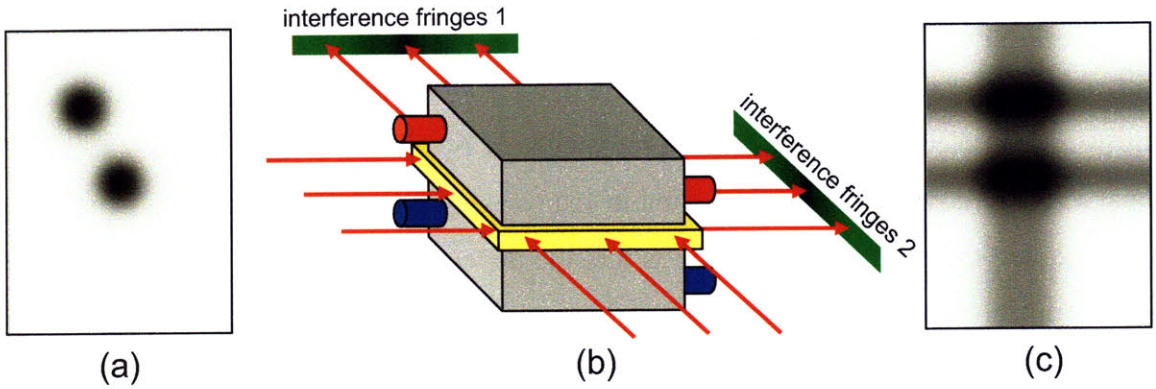

Figure 75. Concept of tomographic interferometry. (a) Distribution of the water content. (b) Experimental setup for two angle interferometry. (c) Reconstructed distribution of water content which shows streaking from the two separate spots in (a) due to the very limited number of scan angles. The spatial resolution of the tomographic reconstruction can be improved by increasing the number of scan angles.

As demonstrated by the experiments of methanol diffusion into Nafion® membranes, the application of the laser interferometry is not limited to the mixture of Nafion® and water. As long as a calibration is performed between the optical path lengths of the materials of interest and the desired properties, this technique can reveal many interesting phenomena such as the diffusion between two liquids or solid and liquid, which are invisible without the technique developed in this thesis.

Appendix A. Matlab® Code for Piecewise Noise Reduction

The following Matlab® m-files are used to reduce the noise in the data of interference intensities measured by the laser interferometry. The scheme of the algorithm was introduced in Chapter 2. The main function for noise reduction is 'denoise.m' which uses two sub-functions: 'lowpassfilter.m' for low-pass filtering and 'badpointindex.m' for determining whether local maxima and minima are noise or real variation of signal.

denoise.m

```
function smoothed_signal=denoise(raw_signal,sampling_rate,initial_cut_off_frequency)

%sampling_rate in [fps]
%initial_cut_off_frequency in [ratio to sampling_rate], max 0.5

cut_off_estimate(1)=sampling_rate*initial_cut_off_frequency;

smoothed_signal=lowpassfilter(raw_signal,cut_off_estimate(1),sampling_rate);
data_size=length(smoothed_signal);
time=(1:data_size)/sampling_rate;
time_raw=(1:length(raw_signal))/sampling_rate;
intensity_span=max(smoothed_signal)-min(smoothed_signal);

mm=2;

while length(badpointindex(smoothed_signal, intensity_span)) >= 1
    intensity_span=max(smoothed_signal)-min(smoothed_signal);
    bad_point_index=badpointindex(smoothed_signal,intensity_span);

    local_max_index=find(imregionalmax(smoothed_signal));
    local_min_index=find(imregionalmin(smoothed_signal));
    local_min_max_index=sort([local_max_index, local_min_index]);

    n=1;

    smoothed_signal_test=smoothed_signal;

    while length(badpointindex(smoothed_signal_test,intensity_span)) >=...
            length(bad_point_index)
        cut_off_estimate(mm)=cut_off_estimate(mm-1)-n*sampling_rate/data_size;
        n=n+1;

        smoothed_signal_new=lowpassfilter(raw_signal,cut_off_estimate(mm),sampling_rate);

        smoothed_signal_patch=smoothed_signal;
        for kk=1:length(bad_point_index)

            if local_min_max_index(bad_point_index(kk)-1)== 1

                for xx=local_min_max_index(bad_point_index(kk)-1):...
                        local_min_max_index(bad_point_index(kk))
```

```
                    smoothed_signal_patch(xx)= smoothed_signal_new(xx);
                end

            else
                for xx=local_min_max_index(bad_point_index(kk)-1):...
                        local_min_max_index(bad_point_index(kk))
                    weight= (xx-local_min_max_index(bad_point_index(kk)-1))/...
                        (local_min_max_index(bad_point_index(kk))-...
                        local_min_max_index(bad_point_index(kk)-1));
                    smoothed_signal_patch(xx)= weight*smoothed_signal_new(xx)+...
                        (1-weight)*smoothed_signal_patch(xx);
                end
            end

            smoothed_signal_patch(local_min_max_index(bad_point_index(kk)):...
                local_min_max_index(bad_point_index(kk)+1))=...
                smoothed_signal_new(local_min_max_index(bad_point_index(kk)):...
                local_min_max_index(bad_point_index(kk)+1));


            if local_min_max_index(bad_point_index(kk)+2)== data_size

                for xx=local_min_max_index(bad_point_index(kk)+1):...
                        local_min_max_index(bad_point_index(kk)+2)
                    smoothed_signal_patch(xx)= smoothed_signal_new(xx);
                end

            else
                for xx=local_min_max_index(bad_point_index(kk)+1):...
                        local_min_max_index(bad_point_index(kk)+2)
                    weight= (-xx+local_min_max_index(bad_point_index(kk)+2))/...
                        (local_min_max_index(bad_point_index(kk)+2)-...
                        local_min_max_index(bad_point_index(kk)+1));
                    smoothed_signal_patch(xx)= weight*smoothed_signal_new(xx)+...
                        (1-weight)*smoothed_signal_patch(xx);
                end
            end
        end

        smoothed_signal_test=smoothed_signal_patch;

    end
    smoothed_signal=smoothed_signal_test;
    mm=mm+1;

end
```

lowpassfilter.m

```
function low_pass_filtered=lowpassfilter(A,cut_off_frequency,sampling_rate)
data_size=length(A);
if mod(data_size,2)==1
    A(data_size)=[];
```

```
    data_size=data_size-1;
end

fourier_transformed=fft(A,data_size);
center_index=data_size/2+1;
cut_off_index=min(ceil(data_size*cut_off_frequency/sampling_rate),...
    data_size/2);

fourier_transformed(cut_off_index:min(data_size,2*center_index-cut_off_index))=0;

low_pass_filtered=ifft(fourier_transformed,data_size);
```

badpointindex.m

```
function bad_point_index=badpointindex(signal,intensity_span)

bad_point_index=[];
k=1;
local_max_index=find(imregionalmax(signal));
local_min_index=find(imregionalmin(signal));
local_min_max_index=sort([local_max_index, local_min_index]);
for n=2:length(local_min_max_index)-2
    if (abs(signal(local_min_max_index(n+1))-signal(local_min_max_index(n))) <...
        0.25*intensity_span)
            bad_point_index(k)=n;
            k=k+1;
    end
end
```

Appendix B. Derivation of Darken Equation (Eq. 43)

Relationship between the Chemical and the Intrinsic Diffusion Coefficient: D vs. D_i

The original Darken equation was derived from a binary alloy system.[121] The chemical diffusion coefficient, D, is defined by:

$$D = -J_{r,1}\left(\frac{\partial c_1}{\partial z}\right)^{-1}, \tag{B. 1}$$

where $J_{r,1}$ is the net flux of the component 1 observed from the outside of the mixture. c_1 and z are the concentration and the space coordinate, respectively. In order to relate the intrinsic and the chemical diffusion coefficient, a coordinate system fixed to the lattice of the binary alloy should be considered. Then, the intrinsic diffusion coefficient, D_i, can be related to the flux of each component relative to the lattice coordinate system.

$$J_1 = -\frac{D_{i,1}}{\Omega}\frac{\partial N_1}{\partial z} \quad \text{and} \quad J_2 = -\frac{D_{i,2}}{\Omega}\frac{\partial N_2}{\partial z}, \tag{B. 2}$$

where Ω is the atomic volume and N's are atom fractions. Therefore,

$$N_1 + N_2 = 1 \quad \text{and} \quad \frac{\partial N_1}{\partial z} = -\frac{\partial N_2}{\partial z} \tag{B. 3}$$

When there are no sources or sinks in the diffusion region, the number of lattice sites is fixed and the sum of the fluxes of atoms and vacancies is zero:

$$J_1 + J_2 + J_v = 0 \tag{B. 4}$$

The velocity, v, of a marker attached to the lattice plane is related to the vacancy flux by:

$$v = J_v\Omega = -(J_1 + J_2)\Omega = (D_{i,1} - D_{i,2})\frac{\partial N_1}{\partial z} \tag{B. 5}$$

If the fluxes are considered from another coordinate system attached to the outside of the diffusion zone, the following relation can be written:

$$J_{r,1} + J_{r,2} = 0 \tag{B. 6}$$

because the total number of atoms in the mixture will remain the same when observed from the outside. The net flux of the component 1, $J_{r,1}$, will be the same as the summation of J_1 and the flux due to the drift of the lattice plane, which is vN_1/Ω.

$$
\begin{aligned}
J_{r,1} &= J_1 + \frac{vN_1}{\Omega} = J_1 - (J_1 + J_2)N_1 = J_1(1 - N_1) - J_2 N_1 \\
&= J_1 N_2 - J_2 N_1 \\
&= -\frac{D_{i,1}}{\Omega}\frac{\partial N_1}{\partial z} N_2 - \frac{D_{i,2}}{\Omega}\frac{\partial N_1}{\partial z} N_1 \\
&= -(D_{i,1}N_2 + D_{i,2}N_1)\frac{1}{\Omega}\frac{\partial N_1}{\partial z} \\
&= -D\frac{\partial c_1}{\partial z}
\end{aligned}
\tag{B. 7}
$$

Since $c_1 = N_1 / \Omega$, finally the following equation is obtained:

$$
D = D_{i,1}N_2 + D_{i,2}N_1, \tag{B. 8}
$$

which relates the chemical diffusion coefficient to the intrinsic diffusion coefficient. When this equation is applied to a mixture of water and Nafion®, *N*'s are regarded as mole fractions, *x*, not atom fractions. Therefore,

$$
D = D_{i,1}x_2 + D_{i,2}x_1 \tag{B. 9}
$$

Relationship between the Intrinsic and the Self-diffusion Coefficient: D_i vs. D_{self}

In a binary mixture, the flux of the component 1 can be assumed to be proportional to the product of the concentration and the chemical potential gradient.

$$
J_1 = -Mc_1\frac{\partial \mu_1}{\partial z} = -D_{i,1}\frac{\partial c_1}{\partial z}, \tag{B. 10}
$$

where the second equality comes from the definition of the intrinsic diffusion coefficient. M is the mobility. The chemical potential is defined in terms of the activity coefficient, γ, and the mole fraction as follows:

$$
\mu_1 = \mu_1^0 + RT\ln(\gamma_1 x_1) \tag{B. 11}
$$

The spatial gradient of the chemical potential is:

$$
\frac{\partial \mu_1}{\partial z} = \frac{RT}{x_1}\frac{\partial x_1}{\partial z}\left(1 + \frac{\partial \ln \gamma_1}{\partial \ln x_1}\right) \tag{B. 12}
$$

Therefore, the intrinsic diffusion coefficient is:

$$D_{i,1} = Mc_1 \frac{\partial \mu_1}{\partial z}\frac{\partial z}{\partial c_1} = Mc_1 \frac{RT}{x_1}\frac{\partial x_1}{\partial z}\left(1+\frac{\partial \ln \gamma_1}{\partial \ln x_1}\right)\frac{\partial z}{\partial c_1}$$
$$= MRT\left(1+\frac{\partial \ln \gamma_1}{\partial \ln x_1}\right) \quad \text{(B. 13)}$$

For the case of the self-diffusion coefficient, the activity coefficient should depend on the overall value of $x_1 + x_2$, not the fraction of the tracers. Consequently, $\partial \ln \gamma_1 / \partial \ln x_1$ is zero.

$$D_{self,1} = MRT \quad \text{(B. 14)}$$

Therefore,

$$D_{i,1} = D_{self,1}\left(1+\frac{\partial \ln \gamma_1}{\partial \ln x_1}\right) \quad \text{(B. 15)}$$

Relationship between the Chemical and the Self-diffusion Coefficient: D vs. D_{self}

Plugging (B. 15) into (B. 9) results in:

$$D = D_{self,1}\left(1+\frac{\partial \ln \gamma_1}{\partial \ln x_1}\right)x_2 + D_{self,2}\left(1+\frac{\partial \ln \gamma_2}{\partial \ln x_2}\right)x_1 \quad \text{(B. 16)}$$

From the Gibbs-Duhem equation for a binary mixture at constant pressure and temperature:

$$x_1 \partial \mu_1 + x_2 \partial \mu_2 = 0 \quad \text{or} \quad \frac{\partial \ln \gamma_1}{\partial \ln x_1} = \frac{\partial \ln \gamma_2}{\partial \ln x_2}. \quad \text{(B. 17)}$$

(B. 16) can be simplified to:

$$D = \left(D_{self,1}x_2 + D_{self,2}x_1\right)\left(1+\frac{\partial \ln \gamma_1}{\partial \ln x_1}\right) \quad \text{(B. 18)}$$

Derivation of Darken Equation for a Nafion®-Water Mixture (Eq. 43)

For a Nafion®-water mixture, the mobility of Nafion® can be assumed to be much smaller than that of water or zero, and then the relationship between the chemical and self-diffusion can be written as:

$$D = \left(D_{self,water}x_{Nafion}\right)\left(1+\frac{\partial \ln \gamma_{water}}{\partial \ln x_{water}}\right) = \left(D_{self,water}x_{Nafion}\right)\left(\frac{\partial \ln a_{water}}{\partial \ln x_{water}}\right) \quad \text{(B. 19)}$$

The mole fractions of water and Nafion® can be expressed in terms of the water content,

λ:

$$x_{water} = \frac{\lambda}{\lambda + 1} \quad \text{and} \quad x_{Nafion} = \frac{1}{\lambda + 1} \tag{B. 20}$$

When these mole fractions are plugged into (B. 19),

$$D = D_{self,water} \frac{1}{\lambda + 1} \frac{\partial \ln a_{water}}{\partial \ln\left[\frac{\lambda}{\lambda + 1}\right]} \tag{B. 21}$$

The denominators can be rearranged as:

$$\begin{aligned} (\lambda + 1)\partial \ln\left[\frac{\lambda}{\lambda + 1}\right] &= (\lambda + 1)\left(\partial \ln \lambda - \partial \ln(\lambda + 1)\right) \\ &= \lambda \partial \ln \lambda + \partial \ln \lambda - (\lambda + 1)\partial \ln(\lambda + 1) \\ &= \partial \lambda + \partial \ln \lambda - \partial(\lambda + 1) \\ &= \partial \ln \lambda \end{aligned} \tag{B. 22}$$

Finally, the relationship between the chemical and the self-diffusion coefficient of water in Nafion® is:

$$D = D_{self,water} \frac{\partial \ln a_{water}}{\partial \ln \lambda}, \tag{B. 23}$$

which is the same result as Eq. 43.

References

1. Comparison of Fuel Cell Technologies, U.S. Department of Energy Hydrogen Program, http://www1.eere.energy.gov/hydrogenandfuelcells/fuelcells/pdfs/fc_comparison_chart.pdf (2008).
2. V. Mehta and J. S. Cooper, *J. Power Sources*, **114**, 32 (2003).
3. S. J. C. Cleghorn, X. Ren, T. E. Springer, M. S. Wilson, C. Zawodzinski, T. A. Zawodzinski and S. Gottesfeld, *Int. J. Hydrog. Energy*, **22**, 1137 (1997).
4. H. A. Gasteiger, S. S. Kocha, B. Sompalli and F. T. Wagner, *Appl. Catal. B-Environ.*, **56**, 9 (2005).
5. K. D. Kreuer, *J. Membr. Sci.*, **185**, 29 (2001).
6. Q. F. Li, R. H. He, J. O. Jensen and N. J. Bjerrum, *Chem. Mat.*, **15**, 4896 (2003).
7. J. L. Zhang, Z. Xie, J. J. Zhang, Y. H. Tanga, C. J. Song, T. Navessin, Z. Q. Shi, D. T. Song, H. J. Wang, D. P. Wilkinson, Z. S. Liu and S. Holdcroft, *J. Power Sources*, **160**, 872 (2006).
8. K. A. Mauritz and R. B. Moore, *Chem. Rev.*, **104**, 4535 (2004).
9. C. HeitnerWirguin, *J. Membr. Sci.*, **120**, 1 (1996).
10. Y. Sone, P. Ekdunge and D. Simonsson, *J. Electrochem. Soc.*, **143**, 1254 (1996).
11. B. Smitha, S. Sridhar and A. A. Khan, *J. Membr. Sci.*, **259**, 10 (2005).
12. S. Slade, S. A. Campbell, T. R. Ralph and F. C. Walsh, *J. Electrochem. Soc.*, **149**, A1556 (2002).
13. P. Choi, N. H. Jalani and R. Datta, *J. Electrochem. Soc.*, **152**, E123 (2005).
14. Y. K. Choe, E. Tsuchida, T. Ikeshoji, S. Yamakawa and S. Hyodo, *J. Phys. Chem. B*, **112**, 11586 (2008).
15. C. H. Lee, H. B. Park, Y. M. Lee and R. D. Lee, *Industrial & Engineering Chemistry Research*, **44**, 7617 (2005).
16. T. A. Zawodzinski, M. Neeman, L. O. Sillerud and S. Gottesfeld, *J. Phys. Chem.*, **95**, 6040 (1991).
17. T. A. Zawodzinski, C. Derouin, S. Radzinski, R. J. Sherman, V. T. Smith, T. E. Springer and S. Gottesfeld, *J. Electrochem. Soc.*, **140**, 1041 (1993).
18. S. H. Ge, B. L. Yi and P. W. Ming, *J. Electrochem. Soc.*, **153**, A1443 (2006).
19. D. R. Morris and X. D. Sun, *J. Appl. Polym. Sci.*, **50**, 1445 (1993).
20. X. Y. Huang, R. Solasi, Y. Zou, M. Feshler, K. Reifsnider, D. Condit, S. Burlatsky and T. Madden, *J. Polym. Sci. Pt. B-Polym. Phys.*, **44**, 2346 (2006).
21. D. Bograchev, M. Gueguen, J. C. Grandidier and S. Martemianov, *Int. J. Hydrog. Energy*, **33**, 5703 (2008).
22. A. Z. Weber and J. Newman, *Chem. Rev.*, **104**, 4679 (2004).
23. P. Costamagna, S. Grosso and R. Di Felice, in, p. 537 (2008).
24. P. H. Choi and R. Datta, *J. Electrochem. Soc.*, **150**, E601 (2003).
25. A. Z. Weber and J. Newman, *J. Electrochem. Soc.*, **150**, A1008 (2003).
26. P. J. James, J. A. Elliott, T. J. McMaster, J. M. Newton, A. M. S. Elliott, S. Hanna and M. J. Miles, *Journal of Materials Science*, **35**, 5111 (2000).
27. P. J. James, M. Antognozzi, J. Tamayo, T. J. McMaster, J. M. Newton and M. J. Miles, *Langmuir*, **17**, 349 (2001).
28. R. S. McLean, M. Doyle and B. B. Sauer, *Macromolecules*, **33**, 6541 (2000).

29. P. J. James, T. J. McMaster, J. M. Newton and M. J. Miles, *Polymer*, **41**, 4223 (2000).
30. L. Rubatat and O. Diat, *Macromolecules*, **40**, 9455 (2007).
31. G. Gebel and O. Diat, *Fuel Cells*, **5**, 261 (2005).
32. A. L. Rollet, O. Diat and G. Gebel, *J. Phys. Chem. B*, **106**, 3033 (2002).
33. L. Rubatat, A. L. Rollet, G. Gebel and O. Diat, *Macromolecules*, **35**, 4050 (2002).
34. L. Rubatat, G. Gebel and O. Diat, *Macromolecules*, **37**, 7772 (2004).
35. T. Thampan, S. Malhotra, H. Tang and R. Datta, *J. Electrochem. Soc.*, **147**, 3242 (2000).
36. S. J. Paddison and R. Paul, *Physical Chemistry Chemical Physics*, **4**, 1158 (2002).
37. K. D. Kreuer, *Chem. Mat.*, **8**, 610 (1996).
38. B. S. Pivovar, *Polymer*, **47**, 4194 (2006).
39. A. J. Easteal, A. V. J. Edge and L. A. Woolf, *J. Phys. Chem.*, **88**, 6060 (1984).
40. F. A. de Bruijn, V. A. T. Dam and G. J. M. Janssen, *Fuel Cells*, **8**, 3 (2008).
41. J. F. Wu, X. Z. Yuan, J. J. Martin, H. J. Wang, J. J. Zhang, J. Shen, S. H. Wu and W. Merida, *J. Power Sources*, **184**, 104 (2008).
42. A. Collier, H. J. Wang, X. Z. Yuan, J. J. Zhang and D. P. Wilkinson, *Int. J. Hydrog. Energy*, **31**, 1838 (2006).
43. S. D. Knights, K. M. Colbow, J. St-Pierre and D. P. Wilkinson, *J. Power Sources*, **127**, 127 (2004).
44. J. R. Yu, T. Matsuura, Y. Yoshikawa, M. N. Islam and M. Hori, *Electrochemical and Solid State Letters*, **8**, A156 (2005).
45. J. R. Yu, T. Matsuura, Y. Yoshikawa, M. N. Islam and M. Hori, *Physical Chemistry Chemical Physics*, **7**, 373 (2005).
46. E. Endoh, S. Terazono, H. Widjaja and Y. Takimoto, *Electrochemical and Solid State Letters*, **7**, A209 (2004).
47. H. L. Tang, P. K. Shen, S. P. Jiang, W. Fang and P. Mu, *J. Power Sources*, **170**, 85 (2007).
48. S. R. Samms, S. Wasmus and R. F. Savinell, *J. Electrochem. Soc.*, **143**, 1498 (1996).
49. Q. Deng, C. A. Wilkie, R. B. Moore and K. A. Mauritz, *Polymer*, **39**, 5961 (1998).
50. J. Surowiec and R. Bogoczek, *Journal of Thermal Analysis*, **33**, 1097 (1988).
51. C. A. Wilkie, J. R. Thomsen and M. L. Mittleman, *J. Appl. Polym. Sci.*, **42**, 901 (1991).
52. E. A. Cho, J. J. Ko, H. Y. Ha, S. A. Hong, K. Y. Lee, T. W. Lim and I. H. Oh, *J. Electrochem. Soc.*, **151**, A661 (2004).
53. Y. S. Kim, L. M. Dong, M. A. Hickner, T. E. Glass, V. Webb and J. E. McGrath, *Macromolecules*, **36**, 6281 (2003).
54. N. Sivashinsky and G. B. Tanny, *J. Appl. Polym. Sci.*, **26**, 2625 (1981).
55. M. Saito, K. Hayamizu and T. Okada, *J. Phys. Chem. B*, **109**, 3112 (2005).
56. F. N. Buchi, B. Gupta, O. Haas and G. G. Scherer, *Electrochim. Acta*, **40**, 345 (1995).
57. H. Wang and G. A. Capuano, *J. Electrochem. Soc.*, **145**, 780 (1998).
58. C. D. Huang, K. S. Tan, H. Y. Lin and K. L. Tan, *Chemical Physics Letters*, **371**, 80 (2003).
59. A. Pozio, R. F. Silva, M. De Francesco and L. Giorgi, *Electrochim. Acta*, **48**, 1543 (2003).
60. S. Stucki, G. G. Scherer, S. Schlagowski and E. Fischer, *J. Appl. Electrochem.*, **28**, 1041 (1998).

61. J. R. Yu, B. L. Yi, D. M. Xing, F. Q. Liu, Z. G. Shao and Y. Z. Fu, *Physical Chemistry Chemical Physics*, **5**, 611 (2003).
62. B. Mattsson, H. Ericson, L. M. Torell and F. Sundholm, *Electrochim. Acta*, **45**, 1405 (2000).
63. M. J. Kelly, G. Fafilek, J. O. Besenhard, H. Kronberger and G. E. Nauer, *J. Power Sources*, **145**, 249 (2005).
64. M. Inaba, T. Kinumoto, M. Kiriake, R. Umebayashi, A. Tasaka and Z. Ogumi, *Electrochim. Acta*, **51**, 5746 (2006).
65. V. O. Mittal, H. R. Kunz and J. M. Fenton, *J. Electrochem. Soc.*, **154**, B652 (2007).
66. G. Hubner and E. Roduner, *Journal of Materials Chemistry*, **9**, 409 (1999).
67. T. A. Zawodzinski, T. E. Springer, J. Davey, R. Jestel, C. Lopez, J. Valerio and S. Gottesfeld, *J. Electrochem. Soc.*, **140**, 1981 (1993).
68. T. A. Zawodzinski, T. E. Springer, F. Uribe and S. Gottesfeld, in, p. 199 (1993).
69. J. J. Sumner, S. E. Creager, J. J. Ma and D. D. DesMarteau, *J. Electrochem. Soc.*, **145**, 107 (1998).
70. C. A. Edmondson, P. E. Stallworth, M. C. Wintersgill, J. J. Fontanella, Y. Dai and S. G. Greenbaum, *Electrochim. Acta*, **43**, 1295 (1998).
71. H. L. Yeager and A. Steck, *J. Electrochem. Soc.*, **128**, 1880 (1981).
72. D. T. Hallinan and Y. A. Elabd, *J. Phys. Chem. B*, **111**, 13221 (2007).
73. G. Suresh, Y. M. Scindia, A. K. Pandey and A. Goswami, *J. Membr. Sci.*, **250**, 39 (2005).
74. S. Tsushima, K. Teranishi and S. Hirai, in, p. 235 (2005).
75. X. Gong, A. Bandis, A. Tao, G. Meresi, Y. Wang, P. T. Inglefield, A. A. Jones and W. Y. Wen, *Polymer*, **42**, 6485 (2001).
76. J. R. P. Jayakody, P. E. Stallworth, E. S. Mananga, J. Farrington-Zapata and S. G. Greenbaum, *J. Phys. Chem. B*, **108**, 4260 (2004).
77. T. A. Zawodzinski, J. Davey, J. Valerio and S. Gottesfeld, *Electrochim. Acta*, **40**, 297 (1995).
78. T. F. Fuller and J. Newman, *J. Electrochem. Soc.*, **139**, 1332 (1992).
79. D. Weng, J. S. Wainright, U. Landau and R. F. Savinell, *J. Electrochem. Soc.*, **143**, 1260 (1996).
80. X. M. Ren, T. E. Springer, T. A. Zawodzinski and S. Gottesfeld, *J. Electrochem. Soc.*, **147**, 466 (2000).
81. X. M. Ren, W. Henderson and S. Gottesfeld, *J. Electrochem. Soc.*, **144**, L267 (1997).
82. X. M. Ren and S. Gottesfeld, *J. Electrochem. Soc.*, **148**, A87 (2001).
83. S. S. Hsieh and Y. J. Huang, *J. Power Sources*, **183**, 193 (2008).
84. A. Hakenjos, H. Muenter, U. Wittstadt and C. Hebling, in, p. 213 (2004).
85. A. Hakenjos and C. Hebling, in, p. 307 (2005).
86. M. Noponen, J. Ihonen, A. Lundblad and G. Lindbergh, *J. Appl. Electrochem.*, **34**, 255 (2004).
87. F. B. Weng, A. Su, C. Y. Hsu and C. Y. Lee, in, p. 674 (2006).
88. K. Tuber, D. Pocza and C. Hebling, *J. Power Sources*, **124**, 403 (2003).
89. M. A. Hickner, N. P. Siegel, K. S. Chen, D. S. Hussey, D. L. Jacobson and M. Arif, *J. Electrochem. Soc.*, **155**, B427 (2008).
90. R. J. Bellows, M. Y. Lin, M. Arif, A. K. Thompson and D. Jacobson, *J. Electrochem. Soc.*, **146**, 1099 (1999).

91. R. Satija, D. L. Jacobson, M. Arif and S. A. Werner, *J. Power Sources*, **129**, 238 (2004).
92. Y. S. Chen, H. Peng, D. S. Hussey, D. L. Jacobson, D. T. Tran, T. Abdel-Baset and M. Biernacki, *J. Power Sources*, **170**, 376 (2007).
93. D. Kramer, J. B. Zhang, R. Shimoi, E. Lehmann, A. Wokaun, K. Shinohara and G. G. Scherer, *Electrochim. Acta*, **50**, 2603 (2005).
94. Z. Zhang, J. Martin, J. Wu, H. Wang, K. Promislow and B. J. Balcom, *J. Magn. Reson.*, **193**, 259 (2008).
95. Z. H. Zhang, A. E. Marble, B. MacMillan, K. Promislow, J. Martin, H. J. Wang and B. J. Balcom, *J. Magn. Reson.*, **194**, 245 (2008).
96. J. Bedet, G. Maranzana, S. Leclerc, O. Lottin, C. Moyne, D. Stemmelen, P. Mutzenhardt and D. Canet, *Int. J. Hydrog. Energy*, **33**, 3146 (2008).
97. G. Gebel, O. Diat, S. Escribano and R. Mosdale, *J. Power Sources*, **179**, 132 (2008).
98. Y. P. Patil, T. A. P. Seery, M. T. Shaw and R. S. Parnas, *Industrial & Engineering Chemistry Research*, **44**, 6141 (2005).
99. R. Mehra, *Proc. Indian Acad. Sci.-Chem. Sci.*, **115**, 147 (2003).
100. Y. Hida, K. Onose and S. Imamura, *Appl. Optics*, **36**, 6828 (1997).
101. R. Solasi, Y. Zou, X. Huang, K. Reifsnider and D. Condit, *J. Power Sources*, **167**, 366 (2007).
102. R. Solasi, Y. Zou, X. Y. Huang and K. Reifsnider, *Mechanics of Time-Dependent Materials*, **12**, 15 (2008).
103. J. V. Ford, B. G. Sumpter, D. W. Noid, M. D. Barnes and J. U. Otaigbe, *Appl. Phys. Lett.*, **77**, 2515 (2000).
104. B. Ovryn and J. H. Andrews, *Appl. Optics*, **38**, 1959 (1999).
105. T. E. Springer, T. A. Zawodzinski and S. Gottesfeld, *J. Electrochem. Soc.*, **138**, 2334 (1991).
106. S. Motupally, A. J. Becker and J. W. Weidner, *J. Electrochem. Soc.*, **147**, 3171 (2000).
107. J. Divisek, M. Eikerling, V. Mazin, H. Schmitz, U. Stimming and Y. M. Volfkovich, *J. Electrochem. Soc.*, **145**, 2677 (1998).
108. E. Skou, P. Kauranen and J. Hentschel, in, p. 333 (1997).
109. C. M. Gates and J. Newman, *Aiche J.*, **46**, 2076 (2000).
110. H. A. Every, M. A. Hickner, J. E. McGrath and T. A. Zawodzinski, *J. Membr. Sci.*, **250**, 183 (2005).
111. S. Hietala, S. L. Maunu and F. Sundholm, *J. Polym. Sci. Pt. B-Polym. Phys.*, **38**, 3277 (2000).
112. N. H. Jalani, P. Choi and R. Datta, *J. Membr. Sci.*, **254**, 31 (2005).
113. P. Y. Chen, C. P. Chiu and C. W. Hong, *J. Electrochem. Soc.*, **155**, B1255 (2008).
114. P. J. Reucroft, D. Rivin and N. S. Schneider, *Polymer*, **43**, PII S0032 (2002).
115. S. von Kraemer, A. I. Sagidullin, G. Lindbergh, I. Furo, E. Persson and P. Jannasch, *Fuel Cells*, **8**, 262 (2008).
116. K. D. Kreuer, S. J. Paddison, E. Spohr and M. Schuster, *Chem. Rev.*, **104**, 4637 (2004).
117. M. Ise, K. D. Kreuer and J. Maier, *Solid State Ionics*, **125**, 213 (1999).
118. F. Meier and G. Eigenberger, *Electrochim. Acta*, **49**, 1731 (2004).
119. G. Xie and T. Okada, *J. Electrochem. Soc.*, **142**, 3057 (1995).

120. T. Takamatsu and A. Eisenberg, *J. Appl. Polym. Sci.*, **24**, 2221 (1979).
121. P. G. Shewmon, *Diffusion in Solids*, Minerals, Metals & Materials Society, Warrendale, PA (1989).